Dissertation zur Erlangung des Doktorgrades
der Fakultät für Chemie und Pharmazie
der Ludwig-Maximilians-Universität München

Application of Molecular Dynamics Simulations for Deeper Understanding of siRNA–Nanoparticle Formulations and Their Interactions in Biological Environments

Katharina Maria Steinegger

aus

Ebersberg, Deutschland

2025

Erklärung

Diese Dissertation wurde im Sinne von § 7 der Promotionsordnung vom 28. November 2011 von Frau Prof. Dr. Olivia M. Merkel betreut.

Eidesstattliche Versicherung

Diese Dissertation wurde eigenständig und ohne unerlaubte Hilfe erarbeitet.

München, 06.10.2025

.....
Katharina Steinegger

Dissertation eingereicht am: 07.10.2025

1. Gutachterin: Prof. Dr. Olivia. M. Merkel

2. Gutachter: Prof. Dr. Wolfgang Frieß

Mündliche Prüfung am: 11.12.2025

“Love of learning is the most necessary passion…

in it lies our happiness.”

– Emilie du Châtelet

Table of Contents

Aim of the thesis

The aim of this work is the development of methods that utilize Molecular Dynamics (MD) simulations for molecular-level insights into siRNA-delivering nanoparticles. MD simulations have been proven valuable in other research areas, such as materials science or the design of small-molecule drugs. Hence, the application of MD in the research of complex nucleic acid delivery systems is a promising approach. As the validation of MD results by orthogonal methods is highly important to ensure the reliability of newly introduced simulation models, the presented work combines computational studies with complementary experiments.

A general introduction to the topic is provided in **Chapter I**, which first focuses on available siRNA delivery vehicles and general considerations for siRNA delivery. Then, the theory behind MD simulations is explained, and different MD techniques are highlighted.

In **Chapter II**, previously published approaches to the utilization of MD for understanding of nanoparticle-mediated siRNA delivery are summarized.

Chapter III focuses on the molecular organization of poly(beta-amino ester) (PBAE)-based polymeric nanoparticles (polyplexes). The investigated particles are based on an in-house-synthesized group of PBAEs comprising varying ratios of hydrophilic polycation side chains (spermine) to hydrophobic oleylamine side chains. Coarse Grained (CG) MD simulations showed the self-assembly of polyplexes on a molecular level, depending on polymer composition and N/P ratios. The presented MD results were validated by a variety of experimental methods, including Nuclear Magnetic Resonance (^{1}H NMR) and Transmission Electron Microscopy (TEM).

Chapter IV advances to the investigation of the interactions between nanoparticles and a biological environment. In this case, the interaction of four different polyplexes and one lipid nanoparticle (LNP) with endosome-mimicking membranes was simulated. Parameters such as particle hydrophobicity, environmental pH, and membrane composition were elucidated through large scale CG and complementary AA MD simulations. Subsequently, the computational results were correlated with performance differences observed between the particles *in vitro*.

Chapter I - General Introduction

1 Short interfering ribonucleic acid (siRNA) as therapeutic agent

1.1 RNA induced gene silencing

Through the process of ribonucleic acid interference (RNAi), messenger RNA (mRNA) is cleaved in a sequence specifically manner by the RNA-induced silencing complex (RISC), a cell endogenous nuclease[1]. RISC is activated by binding of the guide strand of a short interfering RNA (siRNA) to the Argonaute 2 (AGO2) subunit of RISC[2, 3]. As a result, the targeted mRNA, complementary to the bound siRNA strand, is degraded and no longer translated into a protein **(Figure I.1)**.

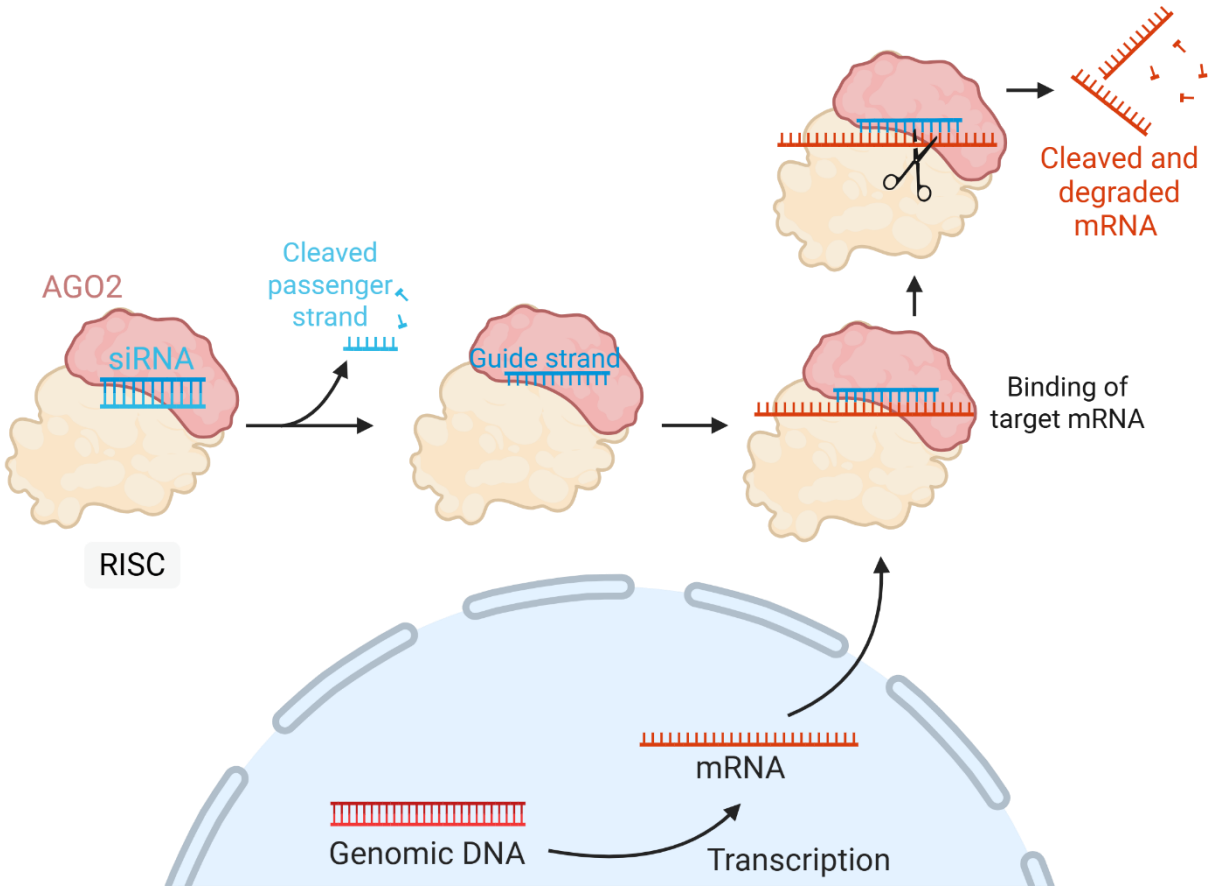

Figure I.1. Simplified schematic overview of the RNAi mechanism.

As an endogenous mechanism, cells utilize RNAi for post-transcriptional regulation of gene expression, protection from transposable elements, and antiviral defense[4, 5]. In this regard, cells cleave long double-stranded (ds) RNA to produce short sequences of approximately 20 – 25 base pairs[2], i.e., the siRNA.
However, through the introduction of synthetic siRNA[6], the mechanism of RNAi can be directed against any desired mRNA sequence, making it a promising tool for therapeutic applications.

To increase performance and stability, but also reduce immunogenicity, therapeutically applied siRNA is chemically modified[7]. Modifications can affect both strands and cover a broad range from the modification of the ribose (2′-OMe and 2′-F)[8] or the phosphate group[9], to base modifications and end-capping[10]. Nonetheless, only a few applications exist in which chemically modified siRNA, administered without a delivery vector (i.e., as “naked” siRNA), has demonstrated therapeutic efficacy in humans. These include direct targeting of the kidney and treatment of ocular diseases via intravitreal injection[10]. Systemically administered, naked siRNA shows poor cellular uptake and short circulation times due to rapid renal clearance, which can be improved by nanoparticle formulations[11]. With this approach, the first proof of successful siRNA delivery in humans *in vivo* was achieved in 2010[12]. Therefore, it is widely accepted that most therapeutic siRNA applications will depend on advanced nanotechnologies to achieve effective delivery.

As of 2025, several siRNA therapies are undergoing clinical trials, and seven FDA-approved siRNA therapies[13, 14] for humans are already on the market. Six of these are delivered as siRNA conjugated to trivalent N- acetylgalactosamine (GalNAc), which facilitates liver-targeted gene knockdown in humans[15]. Other conjugation approaches, for example to antibodies, are being studied to enable targeting to other tissues, such as tumors[16]. The range of non-viral delivery systems developed so far further includes inorganic and carbon-based materials, a broad variety of polymer-based nanoparticle systems, and lipid-based approaches **(Figure I.2)**[17].

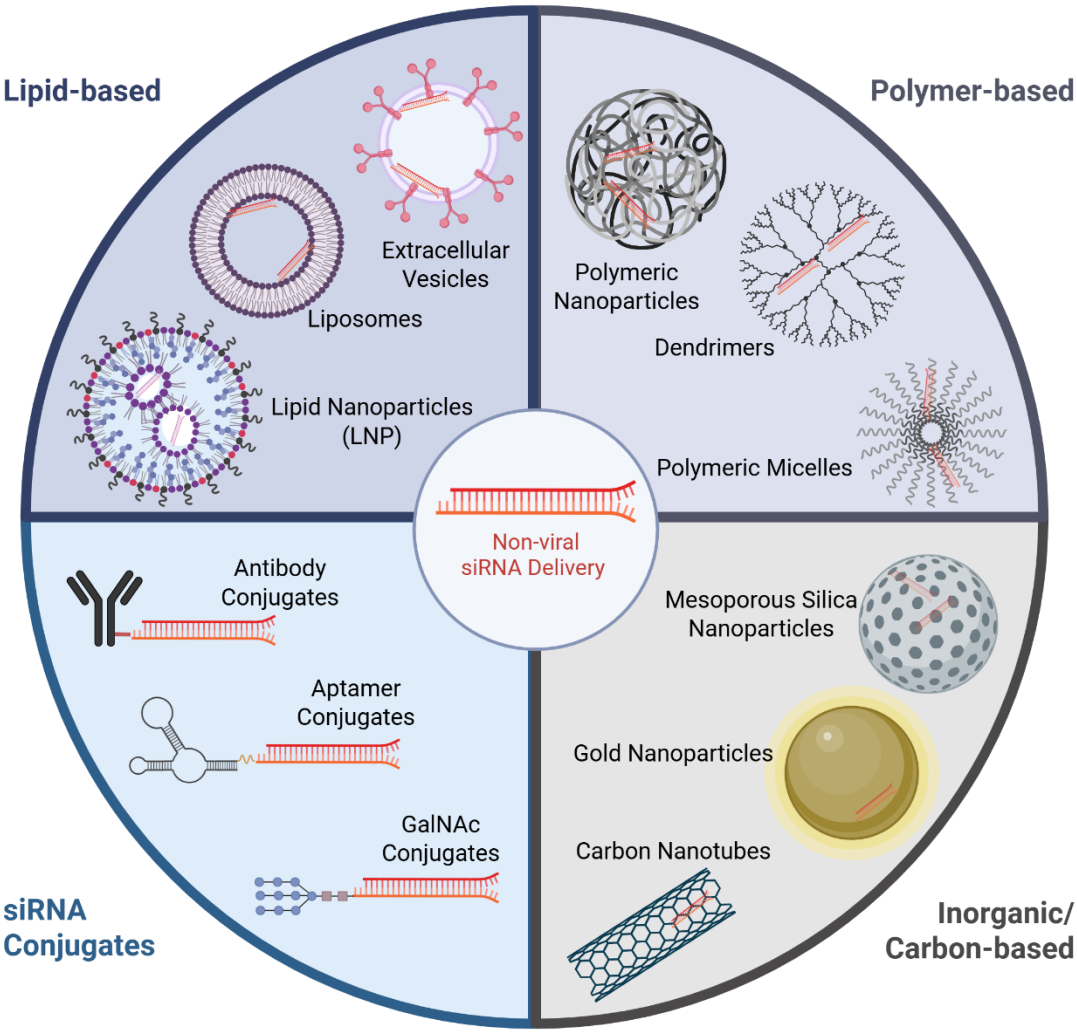

Figure I.2. Overview of some of the most studied non-viral siRNA delivery systems.

1.2 Lipid Nanoparticles

The use of lipids in the concept of liposomes as drug delivery vehicles was established as early as 1964[18]. Fifty-four years later, in 2018, the FDA approved the siRNA therapy patisiran[19], demonstrating that lipids are also capable of safely and efficiently delivering siRNA in the form of lipid nanoparticles (LNPs). Shortly thereafter, the mRNA COVID-19 vaccines developed by Moderna and BioNTech/Pfizer were approved[20]. Today, LNPs are the most extensively researched RNA delivery vehicles. They are commonly composed of four lipid types in varying ratios: A sterol (typically cholesterol), a helper lipid, a PEGylated lipid, and an ionizable lipid[21]. Like the GalNAc conjugates, the LNP formulation used in patisiran predominantly targets hepatocytes, which has been postulated to result from the abundance of apolipoprotein E (ApoE) in the protein corona that forms around the nanoparticle after injection[22]. To further advance LNP technology, selective targeting towards organs beyond the liver is highly desirable. For instance, the incorporation of a fifth lipid component enables the design of so-

called selective organ targeting (SORT) LNPs, which have been shown to direct siRNA delivery to the spleen, lungs, or kidneys[23]. Still, the search for novel lipids and optimized LNP formulations is ongoing, often aided by computational approaches such as the screening of large libraries by machine learning algorithms[24-26].

While the PEGylated lipid in LNP formulations is known to play a key role in controlling particle size and maintaining colloidal stability[21], fully delineating the individual contributions of each lipid component to RNA encapsulation or inner particle structure remains highly complex. For example, depending on the shape of the helper lipid[27], lipid to cargo ratios[28], and particle size[29], the inner structure of an oligonucleotide delivering LNP can range from multilamellar to inverse hexagonal structures and disordered phases. Consequently, lipid composition of an LNP largely determines its ability to fuse with biological membranes, which leads to large differences in downstream processes like the endosomal escape (EE) of LNPs[27, 30]. Sophisticated methods such as Small-Angle X-Ray Scattering (SAXS)[29, 31] help to unveil the inner organization of LNPs. Likewise, LNP structure is a research area in which computer-aided methods, like Molecular Dynamics (MD) simulations (see below) have proven to be highly insightful[32, 33].

1.3 Polymer based delivery systems

Due to the highly versatile nature of polymers, potential strategies to encapsulate siRNA into polymeric nanostructures are numerous. However, even though several applications have entered clinical trials[34], no polymer-based nanoparticle formulation for nucleic acids has been approved as a therapy to date (2025).

Polycationic structures efficiently interact with the polyanionic backbone of siRNA through electrostatic interactions. The most prominent polymer in this regard is polyethyleneimine (PEI) in its linear or branched forms with varying molecular weights[35, 36]. Alternatives include poly(2-(N,N-dimethylamino)ethyl methacrylate) (pDMAEMA), which shows similar encapsulation ability but lower transfection efficiency compared to PEI[37], or poly(L-lysine) (PLL), which comes with the advantage of being biodegradable[13]. Poly(amidoamine)s (PAMAM) on the other hand are well known in the design of dendrimers, which are highly branched, well defined three-dimensional polymeric structures[38]. However, the high cationic charge densities found in many polyplexes are often associated with cytotoxicity *in vitro* and *in vivo*[13, 37]. Advancements have been achieved by combining polymers with biocompatible materials such as poly(lactic acid-*co*-glycolic acid) (PLGA)[39], by increasing biodegradability[40] or by incorporating stealth moieties, such as poly(ethyleneglycol) (PEG) grafted variants. PEGylation of polymeric nanoparticles improves stability and circulation times, while simultaneously reducing the cytotoxicity of polycations by shielding the charge

dense region[41, 42]. On the other hand, a dense PEG layer on the nanoparticle surface can decrease transfection efficiency by hindering cellular uptake and EE[43].

As hydrophobic modifications of polymers exhibit great potential to enhance transfection efficiency[44-47], amphiphilic polymers received increasing attention[48]. In this regard, a block copolymeric structure facilitates the formation of polymeric micelles with a hydrophobic core[49]. Nucleic acids can be loaded into polymeric micelles through covalent conjugation or electrostatic interactions similar to conventional polyplexes, either in the core or the shell region of the micelle[50]. For polymeric micelles loaded with nucleic acids by electrostatic interaction, the term micelleplex has been established. Besides an often-increased EE performance, micelleplexes benefit from hydrophobic contributions to the self-assembly process, which results in increased colloidal stability[48, 51]. However, amphiphilic polymers do not always have a strictly block copolymeric structure, as showcased by poly(beta-amino ester)s (PBAE)s[52-54], which have attracted increasing interest due to their biodegradability and high versatility. PBAEs are synthesized by Michael addition of a diacrylate and primary amines, which enables the simultaneous introduction of hydrophilic and hydrophobic side chains[55].

1.4 Universal challenges of the siRNA delivery process

Although non-viral delivery vehicles vary widely in their chemical composition, several common challenges throughout the delivery process can be identified.

Before reaching the target tissue, the hurdles a formulation must overcome largely depend on the delivery route. Serum proteins adsorbing to the particle surface (the so-called protein corona) may render nanoparticles prone to immunological recognition[56]. In contrast, inhaled nanoparticles must additionally diffuse through mucus barriers before reaching epithelial lung cells[57].

The conjugation of targeting ligands to the surface of nanoparticles can direct them towards specific tissues or cell types[58], but the composition of the protein corona can likewise influence biodistribution[23].

Cellular uptake of nanomedicines is mostly mediated through a variety of endocytic mechanisms, which depend on both particle properties and cell type. While the process of phagocytosis is restricted to certain cell types such as macrophages, pinocytosis can be observed in most cells to varying degrees[59] **(Figure I.3A)**. Clathrin-mediated endocytosis (CME), a pathway exploited by many nanomedicines, is activated upon receptor-specific[60, 61] or receptor-independent[62] contact between particle and clathrin-coated pits on the plasma membrane. During CME, particles are internalized into clathrin-coated vesicles, which subsequently undergo intracellular trafficking along the endo-lysosomal pathway. In contrast,

caveolae-dependent endocytosis and clathrin/caveolin independent endocytosis circumvent the lysosomal compartment[63].
Which endocytic mechanism dominates for a given nanoparticle formulation depends on many factors such as particle size and shape[64]. For instance, caveolae-dependent endocytosis favors smaller particles than CME[65].

Finally, achieving high cellular uptake does not necessarily guarantee high transfection efficiency of a formulation[53]. Instead, siRNA must be released from the delivery vehicle and escape from endocytic vesicles, i.e., the endo-lysosomal compartment. EE is often referred to as the bottleneck of nucleic acid delivery, and underlying mechanisms are being widely discussed. EE of LNPs is believed to occur through direct interactions of particles and membrane[66], resulting in exchange of lipids and the formation of pores for the cargo to escape. For polycationic materials, rupture via the so-called proton sponge effect has long been proposed but is unlikely to represent the sole EE mechanism[36, 67] **(Figure I.3B)**. To date, EE remains a highly researched topic with many open questions[30, 48], as further discussed in Chapter IV.

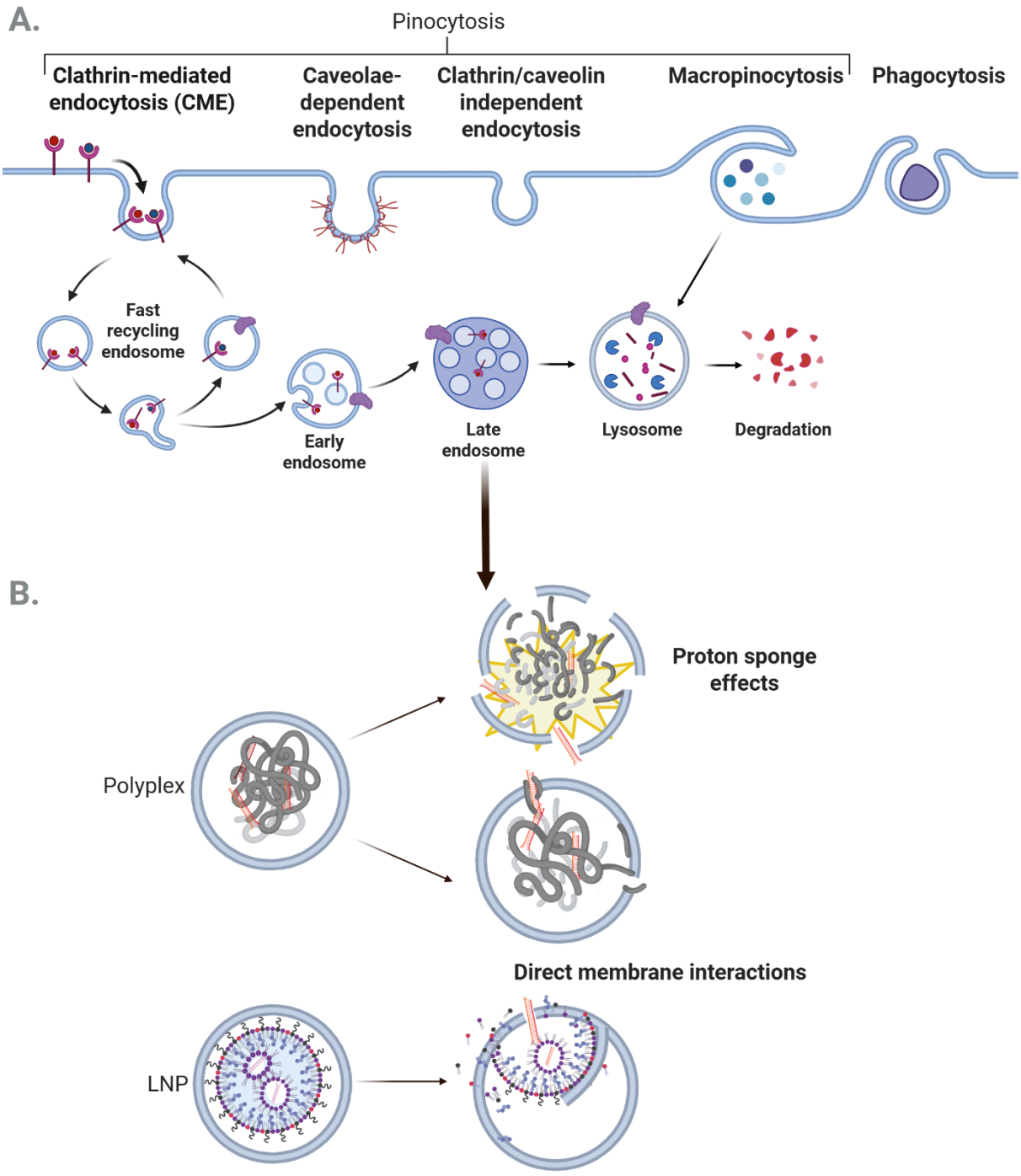

Figure I.3. Overview of proposed mechanisms for A. Cellular Uptake of nanoparticles and **B.** Endosomal escape mechanisms of polyplex- and LNP formulations.

2 Molecular dynamics (MD) simulations

2.1 MD simulations for pharmaceutical applications

Molecular Dynamics (MD) simulations are a broadly applied tool in both materials and life sciences. Especially in the context of small-molecule drug discovery, MD is widely established, as it aids in target modelling, binding pose prediction, lead optimization and serves as a valuable tool in virtual screening processes[68]. Likewise, advancements have been made to apply MD in drug development: valuable contributions include studies on drug solubility[69], protein formulation[70], and nanotechnologies[71, 72].

2.2 The physical background of MD simulations

MD simulations visualize the motion of particles, such as single atoms, based on Newton's equations of motion. The potential energy of such a simulated system is composed of two main components, i.e., bonded and non-bonded interactions. Bonded interactions involve forces between covalently bound atoms of a molecule, namely bond potentials, angle potentials, and both proper and improper dihedrals, whereas non-bonded interactions include contributions from the Lennard-Jones potential and electrostatic forces **(Figure I.4)**[73].
These interactions are defined within a force field, which serves as the mathematical framework of an MD simulation. However, accurately capturing all relevant interactions for a specific system remains a non-trivial task. As such, the refinement and development of MD force fields continues to be an active area of research.

Force fields can be developed based on experimental data, such as X-ray diffraction or nuclear magnetic resonance (NMR) data. Alternatively, they can be derived from quantum mechanical (QM) calculations, such as *ab initio* calculations or density functional theory (DFT), or from a combination of both QM and experimental data[74, 75]. Force fields can be differentiated according to their application (i.e., force fields that are optimized for the simulation of a certain type of biomacromolecules[76]) or their resolution (see below). Additionally, a distinction between additive and polarizable force fields can be made[77]. In addition to bonded and non-bonded interactions, polarizable force fields account for the response of electron clouds to changing electrostatic environments, which increases simulation accuracy[78]. However, this inclusion of additional mathematical terms comes at a significant computational cost[79].

In summary, all force fields are based on the common ground of classical mechanics. Yet, due to the incorporation of different data sources in their refinement, some force fields are more suitable for specific setups than others. The choice of the force field for an MD study can therefore strongly influence its outcome[80-83].

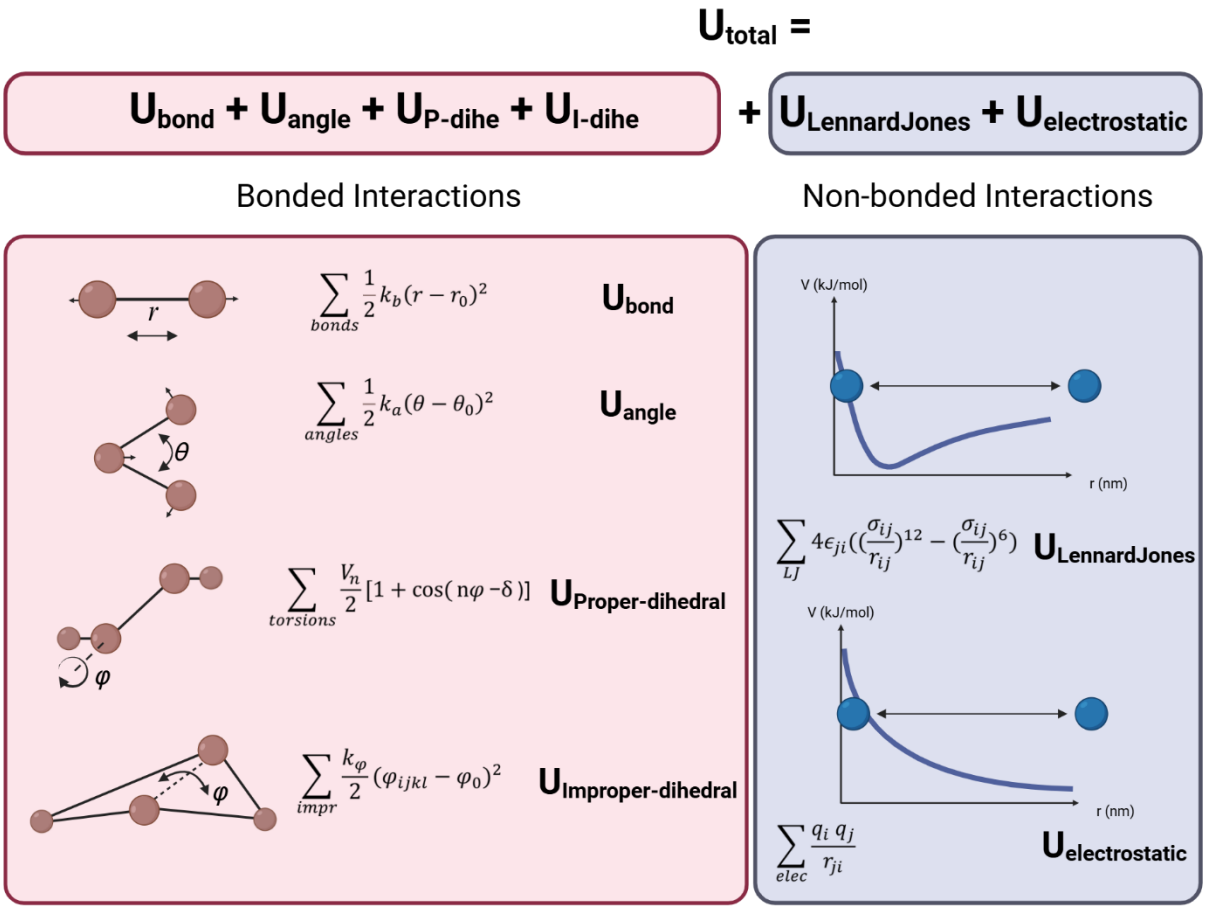

Figure I.4. Basic representation of the interactions contributing to the force field within an MD simulation.

2.3 All Atom Simulations

MD simulations can be designed at different levels of resolution. Intuitively, All Atom (AA) MD simulations treat each atom as a particle with individual interactions and properties. The increasing availability and capability of computational resources over the last decades, for example acceleration through graphics processing units (GPUs)[84] and the incorporation of artificial intelligence, has enabled AA MD simulations of increasingly large systems, such as a complete model of the SARS-CoV-2 viral envelope[85]. However, more commonly, AA simulations are applied to system sizes below 50 nm and simulation times below 10 µs[86-88]. Several additive AA force fields with distinct strengths and limitations are widely used. The AMBER family encompasses a variety of force fields, primarily optimized for biomolecules such as proteins, nucleic acids, and lipids[89-91]. The most recent CHARMM force fields include CHARMM36[92] for biomolecules and the CHARMM General Force Field (CGenFF) for small organic molecules and non-standard compounds. Parameter extensions have been published for specific molecules[93, 94] as well as extensive, more general improvements[95]. In

contrast, the OPLS-AA force field is particularly well suited for small molecules but remains less advanced for biomacromolecules[96].

2.4 Coarse Grained Simulations

Coarse Grained (CG) MD simulations make use of a simplified resolution of molecules, most commonly representing 3–4 heavy atoms as one bead[97] **(Figure I.5)**. This reduction of particles in the system substantially decreases the degrees of freedom in a simulation setup. Additionally, coarse-graining enables larger integration time steps, as fast vibrating bonds (e.g., hydrogen bonds) are no longer represented and hence energy surfaces are smoother[98]. Overall, this leads to an increase in simulation time by 1–2 orders of magnitude in comparison to an equally sized AA simulation box with the same computational resource consumption[99]. With CG simulations, boxes well above 100 nm side length are accessible[100], as well as timescales of several tens of microseconds[101].

The most popular CG force field is the Martini force field, which was first introduced in 2007 as a general model for biomolecular simulations[102]. Since 2021, Martini has been available in its third, refined version, Martini 3[97]. The aim of Martini 3 was to reduce shortcomings of previous versions, such as overstabilization of biomolecular assemblies[103], and to expand the variety of bead types, thereby increasing the chemical space Martini 3 can be applied to[104]. As described above, force fields, especially AA force fields, are parametrized based on experimental data and quantum mechanical data. In the case of Martini 3, the bead types were validated by reproducing experimental water-oil transfer free energies and solvent miscibility data. Consequently, a variety of simulation setups were tested and compared to other experimental or AA simulation results, demonstrating strongly improved performance of the force field[97]. In general, CG results are often refined to match AA simulations to ensure the quality of a newly parametrized molecule model, before upscaling to larger simulation setups[101, 105]. Since the publication of Martini 3, parametrizations of complex molecules, such as carbohydrates[106] and cholesterol[107] have become publicly available. Additionally, automated tools to generate CG input have been developed: This allows for automated generation of protein models, membranes, and preassembly of whole LNPs in CG resolution[108, 109]. Furthermore, the titratable Martini 3 version allows to simulate changes of protonation depending on the pH environment of a molecule[110], whereas backmapping approaches — i.e., restoring AA resolution to a simulated system that has reached equilibrium in a CG setup — help to combine simulations of large systems with AA accuracy[111].

Nevertheless, even with Martini 3, room for improvement remains[112]. For instance, Martini 3 failed to reproduce experimental data concerning protein-protein interactions, making further

optimization of the force field necessary[113]. Similarly, in the case of intrinsically disordered proteins, Martini 3 needed modifications to better keep up with state-of-the-art AA force fields[114]. Hence, AA and CG simulations coexist synergistically.

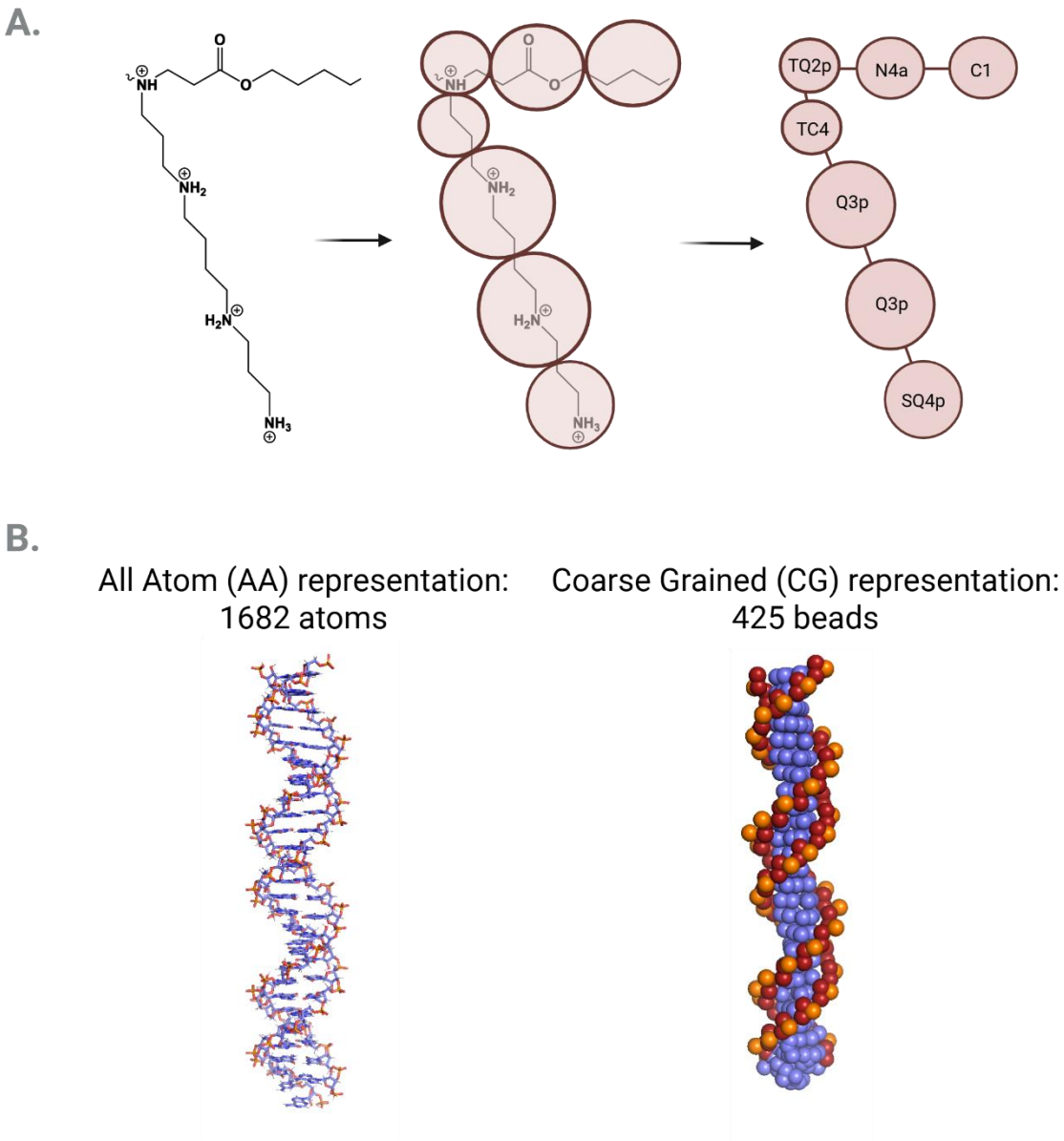

Figure I.5. All Atom versus Coarse Grained MD simulation. A. Visualization of the coarse-graining process of a molecule fragment. **B.** Comparison of a siRNA molecule in AA and CG resolution.

2.5 Advanced sampling techniques

A variety of techniques enable MD simulations of rare events that are not accessible within the timescales of classical equilibrium MD.

The umbrella sampling method[115] applies harmonic biasing potentials to the system of interest, restraining it to overlapping windows along a predefined collective variable (CV). The biased distributions obtained from these windows are subsequently reweighted, for example using the Weighted Histogram Analysis Method (WHAM)[116], to reconstruct the unbiased probability distribution. From this, the potential of mean force (PMF) can be derived, representing the free-energy profile along the reaction coordinate.

Similarly, metadynamics simulations derive free-energy surfaces (FES) of a system along predefined CVs. During the simulation, Gaussian hill potentials are added in a history-dependent manner. This enables the system to overcome energy barriers, while at the same time discouraging the system to revisit previously explored states[117].

In accelerated MD (aMD), no prior knowledge of the potential energy landscape of a system and no definition of CVs are required. The method raises energy minima, thus reducing the barriers the system must overcome to transfer from one metastable state to another[118].

In contrast to these methods, Replica Exchange MD (REMD) samples multiple replicas of the system at different temperatures or with independent Hamiltonians. Exchanges of replica configurations allow the system to cross energetic barriers more efficiently, thereby enhancing sampling even at lower temperatures[119].

2.6 Limitations of Classical MD simulation

While being extremely powerful in providing mechanistic insights into biomolecular processes and molecular interactions, MD simulations do not allow the formation or breakage of covalent bonds[84]. The simulation of chemical reactions therefore lies beyond the scope of classic MD. For this type of insight, *ab initio* molecular dynamics (AIMD), which incorporates electronic properties of the system under investigation[120], is more suitable. Inherently, AIMD simulations are extremely computationally expensive and therefore limited to a few hundred picoseconds[121]. Alternatively, hybrid quantum mechanics/molecular mechanics (QM/MM) simulations apply accurate quantum mechanics to a small region of interest, e.g., the binding pocket of an enzyme, while treating the remainder of the system with a classical force field[122].

Although great advances have been made, the availability of computational resources remains a limiting factor for MD simulations. Consequently, many MD studies apply simplifications to

the system under investigation[71, 123], while others explicitly focus on increasing the complexity of simulated systems[124].

Additionally, the timescales of many biologically relevant processes exceed the temporal range accessible to MD simulations. Therefore, as mentioned above, rare events that would not be observed in equilibrium MD simulations are investigated using advanced sampling techniques[125].

Chapter II - How can simulations aid our understanding of nanoparticle-mediated siRNA delivery?

The following chapter was published as an editorial in *Therapeutic delivery*:

Katharina M. Steinegger and Olivia M. Merkel*:
“How can simulations aid our understanding of nanoparticle-mediated siRNA delivery?” *Therapeutic delivery* vol. 16,7 (2025): 617-619.
doi:10.1080/20415990.2025.2505397

With artificial intelligence and simulation-based methods becoming more powerful, the increasing role of computational approaches in pharmaceutical research is undeniable. This includes Molecular Dynamics (MD) simulations, which have been under constant evolution since 1976[126]. As MD has already proven valuable in the design of small-molecule drugs and protein research, it is now emerging as a promising tool for the development of siRNA delivery systems as well.

Short interfering RNA (siRNA) is used to downregulate disease-driving genes within an organism, offering broad applications in treating cancer, autoimmune diseases, and other conditions. Yet, due to fast degradation of exogenous nucleic acids in the body, successful delivery of siRNA strongly depends on the formulation strategy. While good responses can be achieved with N-acetylgalactosamine (GalNAc) siRNA conjugates in the liver, other formulation strategies focus on the delivery *via* Adeno Associated Viruses (AAVs) or the encapsulation of siRNA into nanoparticles. The materials used for siRNA nanoparticles cover a wide range from inorganic gold nanoparticles, via the more prominent lipid nanoparticles (LNPs) to polymeric nanoparticles, particularly polyplexes. Regardless of which material the carrier systems are based on, they all have a complexity in common which makes the complete understanding of a formulations' behavior challenging. MD provides the potential to make molecular interactions, such as the internal organization of a nanoparticle, accessible while circumventing complex experimental methods such as x-ray scattering approaches.

All-atom (AA) MD simulations show the molecules of interest in single atom resolution. While this is a big advantage for the observation of details, it results at the same time in the major disadvantage of AA simulations: The high number of interactions the simulation must account for leads to a limitation concerning size of the simulated system and time span of the simulation. Nevertheless, AA MD studies reveal valuable details on nanoparticle formation. They can be used to investigate the direct interaction of polyplex-forming cationic polymers[127, 128] with nucleic acids, unveiling binding strengths between polymers and the cargo, as well as preferred binding sites[129] (e.g., major grove vs. minor grove of the siRNA). Other applications allow insights on how modifications of polymers, such as the addition of hydrophobic units to hydrophilic polyethyleneimines (PEI), change the particle performance[130].

Similarly, AA simulations are used in the development of LNPs. First, they can be applied to predict the degree of protonation of an ionizable lipid[31]. This is crucial for LNP design, as the pKa of a lipid within an LNP ("apparent pKa") can differ significantly from its pKa in solution. Second, insights on the geometry of lipid arrangements within an LNP[131, 132] won from AA MD strongly contribute to the understanding of LNP systems. However, AA models are hardly

capable of depicting polyplexes or LNPs at the full scale of experimentally observed nanoparticle sizes.

To access larger systems, coarse-grained (CG) force fields have been developed, the most popular being the Martini force field[97]. Coarse graining reduces the degrees of freedom in a simulation by reducing the resolution, as groups of atoms are summarized into beads with predefined properties such as degree of hydrophobicity or charge. With this approach, not only systems up to ~ 100 nm are simulated, but also timescales of tenths of microseconds are accessible. To avoid wrong conclusions based on observations introduced by the inaccuracies of a CG model, the simplified models must be validated against AA simulations and/or experimental data before further use. Some well-established polymers in nucleic acid delivery, e.g. PEI, have therefore been simulated as AA models[35] and as larger CG models[133]. Here, the CG approach allows to cover the whole range of experimentally used molecular weights of PEI. CG simulations also expand the knowledge gained from MD to include more formulation parameters, such as the role of different N/P ratios (i.e., the ratio of positive charges in the encapsulation agent to negative charges of the RNA). This sheds light on different stages of siRNA encapsulation or the presence of unproductive polymer in a polyplex formulation[134]. Similarly, CG simulations shape the understanding on how different ionizable lipids form LNPs with substantially different properties[109]. Other simulations visualize the changes in LNPs upon pH changes in the environment, including dehydration and rearrangement of lipids in an LNP when dialyzed towards neutral pH[135]. Backmapping from CG resolution to AA is the chance to combine the advantages of both: Assembling larger structures in CG MD and observing atomistic details in the final state after AA resolution was reapplied to the molecules. This method can, for example, be used to research the complex interplay of the different lipid types in an LNP[111].

As siRNA delivery does not end with the formation of a stable nanoparticle, efforts of MD research also expand to the interactions of nanoparticles in biological environments. A key application is the widely debated question of how carrier systems enable efficient endosomal escape of the siRNA, which is necessary for it to reach the site of action in the cytoplasm. Advanced microscopy methods provide valuable insights by tracking nanoparticles in combination with endosomal escape markers[136]. While these methods enable the correlation of particle properties with endosomal escape performance, they do not provide detailed information on underlying mechanisms. MD simulation is beginning to make the molecular process of endosomal escape observable[71, 109], allowing for more comprehensive understanding of mechanistic backgrounds. In this regard, the influence of lipid composition and charge in an LNP on its ability to fuse with endosomal membranes can be

visualized. Additionally, the role of different lipid types in the biological membranes can be more thoroughly discussed when made observable by a simulation[123].

With the rapidly growing number of publications in the field, the availability of tools and methods for faster preparation of simulations increases as well. For example, tools for automatic generation of membranes with desired composition[137, 138] or flexible protocols for building LNPs in CG resolution[109] are publicly available. Certainly, this will further contribute to the progression of MD simulation in the field of siRNA delivery.

It can be concluded that MD simulations aid our understanding of nanoparticle-mediated siRNA delivery by making processes visible and understandable on a molecular level. However, simulation data must always be carefully validated and compared to experimental results to avoid over-interpretation and false conclusions. For now, the strength of MD lies in elucidation and explanation of experimental observations, while the time where it replaces experiments in the development of siRNA delivery systems is yet to come.

Chapter III - Molecular Dynamics Simulations Elucidate the Molecular Organization of Poly(beta-amino ester) Based Polyplexes for siRNA Delivery

Katharina M. Steinegger[a], Lars Allmendinger[a], Sebastian Sturm[b,c], Felix Sieber-Schäfer[a], Adrian P. E. Kromer[a], Knut Müller-Caspary[b,c], Benjamin Winkeljann[a,c,d], Olivia M. Merkel*[,a,c,d]

[a] Ludwig-Maximilians-University Munich, Department of Pharmacy, 81377 Munich, Germany

[b] Ludwig-Maximilians-University Munich, Department of Chemistry, 81377 Munich, Germany

[c] Center for NanoScience (CeNS), Ludwig-Maximilians-University Munich, 80799 Munich, Germany

[d] Comprehensive Pneumology Center Munich (CPC-M), Helmholtz Munich, German Center for Lung Research (DZL), 81377 Munich, Germany

The following chapter was published as scientific article in *Nano letters*:

Katharina M. Steinegger, Lars Allmendinger, Sebastian Sturm, Felix Sieber-Schäfer, Adrian P. E. Kromer, Knut Müller-Caspary, Benjamin Winkeljann, Olivia M. Merkel*:
"Molecular Dynamics Simulations Elucidate the Molecular Organization of Poly(beta-amino ester) Based Polyplexes for siRNA Delivery." *Nano letters* vol. 24,49 (2024): 15683-15692. doi:10.1021/acs.nanolett.4c04291

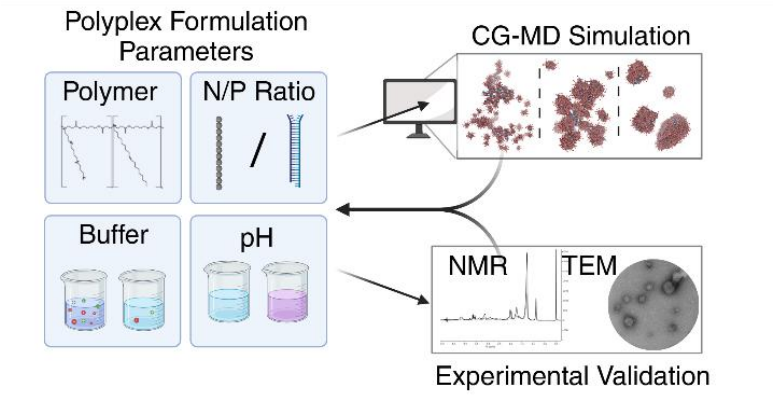

1 Abstract

Cationic polymers are known to efficiently deliver nucleic acids to target cells by encapsulating the cargo into nanoparticles. However, the molecular organization of these nanoparticles is often not fully explored. Yet, this information is crucial to understand complex particle systems and the role influencing factors play at later stages of drug development. Coarse-grained molecular dynamics (CG-MD) enables modeling of systems in the size of real nanoparticles, providing meaningful insights into molecular interactions between polymers and nucleic acids. Herein, the particle assembly of variations of an amphiphilic poly(beta-amino ester) (PBAE) with siRNA was simulated to investigate the influence of factors such as polymer lipophilicity and buffer conditions on nanoparticle structure. Simulations were validated by wet lab methods including nuclear magnetic resonance (NMR) and align well with experimental findings. Therefore, this work emphasizes that CG-MD simulations can provide underlying explanations to experimentally observed nanoparticle properties by visualizing the nanoscale structure of polyplexes.

2 Introduction

Short-interfering ribonucleic acid (siRNA) as therapeutic agent successfully entered the pharmaceutical market in 2018, with five FDA-approved products currently available[139]. Its mode of action is downregulation of transcription of disease driving genes *via* the mechanism of RNA interference (RNAi) in the target cells. However, while the demand for nucleic acid therapies is growing, all presently approved siRNA drugs target the liver[19, 140-142]. A major challenge therefore remains in finding delivery vectors[143], which enable efficient targeting to other organs and simultaneously avoid early degradation of the RNA.

The five marketed siRNA therapies rely either on lipid nanoparticles (LNPs) or conjugation to trivalent *N*-acetylgalactosamine (GalNAc) to assure delivery[139]. Besides viral vectors, alternatives for delivery vehicles include polymers. Cationic polymers encapsulate the negatively charged RNA mainly *via* electrostatic interactions[35], forming so called poly- or micelleplexes. Using polymers as delivery vectors provides certain advantages[144, 145], such as broad tunability and good biodegradability. Therefore, polycations are being investigated as nonviral vectors for safe and efficient delivery targeting a wide variety of diseases[146-149]. The explored materials cover a broad chemical space ranging from polyethyleneimines (PEI)[150, 151], *via* carbohydrates such as chitosan[152], to more complex molecular structures such as poly(beta-amino ester) (PBAE)s[153].

PBAEs were first introduced as polycationic vectors for plasmid DNA in the year 2000[154] and stand out due to their almost unlimited adaptability. Owing to a toolbox-like system, PBAEs allow various combinations of diacrylates for the backbone and amines as side chains of the molecular structure[155]. The introduction of amphiphilicity by combination of hydrophilic and hydrophobic side chains within one polymer was shown to improve colloidal stability[156]. Subsequently, amphiphilic poly(beta-amino ester) (PBAE)s, containing a varying ratio of polycationic spermine and lipophilic oleylamine (OA), have been identified as copolymers that successfully deliver siRNA, achieving particularly high knockdown efficiencies at low polymer-to-RNA ratios[157].

Understanding the internal organization of self-assembled polyplexes can help to identify relevant formulation parameters and to link these to the particles' physicochemical properties[35]. Subsequently, the intracellular behavior of polyplexes can further be elucidated[48, 71]. Experimental methods including Transmission Electron Microscopy (TEM)[35, 51] or Small-Angle X-Ray Scattering (SAXS)[158] have been applied to investigate particle shapes. Others have exposed the role of the molecular weight (MW) of PBAEs by explicitly screening its influence on knockdown efficiency[159]. Meanwhile, Molecular Dynamics (MD) simulations have developed into a powerful tool to be incorporated in the development of drug delivery systems[133, 160, 161]. Especially with the refinement of coarse-grained (CG) models, MD allows for simulating systems in the size of real nanoparticles up to 100 nm at timescales of several microseconds[135, 162].

Herein, PBAEs comprising spermine as polycationic moiety and OA as lipophilic component, have been mapped and parametrized in CG resolution in the MARTINI 3 force field[97].

3 Results and Discussion

The parametrization, based on the mapping (Figure III.1A), yielded distributions of bonded interactions in good agreement with the All-Atom (AA) reference (Figure III.S1A+B). The herein studied PBAE polyplexes are exposed to an acidic pH of 5.4 during polyplex formulation, a pH of 7.4 upon administration and again acidic pH after cellular internalization in the endosomal compartment[48]. According to the p*K*a values determined by Density functional theory (DFT), all amines of the polymer were protonated at pH 5.4. At pH 7.4, only the secondary amines and the tertiary amine of the OA linkage in the backbone were protonated (Figure III.1A). The remaining amines in the spermine moiety were considered deprotonated due to neighboring effects of the protonated secondary amines (Figure III.S2). PBAE models were generated for polymers with varying %OA between 10% and 85%. Initially, a molecular weight (MW) of

around 9 kDa was chosen. To account for possible influences of the MW, models with 4.5, 27, and 100 kDa were generated additionally. As the behavior of these models showed no notable differences upon particle formation in visible outputs and radial distribution functions (RDF) around RNA phosphates (Figure III.S3), further simulations were conducted with the 9 kDa models. Micelle formation of the amphiphilic polymer (Figure III.1B) was confirmed by TEM imaging (Figure III.1C), dynamic light scattering (DLS) (Figure III.1D), and a pyrene assay for critical micellar concentration (CMC) (Figure III.S4), with decreasing CMCs observed as the %OA increased.

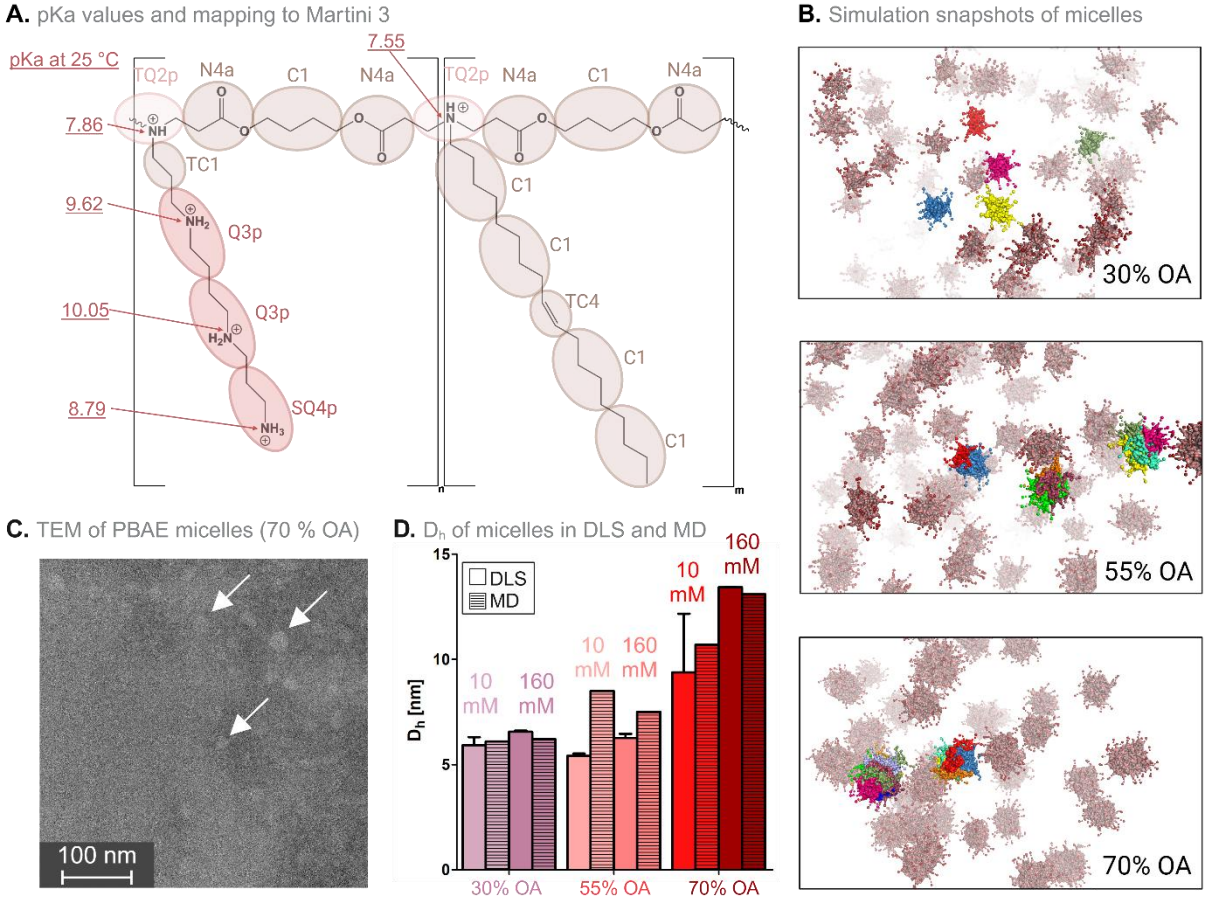

Figure III.1. PBAE mapping and model validation. A. Molecular structure and pKa values at 25 °C of the PBAE copolymer with a spermine (left) and oleylamine (right) subunit. Mapping to CG resolution within Martini 3 indicated by spheres. **B.** Simulation snapshots of 9 kDa polymers in 10 mM HEPES at pH 5.4, simulated for 2.5 µs. Lipophilic components in grey, charged beads in red. Exemplary coloring corresponds to one polymer molecule per color. **C.** Micelles formed of PBAE 70% OA as visible in TEM imaging. **D.** Comparison of hydrodynamic diameters in DLS and Simulation (MD) under low and high ionic strength buffer conditions. DLS results (n = 3) with mean ± SD of main peak below 20 nm by intensity. MD results are mean of Dh averaged over the whole box, calculated from mean square deviation (msd) between 1.75 and 2.25 µs simulated time.

To validate the behavior of the polymer models, setups with only PBAE in buffer were simulated and the average hydrodynamic diameter of micelles was calculated *via* mean square deviation (msd). The micelle sizes in simulation were in good agreement with DLS results (Figure III.1D) and followed the trend of increasing micelle size with increasing %OA of the polymer. Analysis of TEM images yielded a diameter of 18.8 ± 3.8 nm for the 70% OA polymer in 10 mM HEPES, which is larger than DLS (9.4 ± 2.8 nm) and simulation (10.7 nm). This deviation was attributed to the increased visibility of larger micelles in the TEM and unclear margins of single micelles. Another explanation can be an increased sample concentration in TEM making the formation of larger polymer aggregates more favorable, especially considering the high lipophilicity of the 70% OA polymer.

Previous *in vitro* experiments with this type of PBAE copolymer[157], and other PBAE-based studies[163] showed a strong influence of the polymers' amphiphilicity on knockdown or transfection efficiency. Hence, the %OA in the polymer was selected as a factor for in depth *in silico* investigation. Upon simulation of particle assembly, precursor micelles assembled within the first µs. Polycationic spermine moieties remained on the surface and established electrostatic interactions with the negatively charged phosphate beads of the siRNA (Figure III.2A). Over time, this led to the formation of nanoparticles. Unlike for the micelles, the particle sizes cannot be directly compared between simulation and experiment, as the simulation box does not contain enough material to form real sized nanoparticles.

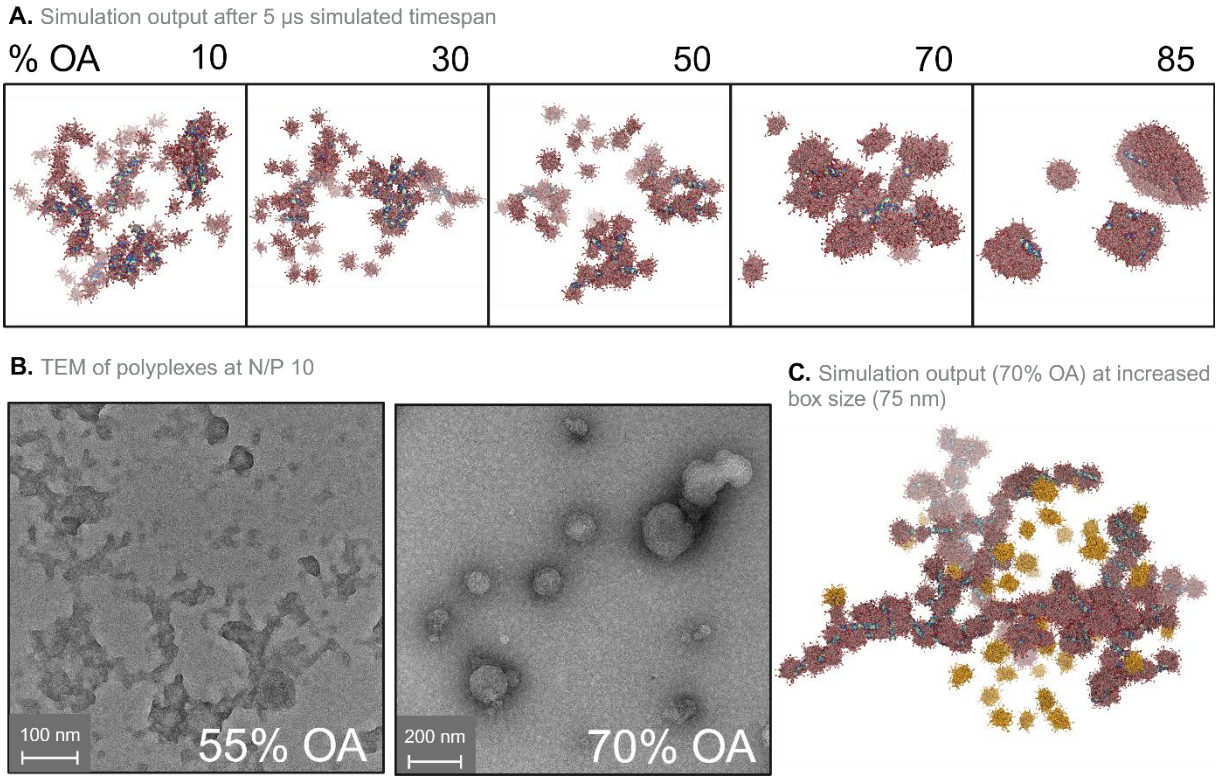

Figure III.2. Influence of polymer lipophilicity on particle morphology (in 10 mM HEPES, pH 5.4, at N/P 10). A. Simulation output after 5 µs of particle assembly with increasing lipophilicity, *i.e.*, %OA of the polymer (10%, 30%, 50%, 70% and 85% shown) from left to right. Polymers in grey/red, siRNA in turquoise. **B.** Particles formed with either 55% or 70% OA in TEM. **C.** Simulation output of particle assembly under the same conditions as in A. for 70% OA but in a cubic box with 75 nm side length, containing 99 siRNA molecules, 5 µs. Orange color represents polymer outside of siRNA containing particles.

Zhao et al.[129] demonstrated in an AA simulation setup the exclusive interaction of spermines with the major groove of siRNA. Notably, this exclusivity of interaction was not reproduced in our model (Figure III.S5), which could be attributed to the reduced mobility of the spermines anchored in the PBAE backbone at GC resolution. Shortcomings of the Martini 3 force field, including non-ideal nonbonded interactions[164], have been reported. Therefore, detailed small-scale interactions profit from the application of an AA simulation, whereas CG-MD is advantageous for large scale simulation setups due to the massive reduction of consumed resources.

The particle morphology was strongly influenced by the lipophilicity of the copolymer: Low %OA polymers formed undefined particles with rugged surfaces. Increasing the %OA led to irregular, “bead-on-a-string”-like particles, as previously described for other polyplexes[35, 51]. Only above 70% OA, compact particles formed (Figure III.2A). TEM images (Figure III.2B) confirmed a change in particle shape, with 55% OA polymer particles being irregularly shaped and 70% OA polymer particles appearing condensed. The differences in particle shape between MD and TEM in the range from 70-80% OA might be attributed to the limited time of

assembly during the simulations. The 70% OA, N/P 10 (ratio of PBAE-amines to RNA phosphates) particle assembly was therefore extended to 15 µs. However, the particle did only slightly condense further but did not reach a similarly compacted shape as observed in the corresponding TEM images (Figure III.S6). As particle assembly in wet lab experiments requires incubation times in the minute-range, the process could be too slow to be portrayed in simulation to the final state. To determine if the limited simulation size of the cubic 40 nm box does affect particle assembly, the 70% OA polymer was exemplarily simulated in a 75 nm box with 99 siRNA molecules (Figure III.2C). The RDF around RNA phosphates showed similar contact levels with amines and water (Figure III.S7) compared to the smaller setup, validating the use of the 40 nm box simulations.

The trends in particle shape were attributed to the capability of different polymers to form larger supramolecular assemblies, i.e., elongated micellar structures, spheres with RNA containing pores, or larger micelles in general. With increasing %OA, the total mass of polymer to achieve the same N/P ratio increases, as the number of charged spermines within the same total mass of polymer decreases. In the simulations, this was quantified as the number of spermines per nm^2 of the micelle core surface (Figure III.S8). With increasing %OA, the spermine density on the micelle surface decreased, therefore the repulsion between single micelles was reduced. Thus, larger polymer arrangements formed, and more compacted particle shapes were accessible.

The N/P ratio is often correlated with knockdown efficiency of siRNA polyplexes[35] and was shown to be of high impact for the characteristics of particles formed with the PBAEs[157]. Here, nanoparticles were prepared for polymers with 30%, 55%, and 70% OA at N/P ratios 1–10 and the polymers' encapsulation efficiencies were assessed. Z - average and PDI (Figure S9A) confirmed the formation of small (< 100 nm) and monodisperse (PDI < 0.2) nanoparticles for all polymers within an optimized N/P range. The ζ-potential increased with increasing N/P ratio from below 0 mV to maximum values around 20 mV. All formulations benefited from an N/P ratio where the ζ-potential (Figure III.S9B) was positive. In contrast, in the N/P range around charge neutrality, standard deviations for z - average and PDI were high due to aggregation tendencies of the nanoparticles. The PDI was lowest just above charge neutrality and increased with the addition of more polymer, arguably due to the formation of excess micelles as a second species. This indicated an optimal N/P ratio of 5–6 for the 30% and 55% OA polymers, while the 70% OA polymer formed the smallest and most monodisperse particles at N/P 7–10. This observation corresponds well with the N/P values at which full encapsulation was reached: Figure 3A shows that for 30% and 55% OA, full encapsulation was achieved at N/P ~ 4, with no notable difference between the two polymers. The more lipophilic polymer (70% OA) reached full encapsulation at an N/P ratio around 6.

Subsequently, MD simulations were conducted with the same polymers at N/P ratios from 1 to 15. The encapsulation efficiency within the simulations was quantified *via* the area under the curve (AUC) of RDF for the water contacts of the RNA surface (Figure III.S10). Figure III.3B shows a decrease of water contacts until N/P 4 is reached for all polymers, which fully corroborates the experimental results for 30% and 55% OA. Conversely, the difference of encapsulation efficiency for the 70% OA polymer between N/P 1-5 was not reproduced. As observed with the results for particle morphology, this suggests inaccuracies of the CG-MD approach in the middle to high %OA range.

It was however visible in the simulation output that particles formed by the hydrophilic polymers (30% and 55%OA) contained more spermine moieties on the particle surface at low N/P ratios (Figure III.3C, N/P 3 and 5). These spermines were not in reach of any RNA backbone and did therefore not contribute to RNA complexation. Instead, they formed a charged corona on the particle surface. The simulations thus provide an explanation for the transition from negative to positive ζ-potential at lower N/P ratios for particles with lower %OA PBAEs. Again, the observed effect can be attributed to limited possibilities for supramolecular arrangement of the polymer within the smaller micelles[161].

Further, the choice of N/P ratio is of high relevance as an excess of unnecessary excipients can promote side-effects[165-167]. Figure III.3C shows the first appearance of free, excess polymer at N/P 5 for 30% OA and N/P 7 for 55% and 70% OA. The amount of free polymer, and from that, the stoichiometry (i.e., effective N/P ratio) in MD simulations was quantified for all polymer models between 10% and 85% OA at N/P 10 in different buffers (Figure III.4A). The trend clearly suggests that the more lipophilic the polymer, the higher the amount polymer bound per siRNA, leading to higher effective N/P ratios.

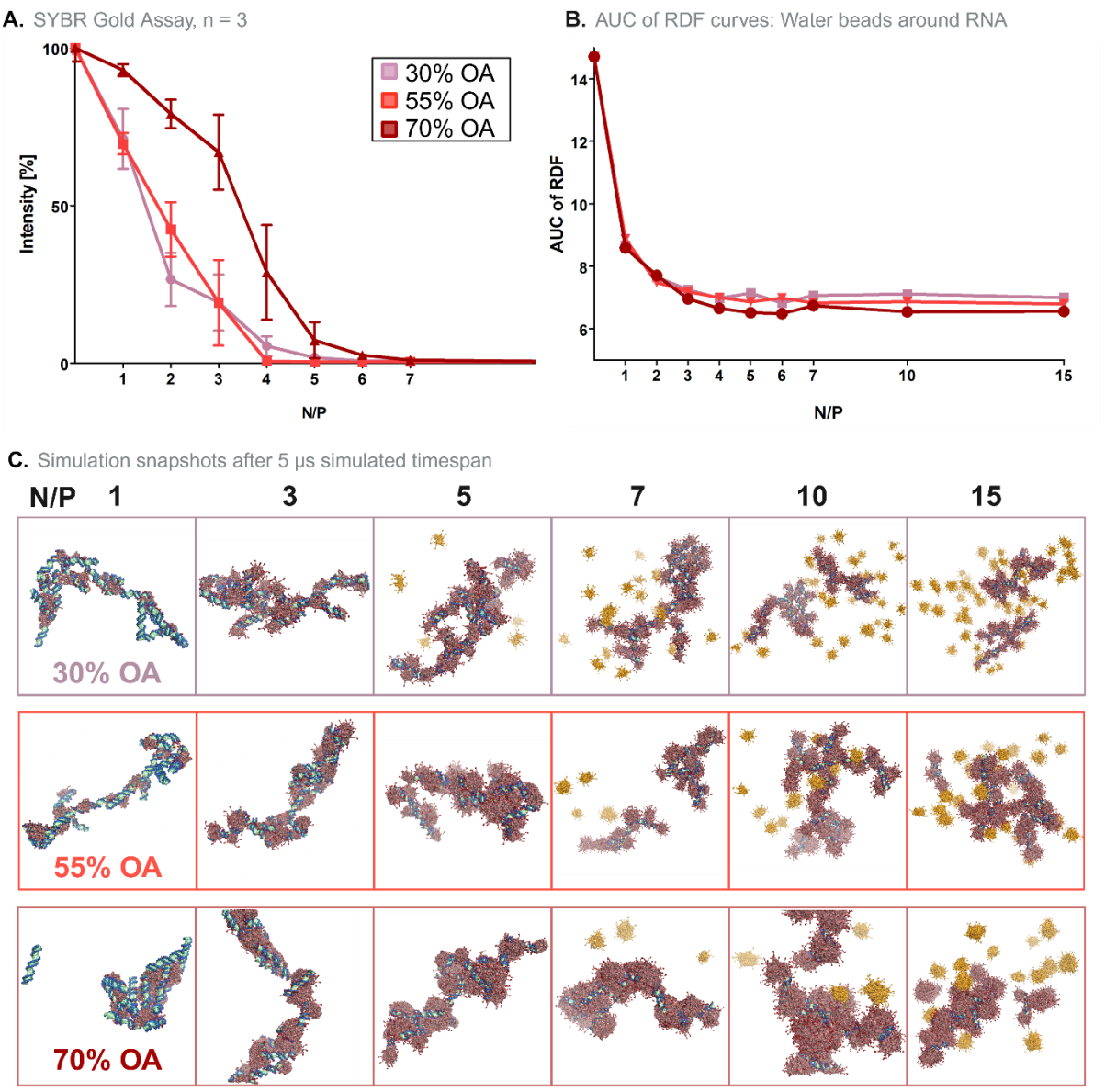

Figure III.3. Nanoparticles at different N/P ratios. A. Encapsulation efficiency experimentally assessed by SYBR Gold assay, n = 3, shown as mean ± SD. **B.** Area under the curve (AUC) of radial distribution functions (RDF) within 0.6 nm of the RNA surface, indicating the decrease of water contacts of the RNA with increasing N/P ratios. **C.** Simulation output after 5 µs simulated particle assembly with increasing N/P ratios from left to right, simulated with 30%, 55% and 70% OA polymers. Excess polymer (outside of RNA containing particles) shown in orange.

These simulation results were validated by ^{1}H nuclear magnetic resonance (NMR) spectroscopy. By titration of an siRNA sample with increasing amounts of PBAE and measurement of an ^{1}H NMR spectrum after each step, new signals referring to excess polymer were identified above certain N/P ratios (Figure III.4B). After the addition of the first PBAE to the siRNA, additional signals appeared incrementally. Assuming that the polyplex signals are not visible due to severe line broadening resulting from short transverse relaxation times (T_2), these signals were attributed to dangling residues on the polyplex surface[168]. In comparison to the peaks of PBAE only samples and samples with high N/P, these signals are slightly shifted towards higher ppm. At high N/P ratios, the most prominent signals showing a constant increase in intensity were signal A, B, C and D (Figure III.4B+C). Signals A and B can be exclusively attributed to the OA[169, 170] within the polymer (Figure III.S11).

The appearance of free polymer at high N/P ratios was confirmed by 2D NOESY experiments. These are based on the nuclear Overhauser effect (NOE), used to detect spatial proximity of protons/ the chemical exchange of protons in different chemical environments[171, 172]. This type of experiment was performed with samples containing RNA and 70% OA polymer at N/P 7 or 15 (Figure III.S12). First, reference spectra containing only PBAE were analyzed. Very intense intramolecular NOEs are present, mainly originating from the OA moiety of the polymer. At N/P ratio of 7, all intramolecular NOEs nearly collapse or are not visible at all due to the extreme line broadening. This may be due to either the sole presence of a giant supramolecular assembly *i.e.*, polyplexes with low tumbling rates leading to drastically increased transverse relaxation rates (R_2), or transitions between free and bound states with significantly different chemical shifts in the slow intermediated exchange regime on the NMR timescale[173]. These findings are in good agreement with the *in silico* results indicating that an N/P ratio around 7 represents a stoichiometric inflection point in polyplex formation with 70% OA PBAE. Finally, if a relatively large excess of polymer is obtained (N/P 15), the NOEs previously present in the reference spectrum (PBAE only) become visible again.

Both methods (NMR and CG-MD) implied that the stoichiometry within the particles no longer increased linearly with the theoretical N/P ratio (Table III.S1, Figure III.S13). Instead, the effective N/P ratio in 10 mM phosphate buffered saline (PBS) reached a threshold of about 9 for 70% OA polyplexes and about 6 for the 30% OA PBAE particles.

The good agreement between NMR results and effective N/P ratios from MD simulations (Figure III.4D) highlights the accuracy of the MD model. The strongest deviation between NMR and MD results was measured in high ionic strength buffer (150 mM PBS in NMR or 160 mM HEPES buffered saline (HBS) in MD) at an input N/P ratio of 15. Here, MD results imply nearly full binding of the 70% OA polymer. This trend towards higher effective N/P ratios in high ionic strength buffers was consistent throughout all simulations (Figure III.4A). However, by NMR

no significant difference was observed at N/P = 15 between particles formed in high or low ionic strength buffer with 70% OA PBAE (Figure III.4D).

Notably, concentrations in MD simulations were about 100x higher than in experimental setups, which might have contributed to the observed deviation between NMR and MD results. Additionally, the reaction field (rf) algorithm used to handle electrostatic interactions in the MD setup comprises a tradeoff with improved computational performance but reduced accuracy of the simulation, as it uses a coulomb cutoff beyond which the dielectric constant of the system is treated as uniform[174]. This leads to poorer treatment of long range electrostatics in comparison to e.g. the Particle Mesh Ewald algorithm (PME)[175]. Still, ionic strength of the medium is known to often influence colloidal stability and size of nanoparticles[176, 177] and will therefore be further discussed below.

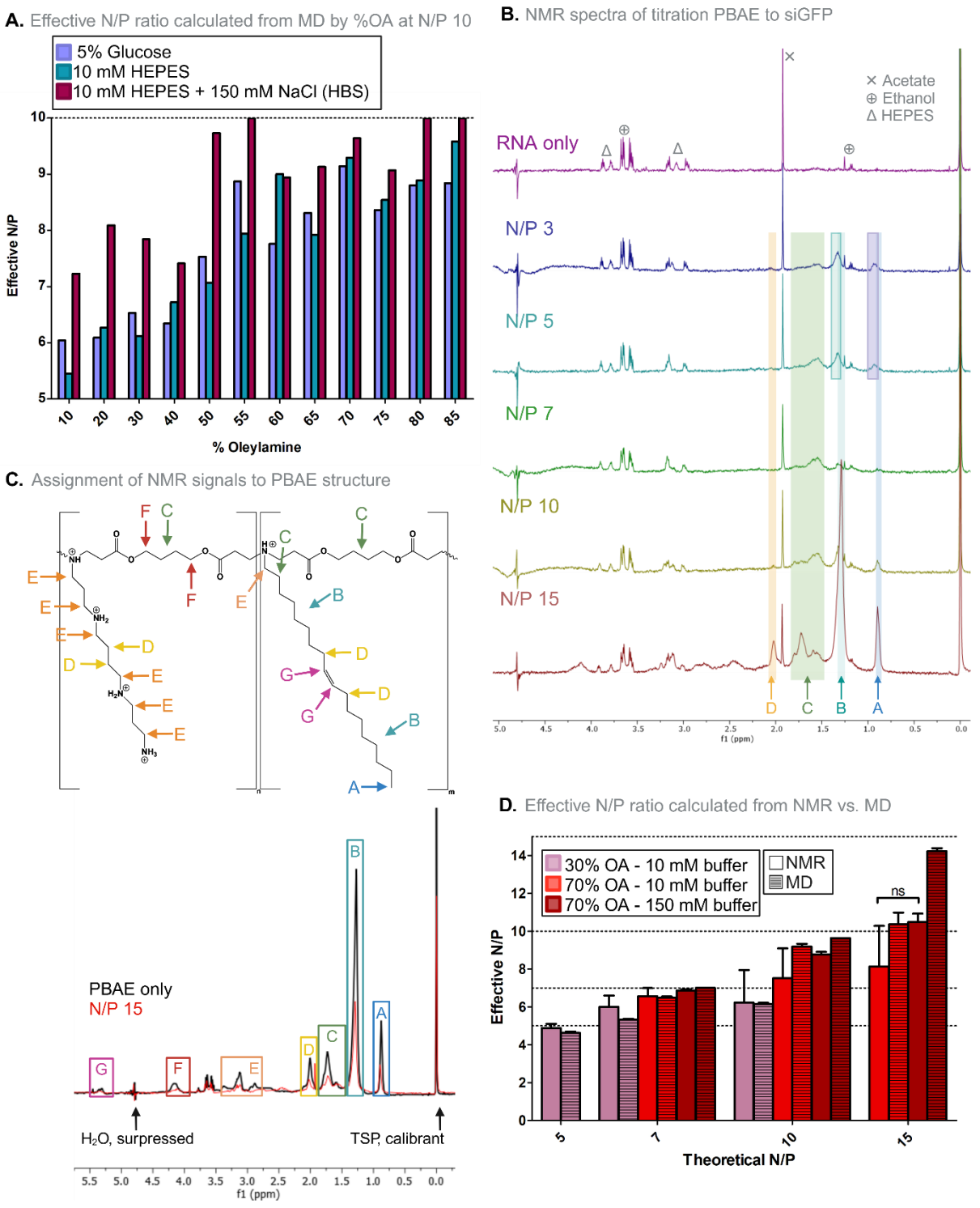

Figure III.4. Simulation validation by NMR. A. Effective N/P ratio calculated from MD (n = 1) at an input N/P ratio of 10. Simulated for polymers from 10% to 85% OA in 5% Glucose, 10 mM HEPES or 10 mM HEPES + 150 mM NaCl (= HBS). **B.** ^{1}H NMR spectra with water suppression (10 mM PBS, pH 5.4, 10% D_2O/H_2O). N/P ratios increase from top to bottom by stepwise addition of 70% OA polymer to the sample. Signals with most prominent changes upon titration marked by boxes. **C.** Excerpt of chemical structure of PBAE, signal assignment and overlay of ^{1}H NMR spectra of N/P 15 and PBAE only; NMR conditions as described under A. **D.** Effective N/P ratio calculated from NMR (n = 3, mean ± SD) in comparison to MD (n = 2, mean).

To determine the influence of buffer excipients, particles were formulated at N/P 10 in three different buffers/solutions at pH 5.4: 5% Glucose, 10 mM HEPES, and 160 mM HBS. DLS measurements revealed a shift towards larger particles (Figure III.5A) with higher ζ – potential (Figure III.S14) at high ionic strength of the medium, independent of lipophilicity of the used polymer. Although no significant difference between 5% Glucose and 10 mM HEPES concerning size and ζ – potential was observed, the presence of ions at higher concentrations (HBS) caused significantly larger particles with hydrodynamic diameters of above 400 nm. In MD simulation, visually more compact particles formed (Figure III.5B) and, as discussed above, the effect of ionic strength resulted in higher effective N/P ratios.

The presence of more ions in the hydrodynamic shell of the PBAE micelles alters the repulsive forces upon particle assembly. Reduced colloidal stability and altered particle shapes are therefore to be expected. Furthermore, surface charge of nanoparticles is known to alter their interaction in physiological environments e.g., with proteins in serum[178]. Ultimately, this influences cellular uptake and intracellular trafficking[67, 179, 180].

When the particle contains functional groups with p*K*a values in physiological ranges, pH changes in the surrounding medium will alter the particle charge and its interactions with the environment[181]. To mimic these changes in the simulation, pH values of 5.4 (formulation), followed by pH 7.4 (administration), and again pH 5.4 (endosome) were applied *via* an adjustment of the protonation state of the polymer[135]. Increasing the pH to 7.4 caused condensation of the particles, as the decreased charge on the micelle surface allowed for a rearrangement of the micelles into larger supramolecular structures (Figure III.5C). These changes reduced the water contacts of the RNA phosphates (Figure III.5D) but increased the contacts with amines. In contrast to CG-MD observations made on lipid-based RNA carriers[135], the pH increase did not cause expulsion of RNA from the particle. After the pH was reduced again, the particles rearranged but primarily maintained the agglomerated shape. However, the microenvironment around the phosphates restored to the level as before the pH changes- for both water and amine contacts. Especially for high %OA particles, the shapes resulting after the pH changes align better with the TEM images (Figure III.2B, Figure III.S6) than before. It could therefore be argued that the pH changes speed up the process of particle condensation, which is otherwise too slow to be simulated to a final state. The readjustment to pH 5.4 was accompanied by a moderate swelling of the polyplex, which was hypothesized previously to play a role in endosomal escape[67].

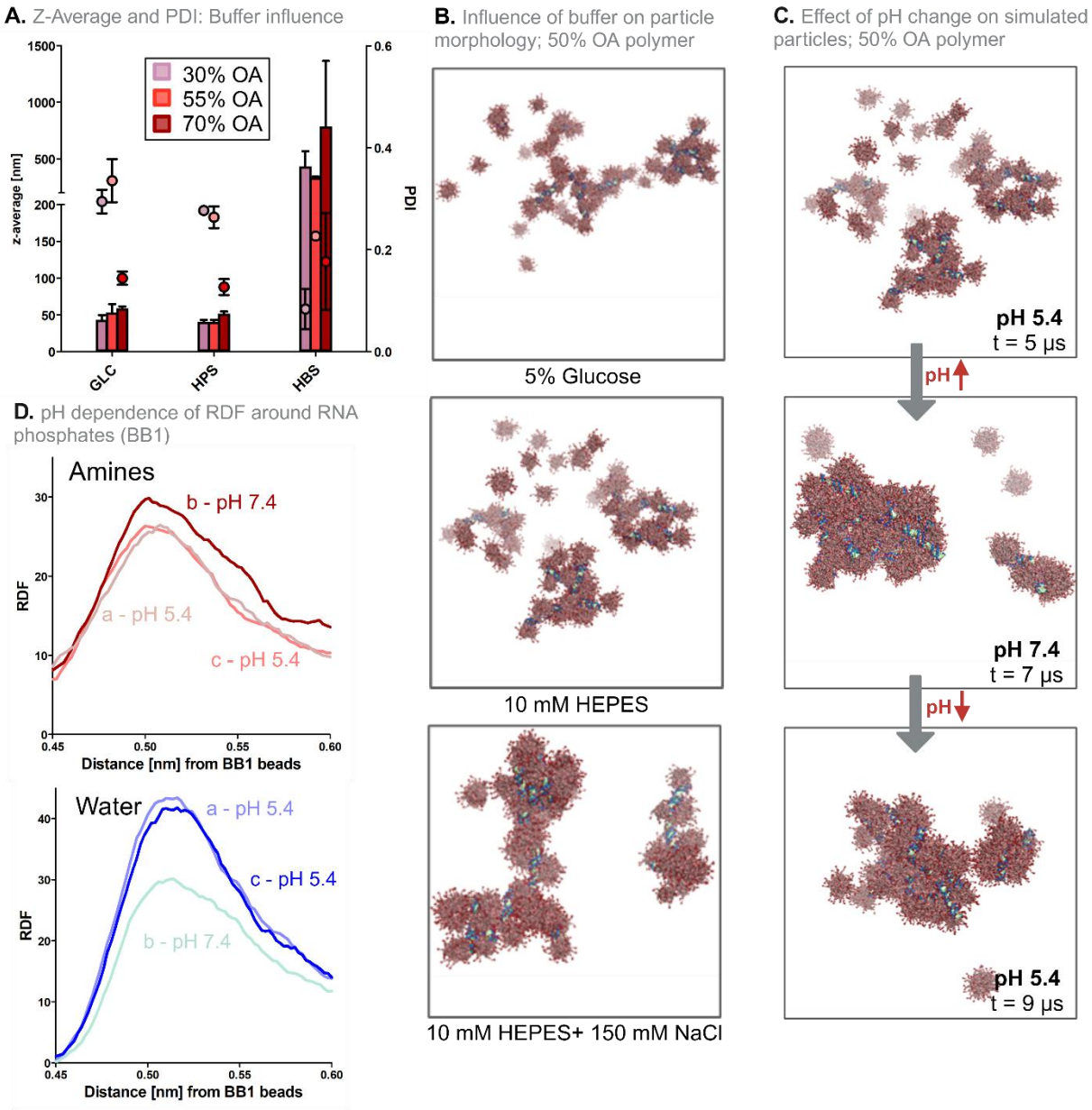

Figure III.5. Influence of buffer conditions on PBAE polyplexes. A. Last frame of simulated particle assembly (5 µs) in different buffers. **B.** Z-average (bars) and PDI (dots) of polyplexes at N/P = 10 in 5% Glucose, 10 mM HEPES or 10 mM HEPES + 150 mM NaCl (= 160 mM HBS), all pH 5.4. n = 3, mean ± SD. **C.** RDF of amines of 50% OA PBAE and water around RNA phosphate beads a) after initial particle assembly b) after pH increase to pH 7.4, and c) after subsequent reduction of the pH back to 5.4. **D.** Visualization of changes in particle structure after simulation of subsequent pH changes (assembly at pH 5.4 for 5 µs, equilibration at pH 7.4 for 2 µs, equilibration back to pH 5.4 for 2 µs).

With a combinatorial approach of CG-MD simulation and experimental validation, experimentally observed influences on polyplex structure were explained on a molecular level. Our CG-MD approach did not suggest a pronounced effect of MW of the polymer for the investigated PBAEs. Instead, lipophilicity of the PBAE was identified to be the main influencing factor on particle shape - reflected by the charge, density, and mobility of spermines on the surface of polymeric micelles. Polyplex morphology may strongly affect cellular uptake and endosomal escape[182]. Hence, the demonstrated influence of lipophilicity of the polymer should be carefully considered when designing amphiphilic PBAEs. Structural alterations of polyplexes were also observed through changes of pH and ionic strength of the medium. Furthermore, with CG-MD and NMR, two methods were introduced to determine the critical N/P_{max} for every %OA. Further increasing the N/P in the formulation did not significantly increase the stoichiometry within the particles. PBAEs are a heterogenous group of polymers, varying not only in lipophilicity, but e.g. also backbone rigidity or side-chain architecture. Similar simulation setups could therefore be applied to other PBAE structures, allowing for a more extensive comparison of the polymers.

Future work will have to show, how the herein found differences between polyplexes of varying lipophilicity and structure are linked to their differing behavior in vitro and in vivo. A quantitative approach that directly links *in silico* data to *in vitro* data is however a major hurdle, as the simulation of whole cells, including their active mechanisms and pathways, is not possible yet[100]. Still, future simulations could provide underlying explanations for differences in biological interaction (e.g., endosomal escape)[71].

In this work, despite minor limitations in reproducing experimental results at high %OA, computational results were generally consistent with experimental findings. By comparing experiments with CG-MD simulations, this study clarifies the molecular organization of PBAE polyplexes and demonstrates the utility of CG-MD in developing drug delivery systems.

4 Methods

4.1 Chemicals

All PBAEs were synthesized in house as described previously[55]: In brief, 1,4-butanediol diacrylate (TCI, Japan) as the backbone was polymerized in a Michael-addition step-growth polymerization with spermine (Fisher Scientific, Acros, USA), protected as tri-boc spermine, and oleylamine (Fisher Scientific, Acros, USA). Tri-boc spermine was deprotected with trifluoroacetic acid (Fisher Scientific, Acros, USA) and products were purified by gel chromatography. Amine-modified siRNA for the knockdown of eGFP ((5´- pACCCUGAAGUUCAUCUGCACCACcg, 3´- ACUGGGACUUCAAGUAGACGGGUGGC), siGFP) was obtained from Integrated DNA Technologies (Leuven, Belgium). HEPES (4-(2-

hydroxylethyl)-1-piperazineethanesulfonic acid), Dulbecco's Phosphate Buffered Saline (PBS), D-Glucose, sodium chloride, deuteriumoxide (D_2O) and 3-(trimethylsilyl)propionic-2,2,3,3-d_4 acid sodium salt (TSP) were obtained from Sigma-Aldrich (Taufkirchen, Germany), while SYBR Gold dye was bought from Life Technologies (Darmstadt, Germany). Water was MilliQ quality produced by an in-house installation.

4.2 Calculation of pKa values by Density Functional Theory (DFT)

To choose appropriate protonation states for the amine beads of the polymer in the MD models, p*K*a values were determined by density functional theory (DFT) with the B3LYP version. The 6311G+(d,p) basis set was applied using the *Gaussian 16W* software to optimize the geometry of four states (protonated in water, protonated in vacuum, unprotonated in water, unprotonated in vacuum) of a polymer fragment to minimum electron density. With the obtained sum of electronic energies within each state, p*K*a values were calculated applying a thermodynamic cycle as described elsewhere[183]. All protonable amines within the polymer structure were considered at 25 °C and 37 °C. After identifying the amines with the highest p*K*a values (i.e., the amines that will most likely be protonated first), the effect of their protonation on the p*K*a of neighboring amines was further investigated with the same approach.

4.3 Molecular Dynamics (MD) Simulations

Parametrizations

All CG simulations were run using the Martini 3 force field[97] within GROMACS 2021.4[184]. The siRNA model for siGFP was adapted from our previous publication[133] by incorporating the RNA backbone parametrization recently published[135] for Martini 3. To obtain models for the PBAE, a dimer (one spermine subunit and one OA subunit) was parametrized and mapped to be used in the Martini 3 force field. To do so, the protocol suggested by the Marrink – Lab on the Martini website (*cgmartini.nl/index.php*) was followed, using the proposed tools to generate input files[185-189]. Similarly, a HEPES model was created to be used as buffer substance in the production simulations (Figure S15). To create polymer models from the parametrized dimer, a python script was created, which automatically generates the necessary input files for desired MW and %OA based on the initially obtained bonded interactions.

Shear viscosity of simulated solvents

As the hydrodynamic diameter of micelles in the simulation was calculated via the Stokes-Einstein–equation[190], shear viscosities for the simulated buffers were required. The shear viscosities at 298 K for standard Martini 3 water, 10 mM HEPES, 5% Glucose[106] and 10 mM

HEPES + 150 mM NaCl (HEPES–buffered saline, HBS) were calculated via the periodic perturbation method[191], using the “cosine acceleration”(cos. acc.) option in GROMACS and analysis via the *gmx energy* tool. Each solvent was simulated in boxes with 12x12x23 nm^3 size with five different cosine accelerations ranging from 0.001 $nm*ps^{-2}$ to 0.005 $nm*ps^{-2}$. Shear viscosities [mPa*s] were then calculated via extrapolation to cos. acc. = 0 $nm*ps^{-2}$. Viscosity results are shown in Table III.S2 and Figure III.S16.

Production runs

Unless stated otherwise, all simulations were run in a cubic simulation box with 40 nm side length and periodic boundary conditions. The boxes were set up by random placement of siRNA and polymer molecules, subsequent addition of ions or other excipients (HEPES/ Glucose[106]) and solvation with standard Martini 3 water[97].
The standard setup for the simulation of polyplex assembly contained 15 siGFP molecules. Individual simulations were additionally tested in a larger setup comprising 99 siGFP molecules in a cube with 75 nm side length. PBAE molecules were added as needed to reach the desired N/P ratio (i.e., ratio of protonable units in the polymer to RNA phosphates) (eq. 1):

$$n(PBAE) = \frac{n(siGFP) * 50 * N/P}{n(charges/PBAE{-}molecule)} \quad (1)$$

Unless stated otherwise, simulations were run at 298 K in 10 mM HEPES with the protonation state of the polymer corresponding to pH 5.4 – the typical conditions for experimental polyplex assembly.[157]
All boxes were minimized in 15 000 steps employing the steepest descent method, followed by an NPT equilibration with 100 000 steps at a timestep of 5 fs. The run settings for the production runs were derived from the settings introduced in the Martini Tutorials: Electrostatic interactions were controlled by the reaction field algorithm with a relative permittivity of $\varepsilon_r = 15$ and a cutoff of 1.1 nm. Temperature was handled by the velocity rescale thermostat, while pressure was controlled by the Parinello-Rahman barostat [192, 193]. The timestep was reduced to 10 fs to ensure numerical stability for all simulations. Analysis was conducted with inbuilt GROMACS functions (*gmx rdf*, *gmx clustsize*, *gmx energy*), MD Analysis tools[194, 195], msd analysis[196, 197], and density based object completion[198].

4.4 Wet Lab Methods

Polyplex Formulation and Characterization

All polyplexes were prepared by batch mixing as described previously for this group of poly(beta-amino ester)s[55, 157, 166]: PBAE was dissolved in the respective buffers at 2.5

mg/ml. Subsequently, the polymer was diluted to a concentration where 50 µl contain the number of protonable units needed for 50 pmol siGFP at the desired N/P ratio (eq. 2):

$$\frac{n(protonable\ units\ PBAE)}{50\mu l} = 50\ pmol * 52\ (\frac{phosphates}{RNA}) * N/P \qquad (2)$$

siGFP was diluted to a concentration of 1 nmol/ml, to facilitate batch mixing with the respective PBAE solution at a ratio of 1:1 (w/w), yielding a final siRNA concentration of 500 pmol/ml. After batch mixing, the particles were incubated at RT for at least 90 min before characterization. Size- and ζ - potential were measured on a Malvern Zetasizer Ultra (Malvern Instruments, Malvern, UK). The encapsulation efficiency was assessed by SYBR Gold assay[166]: Particles were prepared as described in a range from N/P = 1 to N/P = 10 and transferred as triplicates to black 384-well plates with a volume of 20 µl per well. SYBR Gold stain was diluted 1:2000 and 3 µl of the final dilution were added to each well. Fluorescence resulting from intercalation of the dye into the RNA backbone was measured on a TECAN Spark Plate Reader (Tecan Trading AG, Switzerland) at 492 (20) nm excitation and 537 (20) nm emission. siGFP at the respective concentration (500 pmol/ml) without the addition of polymer was set to reference 100% free siRNA. Particle preparation and characterization was conducted in triplicates (n = 3).

Critical Micellar Concentrations (CMC) by Pyrene Assay

The critical micellar concentration (CMC) of polymers covering the %OA range from 12% to 75% was determined by the pyrene assay[199]. Pyrene was dissolved in acetone at a concentration of 1.2 mM, diluted 1:500 into glass vials and left for the acetone to evaporate overnight. Afterwards, a dilution series of PBAE between 0.5–1500 µg/ml was prepared in these vials and incubated in the dark for 24 h. After incubation, fluorescence spectra covering the range from 300 to 350 nm (step size 1 nm, bandwidth 20 nm) were measured on a TECAN Spark Plate Reader (Tecan Trading AG, Switzerland) using black 96-well plates, an emission wavelength of 397 (20) nm. Finally, the spectra were analyzed by calculating I_{345}/I_{330} and plotting of these values against log (c [µg/ml]).

Transmission Electron Microscopy (TEM)

Polyplexes were imaged by transmission electron microscopy (TEM) using a FEI Titan Themis 60-300 microscope (Thermo Fisher Scientific, Schwerte, Germany) as described previously[166]. The particles were prepared with either a 55% OA or a 70% OA polymer at N/P = 10 in 10 mM HEPES (pH 5.4) at a concentration of 6.1 µM siRNA. Micelles formed by PBAE 70% OA were imaged at a concentration of 2.5 mg/ml. For 10 min, 10 µl of sample were placed on a copper grid. Excess liquid was removed with a lint free tissue and next the grid

was stained with 2% (w/v) phosphotungstic acid (PTA) as negative stain. After removal of the excess dye solution, grids were left to dry for at least 15 min before imaging. The diameter of micelles in TEM images was measured in ImageJ (total 275 micelles from three images).

1H Nuclear Magnetic Resonance (NMR)

Calculation of excess polymer and therefore, "real" N/P ratios *via* the application of nuclear magnetic resonance (NMR) was inspired by a previously published method[168]. NMR measurements were recorded on a Bruker Avance III HD 500 MHz spectrometer equipped with a broad band observe 5-mm BB-H&FD CryProbe Prodigy (Bruker BioSpin GmbH, Ettlingen, Germany).

All 1D ^{1}H NMR spectra were recorded at 25 °C with a standard water suppression pulse sequence (zgesgp) from the Bruker pulse program library using excitation sculpting. The π/2 pulse length was 10.4 µs. The spectra were acquired with 64K data points, an acquisition time of 1.64 s, a relaxation delay of 2 s, and 16 transients.

For titration of polyplexes, siGFP was dialyzed against 150 mM PBS (pH 7.4) and diluted in 10 mM or 150 mM PBS (pH 5.4) to a concentration of 2700 pmol/ml. 10% D_2O were added as well as 0.036 mg/ml TSP as reference standard. PBAE was dissolved in the respective buffer to reach a concentration that contains (1500 * 52) pmol protonable units per 6 µl PBAE stock. This results in titration of N/P +1 per 6 µl PBAE stock added to the NMR sample. The total volume of the start-samples (RNA only, "N/P" = 0) was 550 µl. Titration was achieved by pipetting the PBAE stock solution into the tube, followed by mixing with a vortex. For measurement of PBAE only, the amount of siGFP stock added was replaced by buffer. A schematic overview of the titration NMR experiment can be found in Figure III.S17A.

For analysis, the most prominent peaks originating from the OA moiety (peaks A and B, see Figure 4C) were integrated using *MestReNova 15.0.0* software. First, all spectra were processed by automatic phase and baseline correction (Bernstein Polynomial Fit). Subsequently, PBAE only samples were analyzed by automatic peak identification and subsequent automated integration. The integration ranges were reused for the integration of the peaks in the polyplex samples to ensure consistency and reproducibility. For each condition (30% OA in 10 mM PBS; 70% OA in 10 mM PBS or 150 mM PBS) linear regression of the integrals (Figure S17B) of samples without siGFP was conducted.

The effective N/P ratios were then calculated according to eq. 3:

$$effective\ N/P = N/P_{input} - ((\int Peak_{sample} - \int Peak_{RNA-Ref})/s) \qquad (3),$$

with *s* being the slope of the corresponding linear regression, conducted on the PBAE only samples. Finally, the effective N/P was averaged over peaks A and B, which refer to the OA moiety and provided the most consistent results.

2D NOESY spectra

The 2D NOESY spectra were recorded at 25 °C with a phase-sensitive pulse sequence with water suppression employing an excitation sculpting element from the Bruker pulse program library (noesyesfpgpphrs). Data acquisition was performed with 1K (F2) x 512 (F1) data points and a mixing time of 0.1 s. The recycling delay was 1.0 s and 32 transients per increment were applied at a sweep width of 6 kHz in both dimensions resulting in an acquisition time of 0.1204 s. The special acquisition parameters regarding the water suppression element of the pulse sequence were adopted from the optimized parameter set of the respective one-dimensional experiment. A 90° shifted sine-square multiplication and an exponential window of 2.0 Hz in both dimensions in both dimensions prior to FT and zero filing was applied to yield a final symmetrical 2D matrix of 1K x 1K data points.

Data analysis and visualization

Data plotting, linear regressions, and -where applicable- statistical analysis (unpaired t-test, statistical significance defined as $p < 0.05$) were performed in GraphPad Prism (version 5.0, GraphPad Software, Inc., Boston, MA). Simulation output was visualized in PyMOL (version 2.5, Schrodinger, Inc., New York, NY). Some figures shown herein include elements created with BioRender.

5 Acknowledgments

O.M.M. acknowledges funding from the European Research Council (ERC-2022-COG-101088587). This work was supported through the Leibnitz Supercomputing Centre in the framework of the project *AVOCADO - AdVanced fOrmulation using Coarse grAineD mOdelling* to B.W.. Additionally, we thank Jonas Binder for valuable input concerning the CG-MD work.

6 Supporting Information

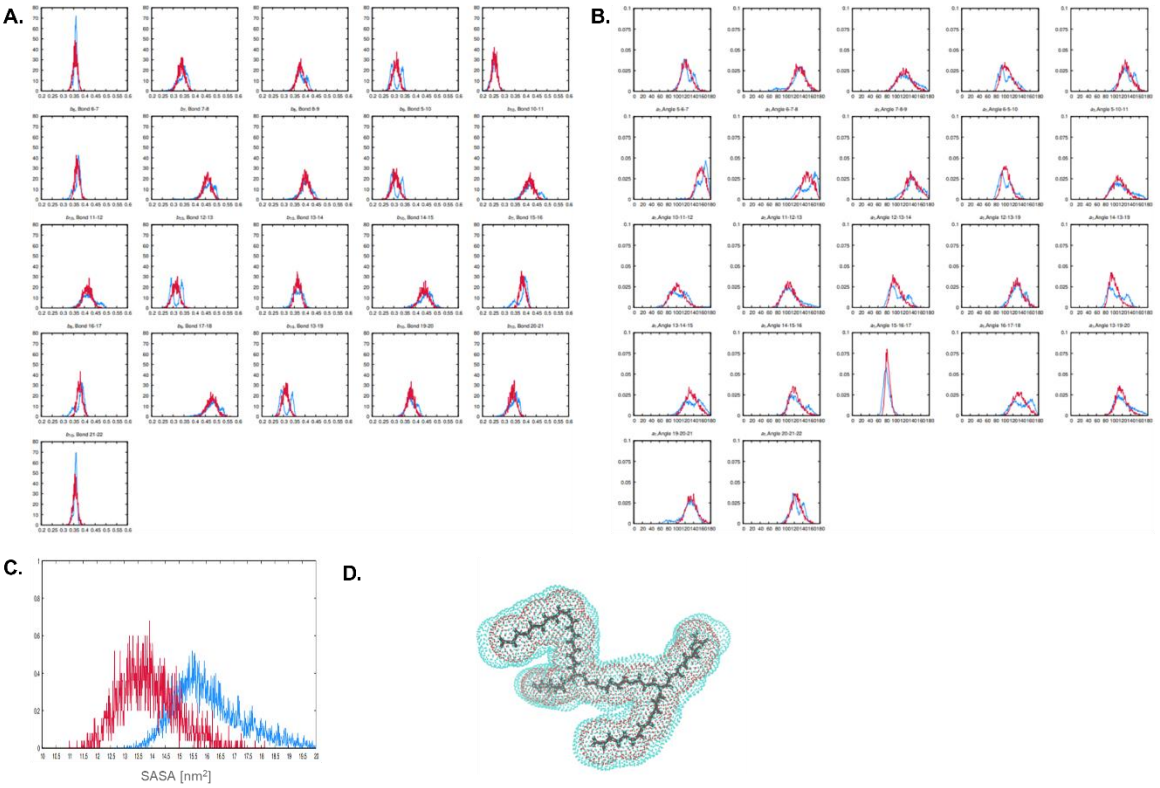

Figure III.S1. Distributions of A. bonds **B.** angels and **C.** distribution of solvent accessible surface area (SASA) within the parametrization of the PBAE dimer. Blue: distributions in the AA model, red: distributions of the CG model in Martini 3. **D.** Visualization of the SASA for the PBAE dimer.

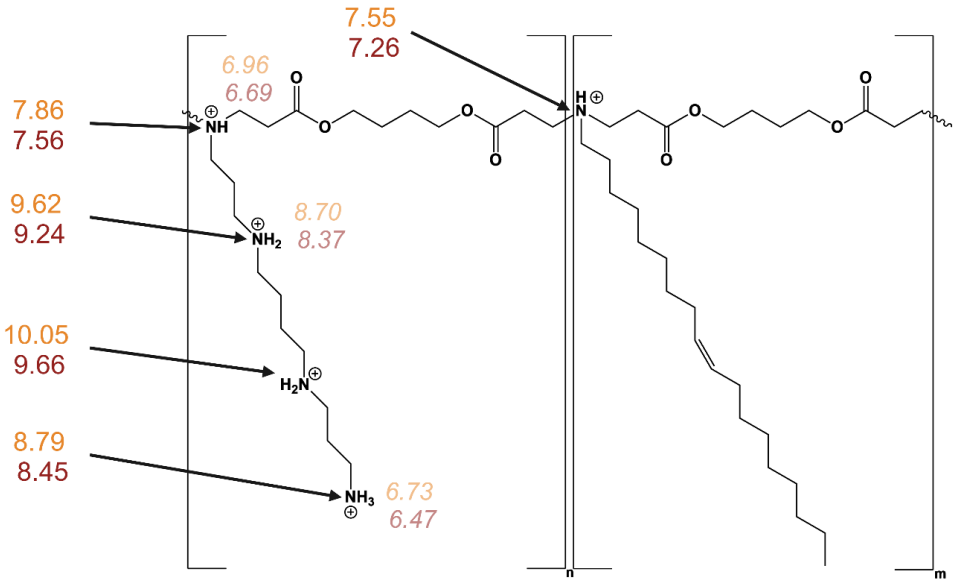

Figure III.S2. p*K*a values of the polymer at 25 °C (orange) and 37 °C (red). p*K*a values after protonation of the secondary amine with p*K*a 10.05 (*i.e.*, the most alkaline) are shown in italics.

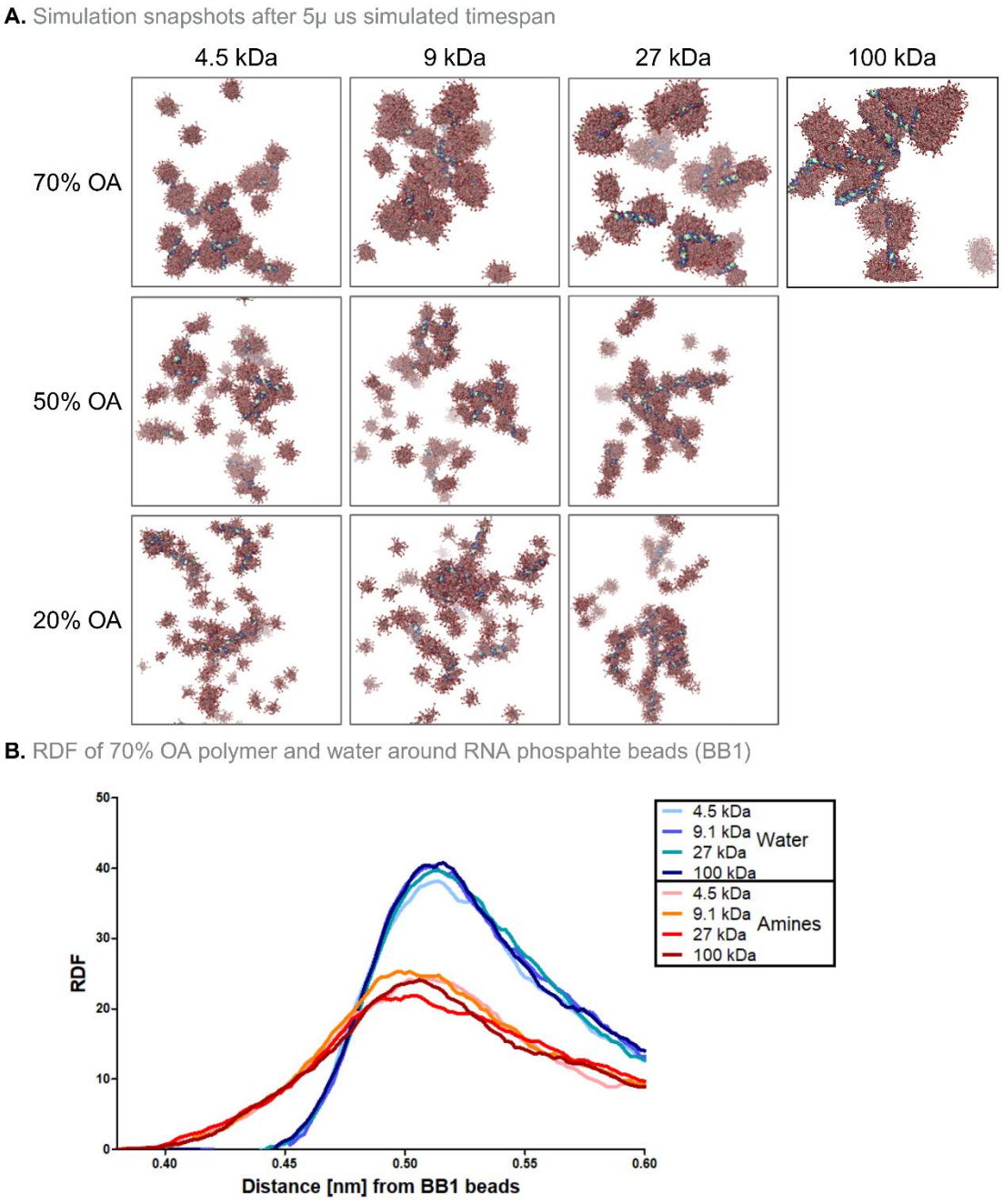

Figure III.S3. Variation of molecular weight of the polymer. A. Visual output after 5 μs simulated particle assembly **B.** Radial distribution function (RDF) around RNA phosphate beads (BB1) for 70% OA PBAE at varied MW of the polymer. Red: Amine beads, Blue: Water beads.

A. Determination of CMC for 70%OA PBAE by Pyrene Assay

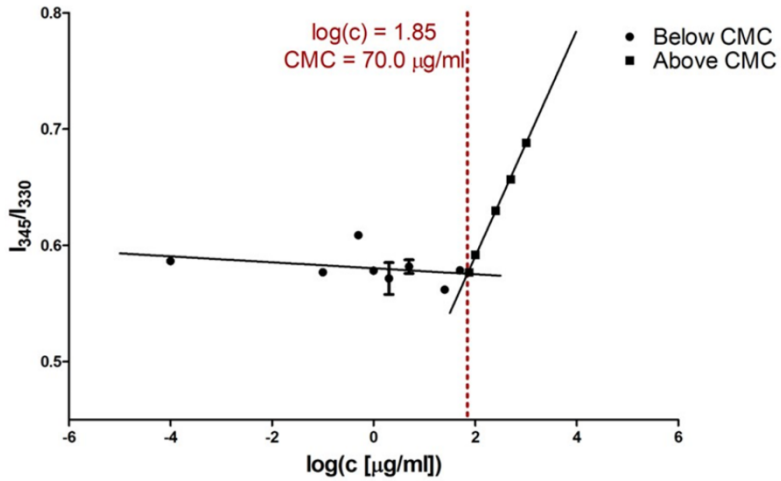

B. Summary of CMCs depending on %OA

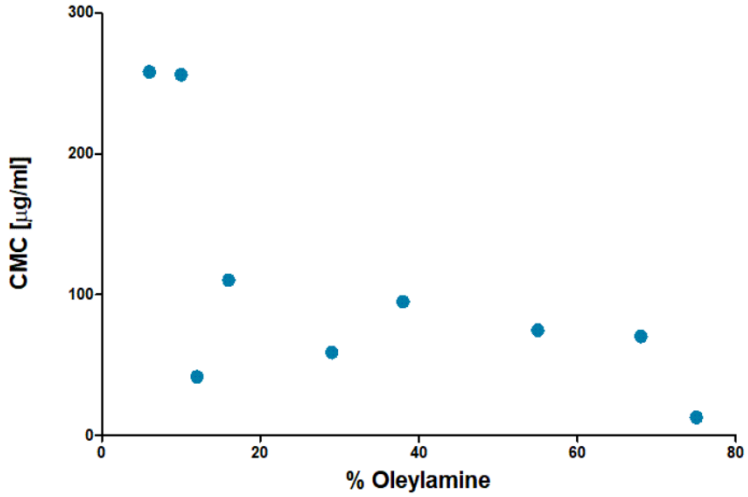

Figure III.S4. CMCs determined by pyrene assay. A. Calculation of the CMC for a 70% OA polymer **B.** Overview of CMCs depending on %OA.

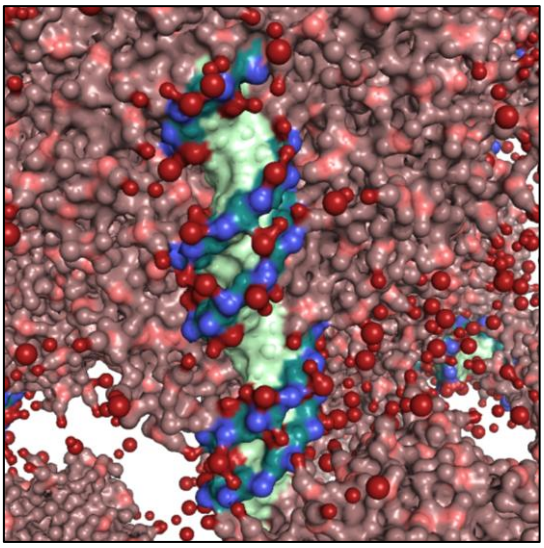

Figure III.S5. Closeup simulation snapshot, visualizing the interaction between siRNA (phosphates blue/ ribose petrol/ bases mint) and spermines (red).

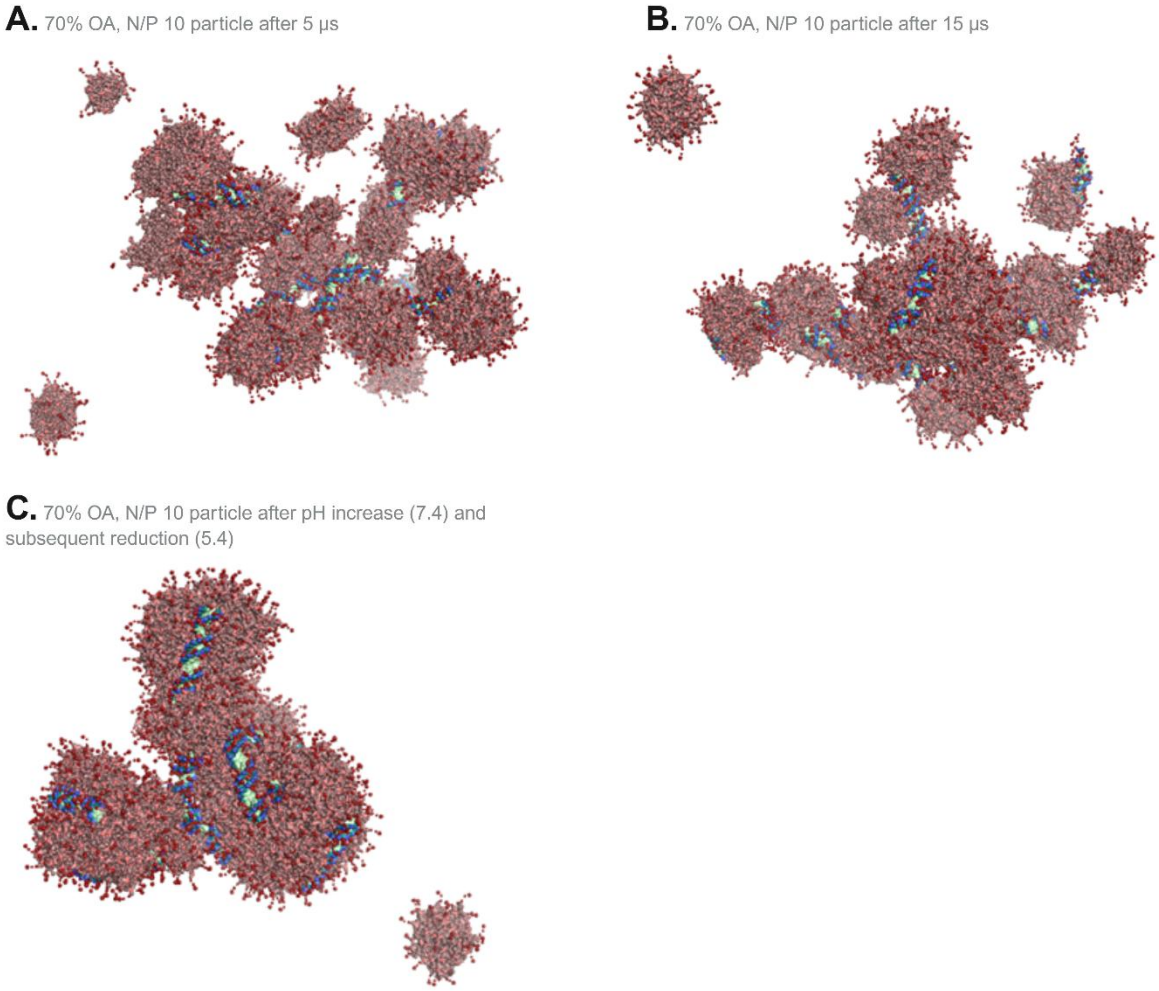

Figure III.S6. 70%OA, N/P 10 particle at different time points. A. After 5 µs at pH 5.4 **B.** the same particle after 15 µs simulation at pH 5.4 **C.** The same particle after pH increase to pH 7.4 and subsequent reduction to pH 5.4.

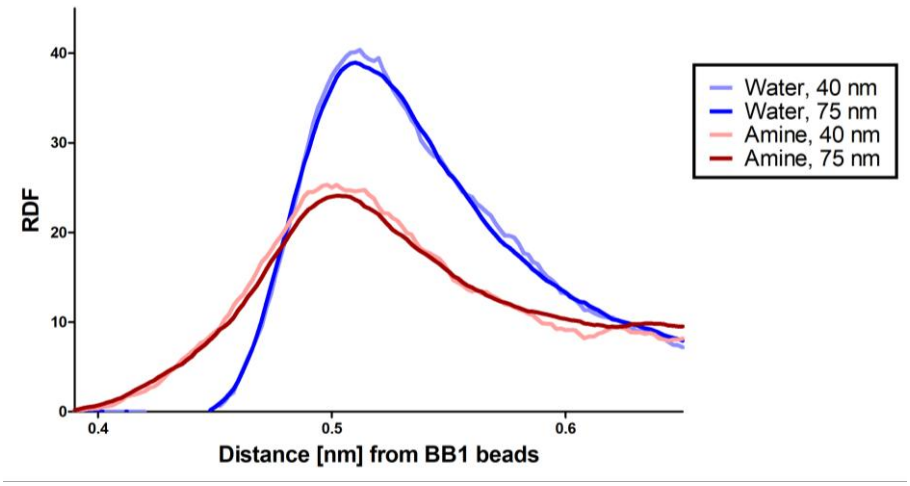

Figure III.S7. Comparison of simulation in increased box size (75 nm) to the standard setup (40 nm) via RDF: Amines (red) and water (blue) around phosphate beads (BB1).

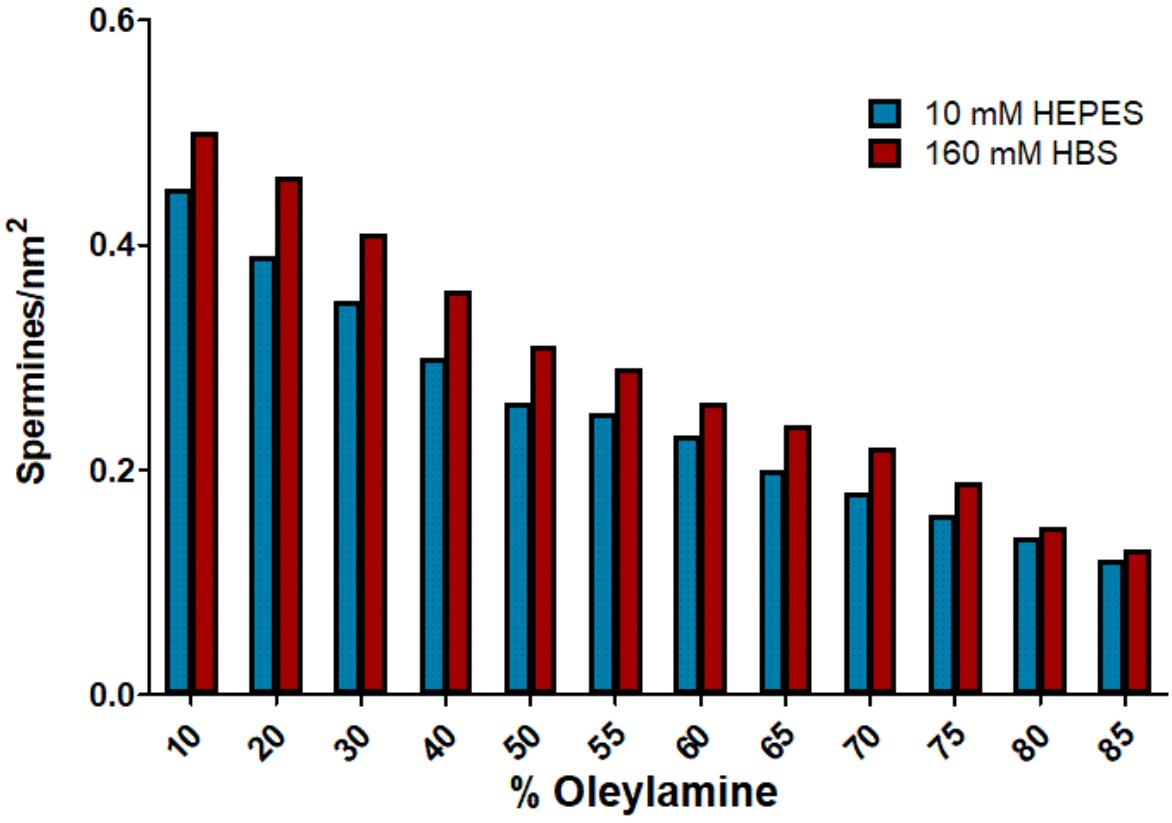

Figure III.S8. Spermine density on the solvent accessible surface area (SASA) of the micelle cores, consisting of backbone and OA beads. Calculated after simulation of polymer only for 2.5 µs in 10 mM HEPES (blue) or 160 mM HBS (red).

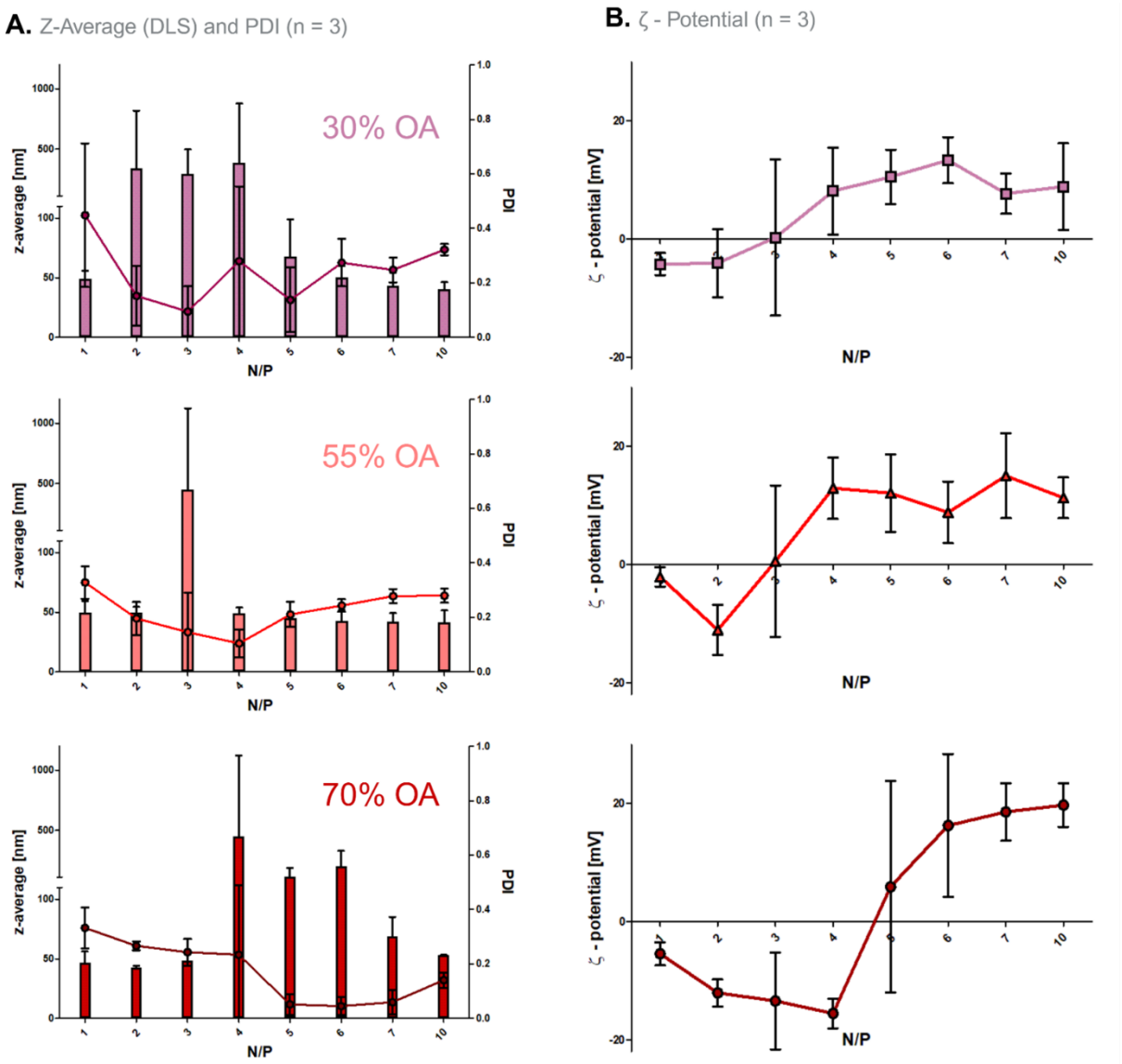

Figure III.S9. Particle characterization at increasing N/P ratios for 30%, 55% and 70% OA PBAE with siGFP. A. z-average (bars) and PDI (dots) of particles as function of N/P ratio, mean ± sd, n = 3. **B.** ζ-Potential as function of N/P ratio, mean ± sd, n = 3.

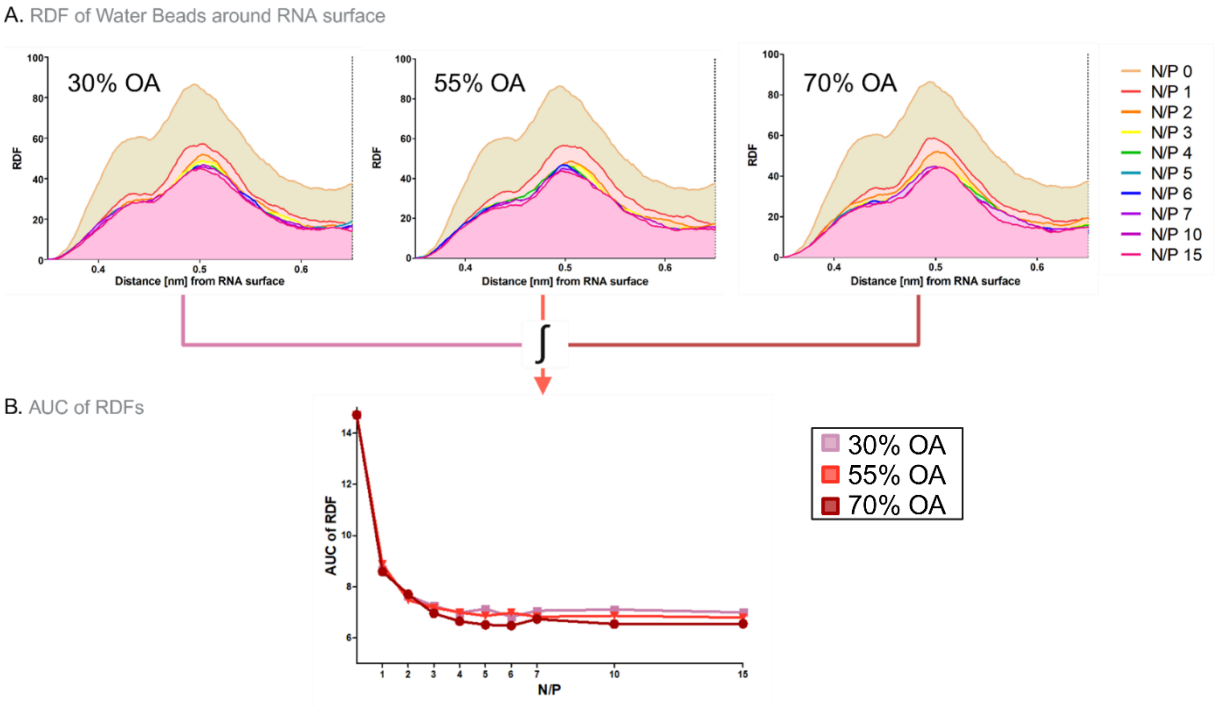

Figure III.S10. Calculation of encapsulation efficiency from MD output via the area under the curve (AUC) of radial distribution functions (RDF). A. Radial distribution functions of water around the surface of the RNA model for 30%, 55% and 70% OA at N/P ratios from 0 (RNA only) to 15. **B.** Graph resulting from integration of RDF curves of (A) between 0 nm and 0.65 nm distance, yielding the AUC for each N/P ratio.

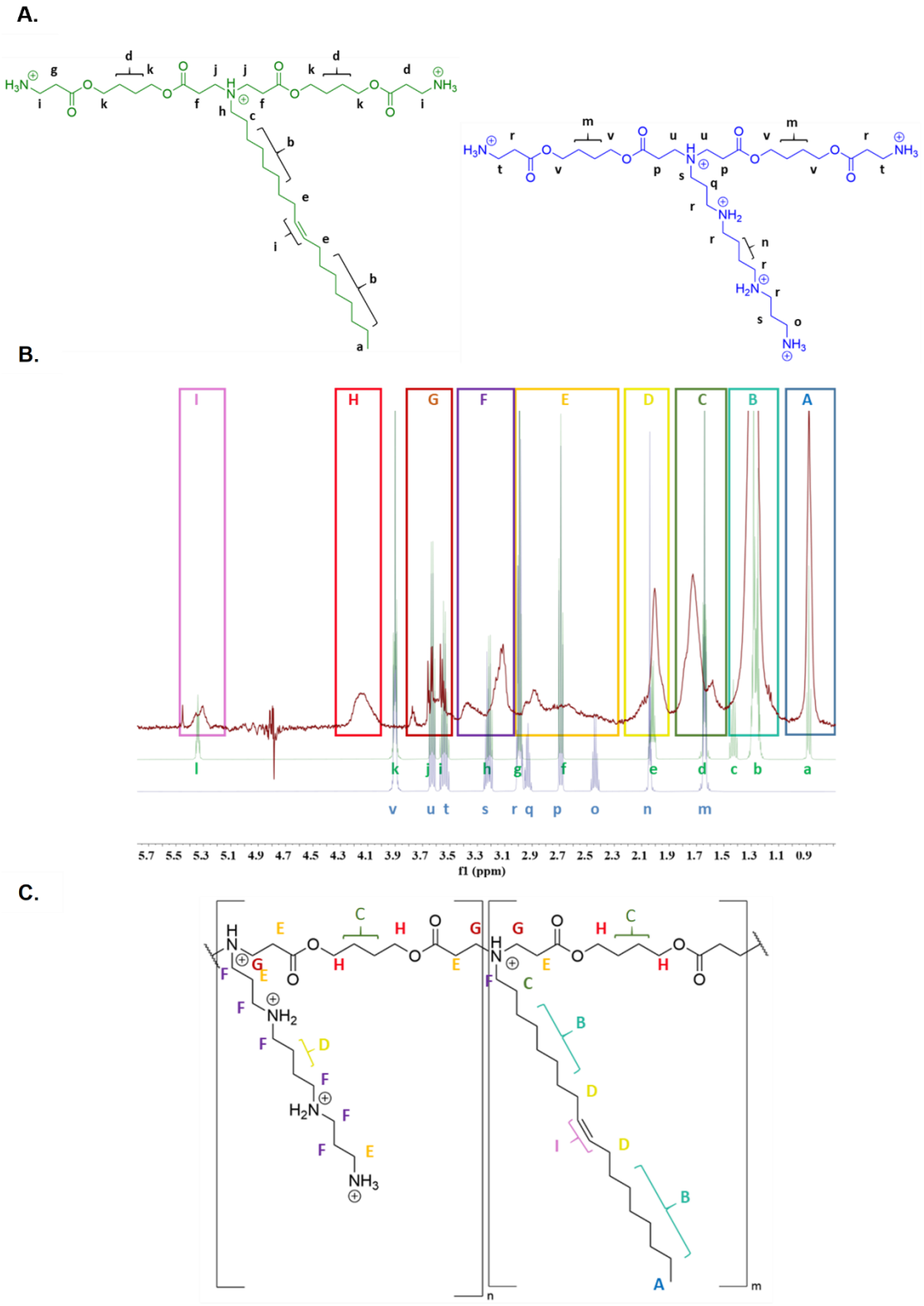

Figure III.S11. Proton assignment to ^{1}H NMR signals of PBAE. A. Artificial fragments of the oleylamine part (green) and the spermine part (blue) of the PBAE polymer for input into the ^{1}H NMR spectra prediction tool of *MestReNova*. **B.** Overlay of the predicted spectra (oleylamine spectrum with signal assignment in green; spermine spectrum with signal assignment in blue; fragment signal assignment in lower case) and the real ^{1}H NMR spectrum of PBAE (70% OA) with resulting region assignment (in upper case) of the polymer-PBAE structure in **C.**

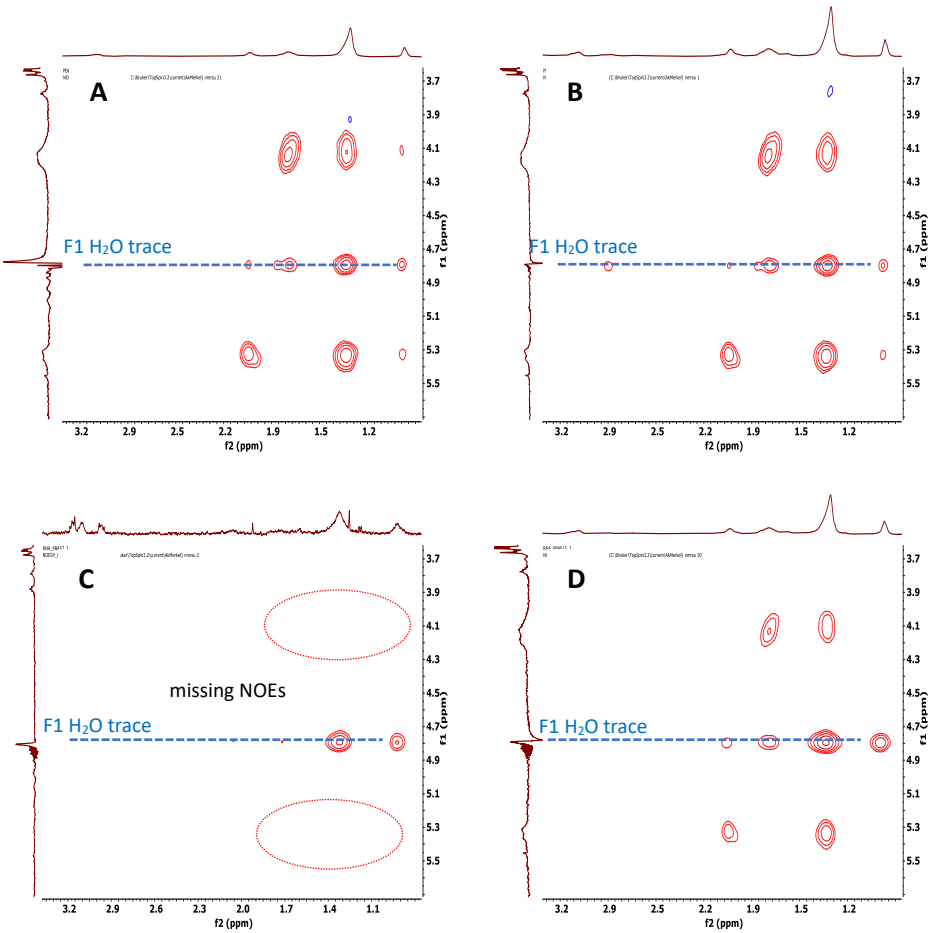

Figure III.S12. Excerpts of 2D NOESY spectra with identical amplifications of A. PBAE alone; concentration as in C. **B.** PBAE alone; concentration as in D. **C.** N/P 7. The dashed oval circles indicate the region where previous NOE correlations are now missing. **D.** N/P 15.

Table III.S1. Summary of results from titration ^{1}H NMR method. Effective N/P ratios were calculated according to eq. 3, based on the regressions shown in Figure III.S3B.

	theoretical N/P	effective N/P				
		n1	n2	n3	mean	SD
30% OA. 10 mM PBS	1	1.15				
	2	2.08				
	3	3.27				
	4	3.98				
	5	4.64	4.92	5.08	4.88	0.22
	6	4.08				
	7	5.31	6.36	6.32	6.00	0.59
	10	4.23	7.20	7.24	6.22	1.73
70% OA. 10 mM PBS	1	0.93				
	2	1.89				
	3	2.81				
	4	3.73				
	5	4.77				
	6	5.85				
	7	6.88	6.82	6.61	6.77	0.14
	8	7.81				
	9	8.60				
	10	9.28	8.34	6.62	8.08	1.35
	15	10.61	6.83	6.98	8.14	2.14
70% OA. 150 mM PBS	1.7	1.55				
	3.3	3.03				
	5	4.82				
	7	6.82	6.85	6.93	6.86	0.05
	8.3	8.01				
	11.6	9.37				
	10	8.92	8.66	8.74	8.77	0.13
	13.3	9.68				
	15	9.97	10.67	10.80	10.48	0.45

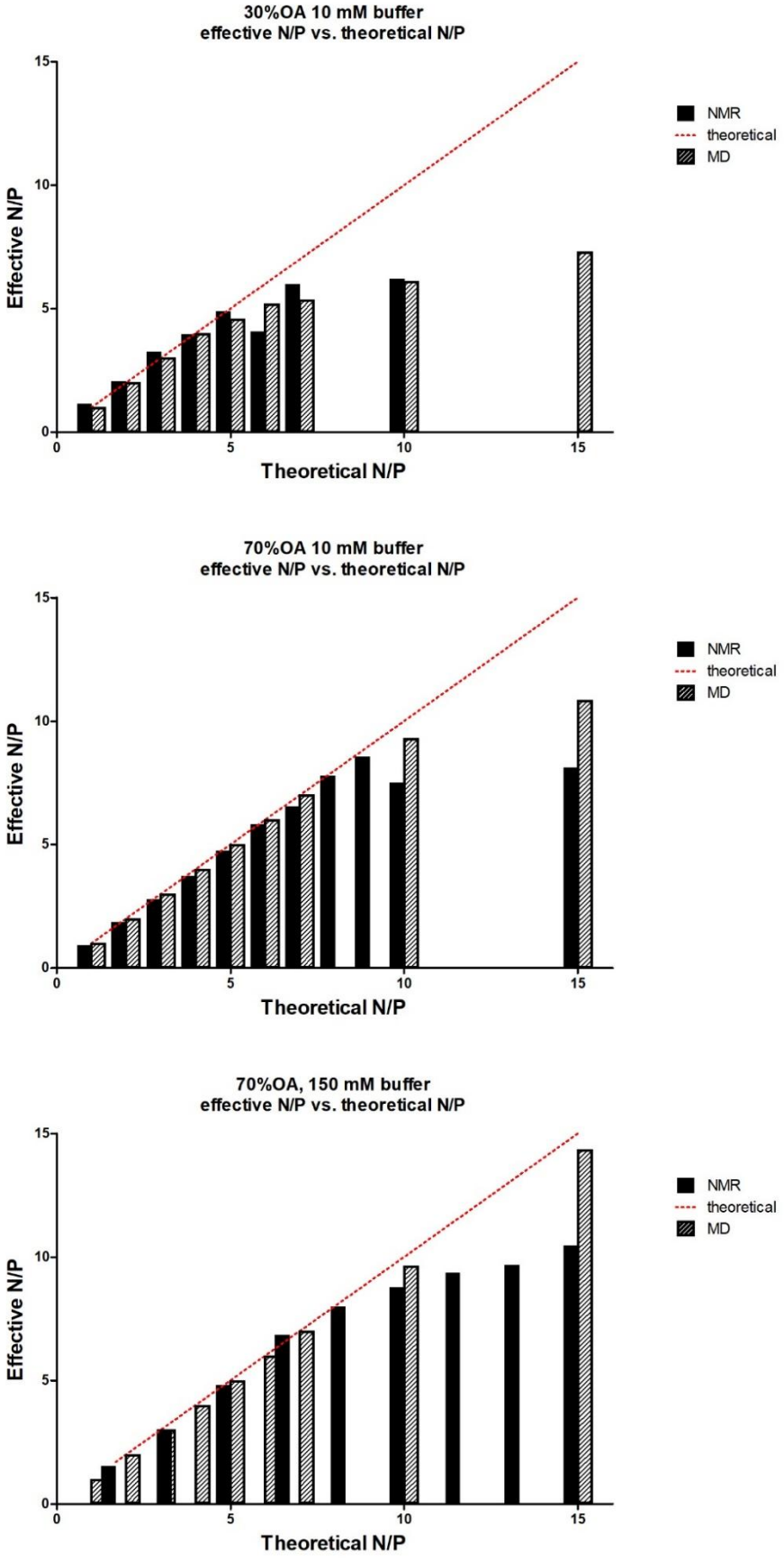

Figure III.S13. Effective vs. theoretical N/P ratio in NMR (titration) vs. MD, n = 1.

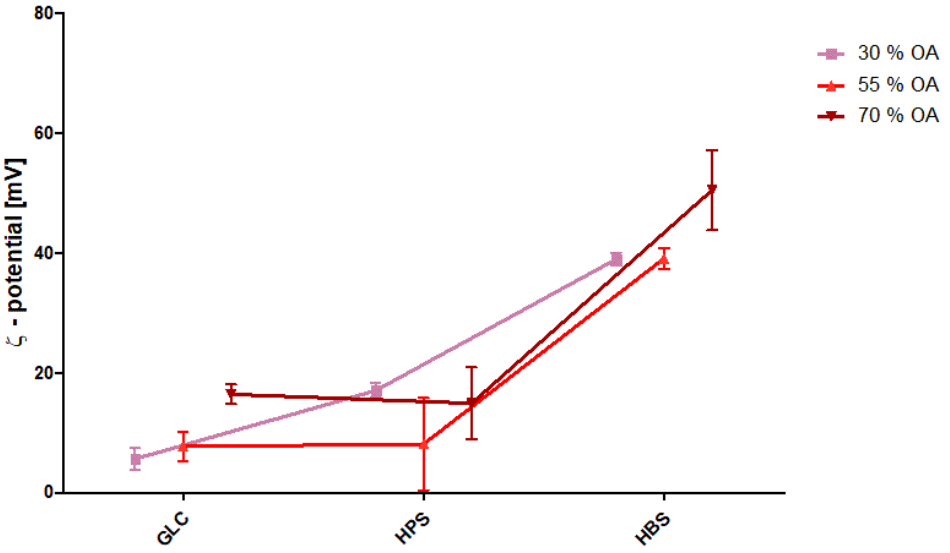

Figure III.S14. ζ-Potential of N/P = 10 particles in 5% Glucose, 10 mM HEPES and 160 mM HBS, n = 3, mean ± sd.

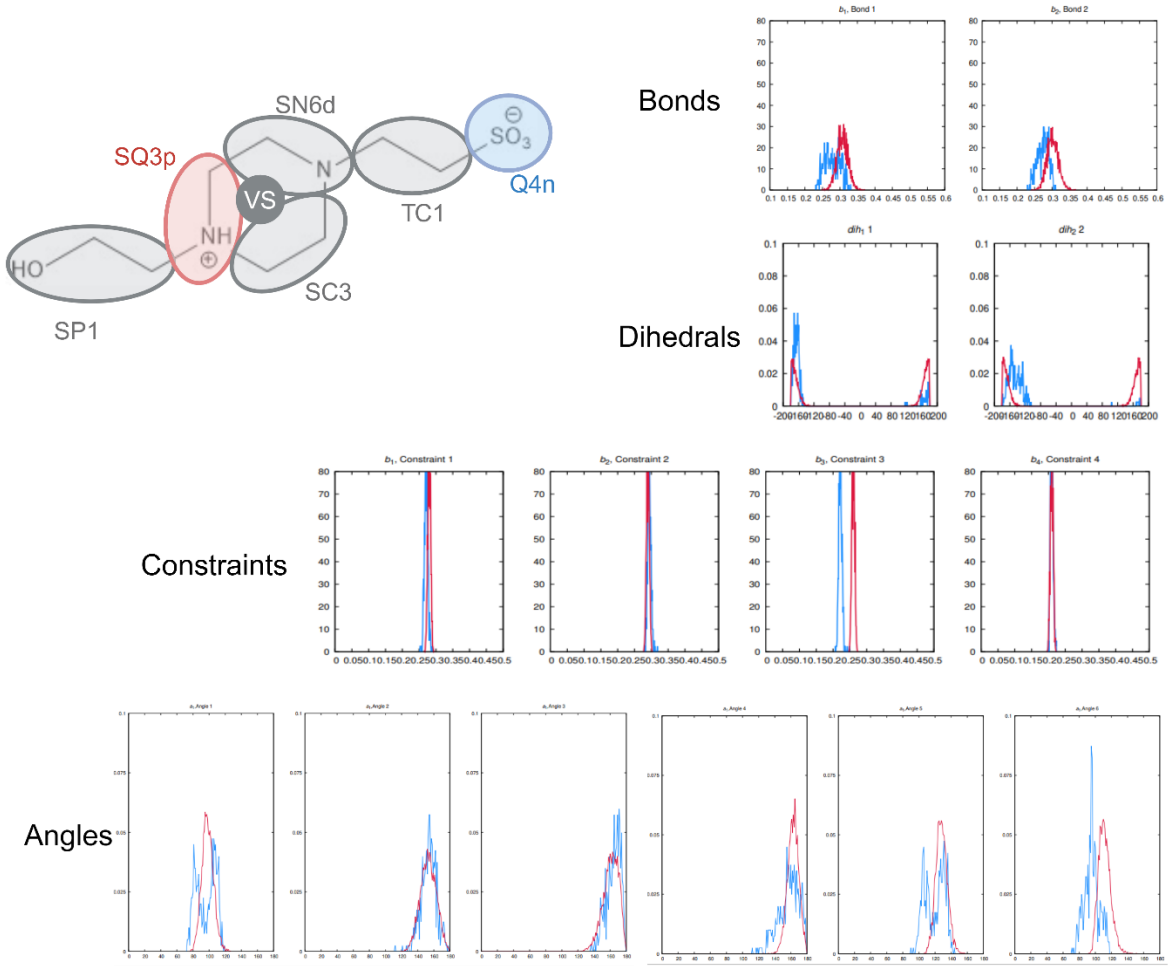

Figure III.S15. Mapping and parametrization of the HEPES model used as buffer substance within MD simulations of the project. Bonded distributions of the CG model (red) are shown in comparison to the All-Atom (AA) model (blue).

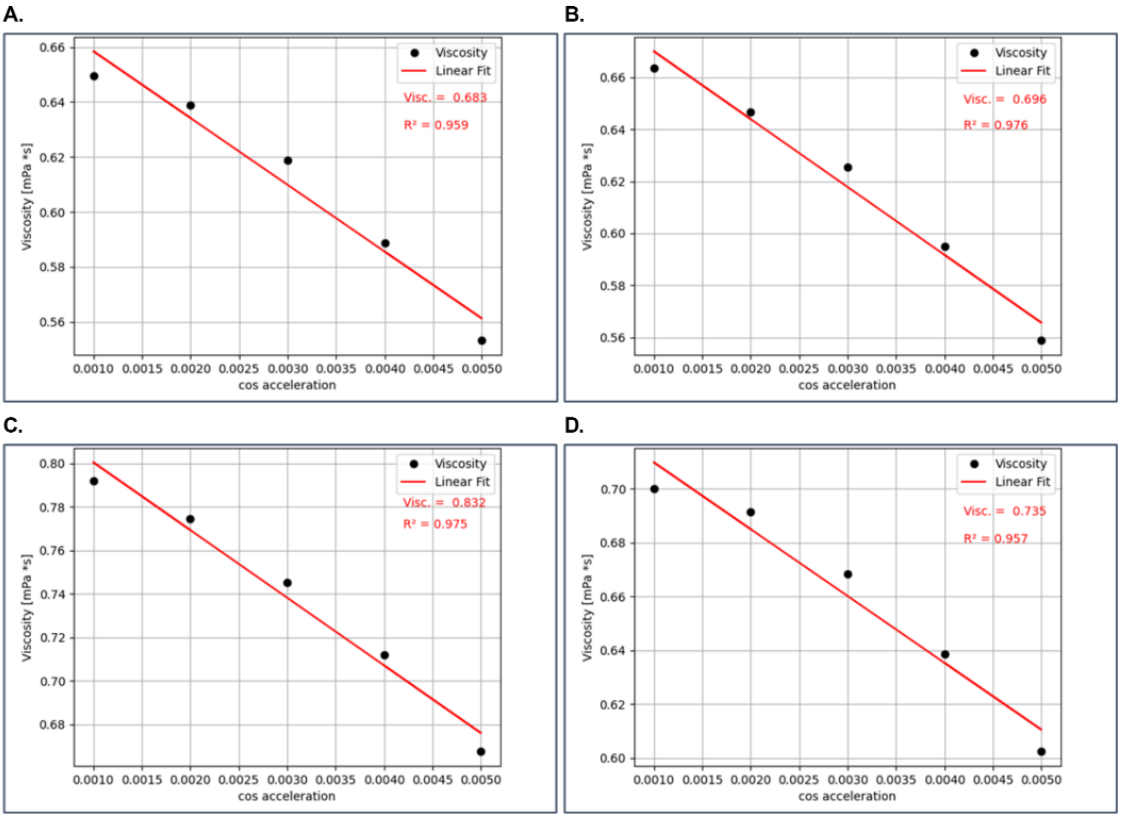

Figure III.S16. Shear viscosity of simulated buffers/solvents as determined by the periodic perturbation method. **A.** Water **B.** 10 mM HEPES **C.** 5% Glucose **D.** 160 mM HBS.

Table III.S2. Shear viscosity of simulated buffers/solvents as determined by the periodic perturbation method.

Buffer/Solvent	Shear Viscosity [mPa*s]
Water	0.683
10 mM HEPES	0.696
5% Glucose	0.832
160 mM HBS	0.735

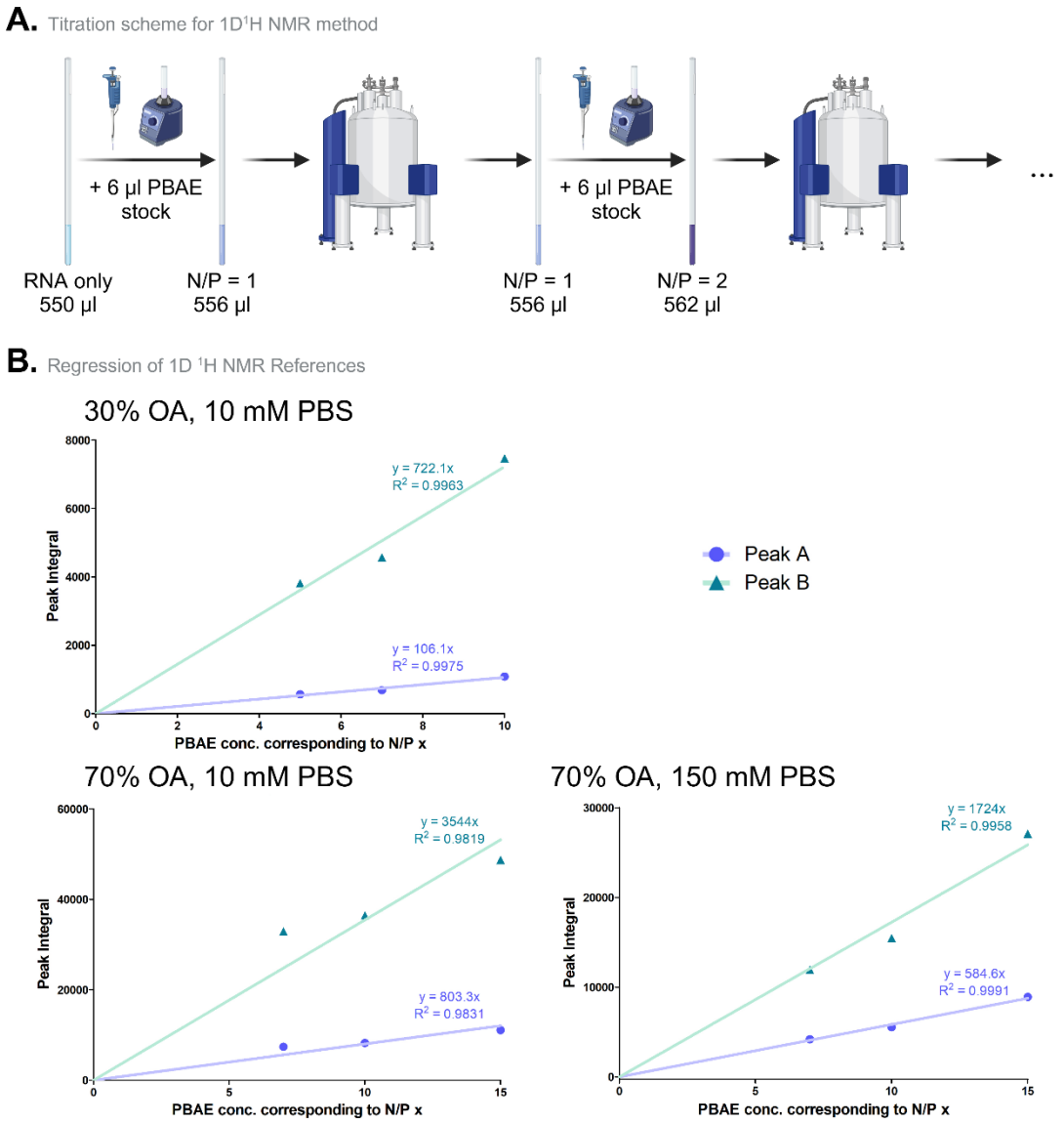

Figure III.S17. 1D ^{1}H NMR method. A. Titration setup for the 1D ^{1}H NMR experiment used to determine effective N/P ratios. **B.** Linear regressions for the calculations of effective N/P ratios from NMR. PBAE only measured at concentrations corresponding to N/P 0 to 15. Each data point was assessed with n = 2.

Chapter IV - Proton sponge or membrane fusion? – Endosomal escape of siRNA polyplexes illuminated by molecular dynamics simulations

Katharina M. Steinegger[a], Min Jiang[a], Fabian Link[a], Benjamin Winkeljann[a,b,c], Olivia M. Merkel*[,a,b,c]

[a] Ludwig-Maximilians-University Munich, Department of Pharmacy, 81377 Munich, Germany

[b] Center for NanoScience (CeNS), Ludwig-Maximilians-University Munich, 80799 Munich, Germany

[c] Comprehensive Pneumology Center Munich (CPC-M), Helmholtz Munich, German Center for Lung Research (DZL), 81377 Munich, Germany

The following chapter was submitted to *Advanced Materials* on 22 September 2025 **Katharina M. Steinegger,** Min Jiang, Fabian Link, Benjamin Winkeljann, Olivia M. Merkel*: "Proton sponge or membrane fusion? – Endosomal escape of siRNA polyplexes illuminated by molecular dynamics simulations"

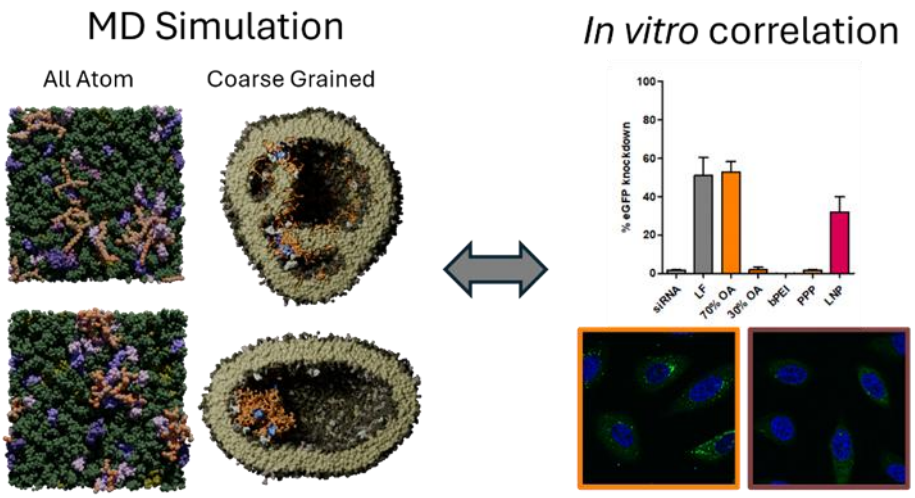

1 Abstract

To achieve a therapeutic effect, nanoparticles delivering nucleic acids must facilitate endosomal escape (EE) of their cargo. Despite extensive research, the mechanisms that lead to an effective EE are not sufficiently understood. Herein, we utilized Molecular Dynamics (MD) simulations in All Atom (AA) and Coarse Grained (CG) resolutions to differentiate the interaction of four polymeric formulations (polyplexes) and one lipid nanoparticle (LNP) with endosomal membranes. On the one hand, the results emphasize the benefit of hydrophobic residues in the nanoparticles. On the other hand, the role of anionic lipids in the biological membranes is demonstrated. Furthermore, the identified interaction patterns were successfully correlated to the *in vitro* performance of the formulations. For the first time, different EE mechanisms of polyplex formulations are visualized in simulation and therefore distinguishable from one another. Hence, this work highlights the power of MD simulations for taking a big step towards better understanding EE efficiency.

2 Introduction

Short interfering ribonucleic acid (siRNA) downregulates the expression of targeted, disease-driving genes[3] by binding to the RNA-induced Silencing Complex (RISC) in the cytoplasm. Therefore, following endocytosis, escape from the endo-lysosomal pathway is essential to achieve a therapeutic effect[200]. A broad range of strategies has been developed to formulate potent nanoparticles for nucleic acid delivery[201, 202], including the use of polycationic polymers[151, 203]. However, many of these polymer-based polyelectrolyte complexes, commonly termed polyplexes, exhibit limited endosomal escape (EE)[136, 204], leaving room for significant technological improvement[45, 157].

Various mechanisms have been discussed to play a role in the EE of polymeric nanoparticles: Initially, the “proton sponge” theory, first formulated in the 1990s[36], was among the most popular theories. It relies on the buffering capacity of endocytosed polymers, which promotes increased proton influx into the endosome during acidification. This is thought to be accompanied by the influx of neutralizing chloride ions and water[67], resulting in osmotic swelling. Ultimately, the endosome ruptures and nucleic acid cargos could be released into the cytoplasm. A closely related hypothesis proposes that endosomal acidification increases the charge density of the polymer, leading to polyplex swelling and inducing a steric burst of the endosomal membrane[48]. These hypotheses are supported by findings that polymers with pKa values in the physiological range (approximately 6-8) are more effective at facilitating

EE[205] and the circumstance that EE can be reduced by inhibiting endosomal acidification. However, conflicting results from live-cell imaging demand a revision of the proposed mechanisms[206], as the data does not indicate complete lysis of endosomes after successful EE of the nucleic acid. In either case, rapid and intense disruption of endosomes and lysosomes can induce cytotoxicity due to the concurrent release of harmful vesicular contents, and is therefore considered undesirable[207]. Subsequently, attention shifts to direct polymer-membrane interactions that locally form smaller endosomal holes or pores[208, 209]. Polyplexes do not escape the endosomes intact[206], but rather in a disintegrated state. The role of acidification could therefore be attributed to its involvement in nucleic acid cargo unpacking and polymer shedding from the particle[179].

Concerning lipid-based nanoparticles (lipoplexes and lipid nanoparticles (LNPs)), research indicates EE to be a complex procedure including membrane fusion, phase transition in the lipid phase of the LNP, and lipid mixing between membrane and nanoparticle [30, 66, 71, 206, 210].

In consequence, the lipid bilayer of the membrane is disturbed and the cargo escapes through resulting holes. LNPs can be highly effective and have successfully entered the market, for example in the form of Onpattro® (Patisiran)[19]. Still, LNPs too are limited by their EE, and only a small, often cited as single-digit percentage[211] of the encapsulated siRNA molecules reaches the cytoplasm[212].

Even though great effort has been put into understanding EE mechanisms, the process is still not understood to a level that allows specific fine tuning of EE performance of a formulation.

As Molecular Dynamics (MD) simulations help to understand underlying mechanisms in complex formulations or biological interactions on a molecular level[71, 213], they possess great potential to overcome the gap in understanding EE. All Atom (AA) MD simulations, showing the molecules in single atom resolution, provide detailed insights on e.g., binding mechanisms on a small scale[128, 129]. In contrast, Coarse Grained (CG) MD simulations work with a decreased resolution, as they summarize groups of atoms in predefined beads[97]. CG MD enables larger simulations up to ~ 100 nm side length of the simulation box with longer timescales in the range of multiple microseconds- enabling for example the simulation of the formation of whole nanoparticles[134, 135]. Additionally, it has previously been shown that CG MD can visualize EE mechanisms[71].

This work compares the EE of four polyplexes and one LNP formulation through AA and CG MD simulations. The first polyplex material is 25 kDa branched PEI (bPEI), which is a commercially available polymer that has been used for siRNA delivery in research for over 20 years[35, 36]. The second polymer is a block copolymer consisting of two blocks of 5 kDa bPEI, linked by a 5 kDa polycaprolactone (PCL) chain[214]. Furthermore, two variants of an amphiphilic poly(beta)aminoester (PBAE) copolymer[55, 157] were tested for their EE

performance. They differ in their content of hydrophobic oleylamine (OA) residues, so that a more hydrophilic particle is compared to a more hydrophobic variant. Lastly, an Onpattro®-like LNP formulation[109] was incorporated in the study to directly compare the EE of polyplexes and LNPs.

In vitro experiments outlined strong differences in the performance of the compared formulations. Based on the interaction patterns visualized and identified by MD, these differences can be meaningfully interpreted. Hence, this work highlights the power of MD simulations for taking a big step towards better understanding EE mechanisms.

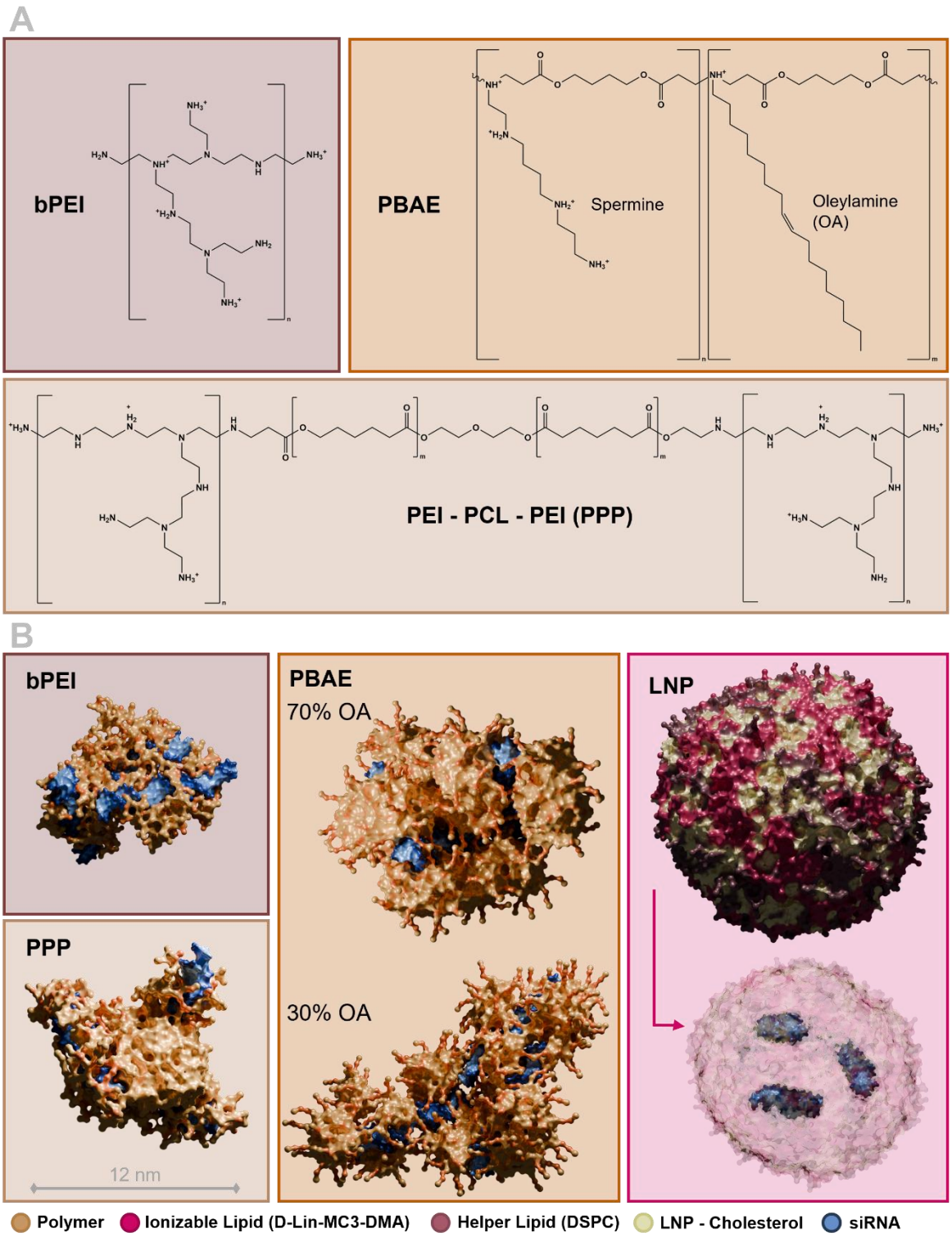

Figure IV.1. Polymer structures and model particles in CG resolution
A. Molecular structures of polymers used in this work; branched polyethylenimine (bPEI), poly(beta)aminoester (PBAE) with varying ratios of hydrophilic spermine and hydrophobic oleylamine (OA), and bPEI – polycaprolactone (PCL) – bPEI block copolymer (PPP). **B.** CG model particles with three siRNA molecules each at pH 7.4. The LNP is additionally shown with transparent lipids to visualize the orientation of the siRNA molecules inside; polymer in gold/orange, MC3/MC3H in pink, DSPC in purple, cholesterol in green, RNA in blue.

3 Results and Discussion

3.1 Characterization of nanoparticles

Four polyplex formulations described in the literature were included in this study and based on the polymers shown in Figure IV.1A. For the PBAE, either a 70% OA polymer (i.e., more hydrophobic) or a 30% OA polymer (i.e., more hydrophilic) were used. All polyplexes were formulated at N/P 10, as all four polymers have been shown to form stable particles at that ratio[35, 54, 157, 214]. The LNP was formulated with an Onpattro®-like composition, but at N/P ratio of 6.5 to align as closely as possible with the simulated model LNP[109]. For all experiments, the formulations were normalized to equal siRNA concentration. However, due to differences in polymer charge density, the total polymer mass concentration varied notably between formulations, despite equivalent N/P ratios. Specifically, relative to bPEI, the concentrations were 7.9-fold higher for 70% OA PBAE, 5.9-fold for 30% OA PBAE, and 1.6-fold for PPP.

All five formulations formed particles with a hydrodynamic diameter (z-average) between 50 and 70 nm and a polydispersity index (PDI) below 0.3 (Figure IV.S1A). The ζ-potential of all polyplexes was positive, whereas the LNPs were slightly negatively charged (Figure IV.S1B). In CG simulations, polyplexes were formed via self-assembly, resulting in stable nanoparticles with diameters ranging from approximately 10 to 18 nm (Figure IV.1B). All polymer molecules present were associated with the respective polyplex, except for 30% OA PBAE. Here, 20% of the polymer remained separate from the polyplex at both pH 5.4 and pH 7.4, resulting in a final N/P ratio of approximately eight. This agrees with our previous work on PBAE polyplexes, where 30% OA PBAE showed unbound polymer at pH 5.4 and N/P ratios above ~ 6[134]. For subsequent simulations of the membrane interaction, excess polymer in the 30% OA PBAE MD setup was removed. The model LNP with a diameter of ~ 16 nm did not originate from a self assembly simulation, but was constructed based on a protocol for the setup of LNPs with hexagonal core structure in Martini 3[109]. As Polyethylenglycol (PEG) lipids tend to shed from LNPs when in contact with serum[215] they are not expected to play a role in EE of LNPs. Therefore, no PEG lipids were incorporated into the simulated LNP model.

3.2 Comparison of the particles in vitro

In HeLa cells stably expressing enhanced green fluorescent protein (eGFP), the 70% OA PBAE polyplex and the LNP showed the highest knockdown efficiencies with 30 - 60% at a dose of 20 pmol/ 6,000 cells. (Figure IV.2A), whereas the other polyplex formulations achieved no knockdown at the same dose. No cytotoxicity was evident for the 30% OA PBAE and the LNP formulation, with cell viability being > 90% and lactate dehydrogenase (LDH) release

being < 10% (Figure IV.S3) at all tested particle concentrations. The bPEI and PPP particles only caused mild cytotoxicity (< 90% cell viability) at the highest concentration. However, the 70% OA PBAE polyplexes caused notable LDH release (12-25%) and reduced cell viability (50-80%) at all tested concentrations.

The limited knockdown efficiencies observed for the 30% OA PBAE, bPEI, and PPP polyplexes can be partially attributed to insufficient cellular uptake (Figure IV.2B and Figure IV.S4). Among all formulations, the 70% OA PBAE polyplex consistently showed superior uptake, while 30% OA PBAE exhibited particularly low internalization, and bPEI and PPP polyplexes performed comparably to each other. The relatively weak uptake signal of the LNP in confocal microscopy was likely due to fluorescence quenching within the dense core of the nanoparticles[216]. Since the microscope settings were optimized to detect the strong fluorescence signal of AF647-labeled siRNA in polyplexes, they were suboptimal for capturing the quenched signal from the LNPs. Consequently, Figure IV.S4 indicates that cellular uptake of the LNPs is comparable to that of bPEI and PPP. Differences in uptake may explain the superior knockdown efficiency of the 70% OA PBAE. However, they do not fully account for the performance gap between the LNP and the bPEI or PPP polyplexes. Subsequently, EE efficiency was quantified through confocal fluorescence microscopy as puncta caused by the recruitment of mRuby-3-Galectin 8 fusion protein (Gal8) stably expressed by the cells. Gal8 is recruited to damaged endosomes when luminal glycans are exposed to the cytoplasm (Figure IV.2C+D) and is therefore widely used as EE marker[217]. The 70% OA PBAE polyplexes caused significantly more Gal8 recruitment compared to all other formulations. However, these polyplexes also achieved the highest uptake by the HeLa cells. Therefore, the high knockdown efficiency of the 70% OA PBAE was likely a combination of superior uptake and strong EE. The endo-lysosomal membrane disruption caused by the EE of the 70% OA polyplexes can trigger apoptosis or uncontrolled cell death[218, 219], consistent with the observed cytotoxicity of 70% OA PBAE. HeLa cells are characterized by relatively small endosomes, which has been suggested to favor the EE efficiency of polyplex formulations[204]. Hence, because Gal8 recruitment is cell type-dependent[53], the same polymer may be safe and effective in other cell types[54]. The other polyplexes induced significantly lower Gal8 recruitment, suggesting that limited EE may contribute to their poor knockdown efficiency, which is in accordance with published results about PEI polyplexes[53].

Due to the lack of cellular uptake of 30% OA PBAE, their performance in the Gal8 assay could not be directly compared to the other formulations. Rui et al.[53] reported a negative correlation between the hydrophobicity of PBAE polyplexes and Gal8 recruitment. Notably, in their study, increased Gal8 recruitment did not translate into improved transfection efficiency. The authors suggested that high Gal8 puncta counts might result from empty polymer micelles that disrupt endosomes without delivering nucleic acid cargo. For other amphiphilic PBAEs, a positive

correlation between hydrophobicity and Gal8 recruitment was observed[220], with the most hydrophilic polymer causing the least Gal8 puncta.

Interestingly, the LNP formulation caused Gal8 recruitment as low as bPEI and PPP, even though its knockdown efficiency was higher. However, the low Gal8 recruitment by the LNPs likely originated from the EE mechanism itself: It has been shown that the ionizable lipid DLin-MC3-DMG does not induce Galectin recruitment[30], arguably due to the formation of only small pores in the endosomal membrane. In summary, although useful within narrowly defined particle libraries[136], Gal8 recruitment alone is not sufficient to predict the EE or knockdown efficiency across diverse nanoparticle formulations. The detection of Gal8 puncta does not indicate whether endosomal damage was accompanied by the release of nucleic acid cargo[53], nor does it capture smaller membrane defects[30]. This could lead to favoring potentially cytotoxic particles with high Gal8 recruitment over similarly effective particles that cause only minor endosomal damage through other EE mechanisms. To further analyze the interaction of the nanoparticles with cellular membranes, their capacity to induce erythrocyte lysis was tested (Figure IV.2E). The LNPs, 30% OA PBAE and bPEI polyplexes only caused minor hemolysis, independent of the medium's pH level. In contrast, PPP particles caused notable hemolysis of ~ 10 – 25% at all pH levels, and 70% OA PBAE polyplexes caused increased lysis at pH 5.4 only. Hemolytic activity is generally associated with cytotoxicity[221]. However, lytic activity at acidic pH only, as demonstrated by 70% OA PBAE, is favorable for polyplexes[136], as it indicates increased membrane interaction in the acidified endo-lysosomal compartment. Again, this emphasizes that the toxicity of the 70% OA PBAE can be referred to its excessive effect on the endosomes.

As the uptake efficiency of the polyplexes differed strongly, it was not possible to fully distinguish the EE efficiency from the above presented results. However, the 70% OA PBAE and the LNP overall outperform the other formulations concerning knockdown efficiency, which will be correlated to their membrane interactions and EE mechanisms by MD below. Therefore, nanoparticles-membrane interactions were next assessed by measuring erythrocyte lysis (Figure IV.2E). The LNPs, 30% OA PBAE and bPEI polyplexes only caused minor hemolysis, independent of the medium's pH level. In contrast, PPP particles caused notable hemolysis of ~ 10 – 25% at all pH levels, and 70% OA PBAE polyplexes caused increased lysis at pH 5.4 only. Hemolytic activity is generally associated with cytotoxicity[221]. However, lytic activity at acidic pH only, as demonstrated by 70% OA PBAE, is favorable for polyplexes[136], as it indicates increased membrane interaction in the acidified endo-lysosomal compartment. Again, this emphasizes that the toxicity of the 70% OA PBAE can be referred to its excessive effect on the endosomes. As the lytic activity of the PPP polymer exceeds the cytotoxicity observed in other assays (Figure IV.S3), it can be related to membrane interactions in the

hemolysis assay that are otherwise masked by a protein corona around the nanoparticle formed in serum[222].

As the uptake efficiency of the formulations differed strongly, differences in EE performance could not be clearly interpreted. However, the 70% OA PBAE and the LNP formulation overall outperform the other polyplexes concerning knockdown efficiency, which will be correlated to their membrane interactions and EE mechanisms by MD below.

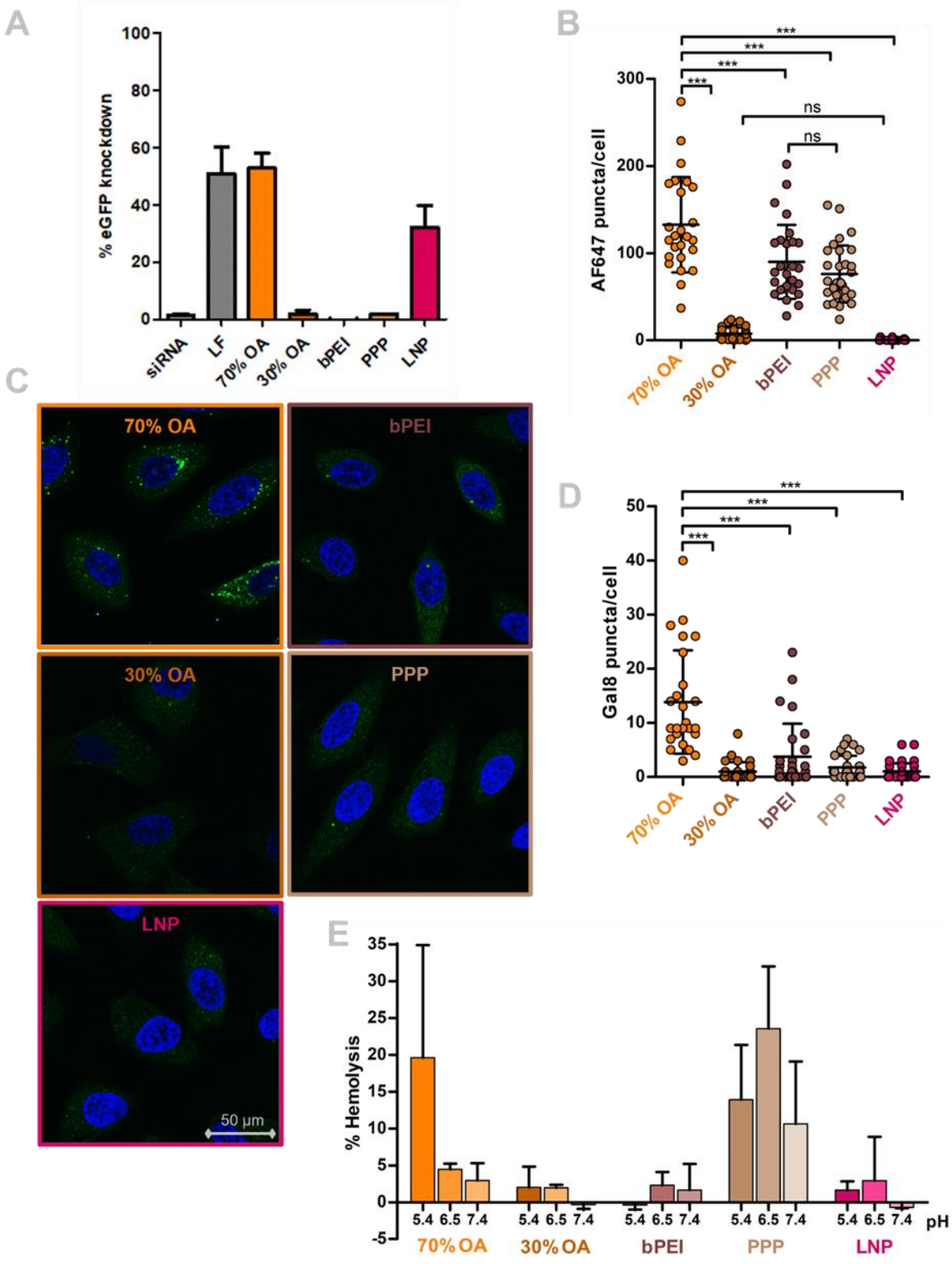

Figure IV.2. Comparison of *in-vitro* behavior

A. eGFP knockdown in HeLa/eGFP cells, mean ± sd, n = 2. **B.** Uptake in HeLa cells quantified as puncta of AF647 labeled siRNA per cell observed in the confocal images, mean ± sd, one-way ANOVA, ***p < 0.001, ns = nonsignificant (p > 0.05). **C.** Confocal images showing Gal8 recruitment (green puncta) in HeLa cells (blue: DAPI) 4 h after transfection. **D.** Quantification of Gal8 puncta as shown in C, mean ± sd, one-way ANOVA, ***p < 0.001, ns = nonsignificant (p > 0.05). **E.** Erythrocyte lysis of all five nanoparticle formulations relative to Triton X treatment at three different pH values (5.4, 6.5 and 7.4), mean ± sd, n = 3.

3.3 Membrane interaction mechanisms in simulation

To identify the interaction mechanisms of nanoparticles with membranes after cellular uptake, AA and CG membranes mimicking different stages of the endo-lysosomal pathway were created (Table IV.S1). The first membrane represents the (early) endosome, which is slightly negatively charged and contains glycolipids that were initially present at the outer leaflet of the plasma membrane[223]. As the milieu in the early endosome is only slightly acidic, the particle interactions with this membrane type were simulated at pH 6.5. Deemed crucial for the functionality of biological membranes is also the formation of microdomains such as lipid rafts[224]. These specified membrane regions form through the preferred interaction of cholesterol, saturated lipids and sphingolipids. To investigate the influence of lipid raft formation on EE, a simplified membrane model, composed of palmitoyloleoylphosphatidylcholine (POPC), cholesterol, and N-Palmitoyl-D-sphingomyelin (DPSM) was created. This model contained an increased amount (2%) of glycolipids (glycolip-monosialotetrahexosylgangliosides DPG1 and DPG3), which comprise one n-acetylneuraminic acid each. Hence, the lipid raft model contained all its negative charge in the glycan layer. Lipid rafts are characterized by reduced lateral diffusion[225] in the ordered state, which was well represented by our models (both AA and CG) in comparison to the other membrane types (Figure IV.S2).

Two additional membrane models were constructed to simulate the late endosome/lysosome with interactions at more acidic conditions (pH 5.4). In the late endosome, the amount of cholesterol and sphingolipids was decreased, whereas the amount of negatively charged lipids was increased[223, 226]. These negatively charged lipids include bis-(monoacylglycero)-phosphate (BMGP)[227], a lipid that is unique to late endosomal/lysosomal membranes. The late endosomal membrane contained the same number of glycolipids as the endosomal membrane used in this study. The lysosomal membrane model was structurally identical to the late endosomal model, except that glycolipids were omitted to allow assessment of their specific influence. As a result, the lysosomal membrane was the only symmetrical bilayer among all models examined. While this study aimed to reproduce the lipid composition of endo-lysosomal membranes with greater compositional diversity than previous models[71, 123], the incorporation of membrane proteins and active cellular processes remains beyond its scope. Consequently, the presented membrane models should still be regarded as simplified representations.

The interaction of the four CG membrane models with all five particle formulations was simulated in triplicates. Initial contact of the particles with the glycosylated leaflet of the membrane was assured by a short pull applied to the particle in the first nanoseconds of simulation. After 2.5 µs, distinctive differences between the particles were detected (Figure IV.3A-E). Two types of interaction with the membranes were prominent: Firstly, hydrophobic

interactions of the PBAEs, the PPP polyplex and the LNP were visible as interference of polymers/LNP-lipids with the hydrophobic core of the membranes. In the case of the PBAEs (Figure IV.3A+B) and the LNP (Figure IV.3C), this led to mixing of membrane lipids and particle material[123], resulting in notable amounts of particle material being shed from the particle and integrated into the membrane. Simultaneously, the 70% OA PBAE polyplex and the LNP were capable of extracting membrane lipids out of the initial membrane plane. Due to the copolymeric structure of the PBAEs, their OA tails reached into the hydrophobic membrane center, while the backbone stayed in the headgroup region and the polycationic spermines reached into the solvent layer above. However, unlike the 70% OA PBAE and the LNP, the 30% OA polymer was not capable of extracting lipids from the membrane into hydrophobic particle compartments above the membrane surface. Hence, the interaction mode of the hydrophilic PBAE appeared more comparable to the influence of bPEI and PPP, which caused only minor to no deviations of the membranes' density profiles (Figure IV.3B, D and E). In the PPP polymer, the hydrophobic compartment of the particle (the PCL chain) is clearly separated from the hydrophilic bPEI units due to the block copolymeric structure. Consequently, if in immediate contact with the membrane, the PCL residue tended to partition into the membrane core, whereas the bPEI segments remained localized at the membrane surface (Figure IV.3E, Figure IV.S5).

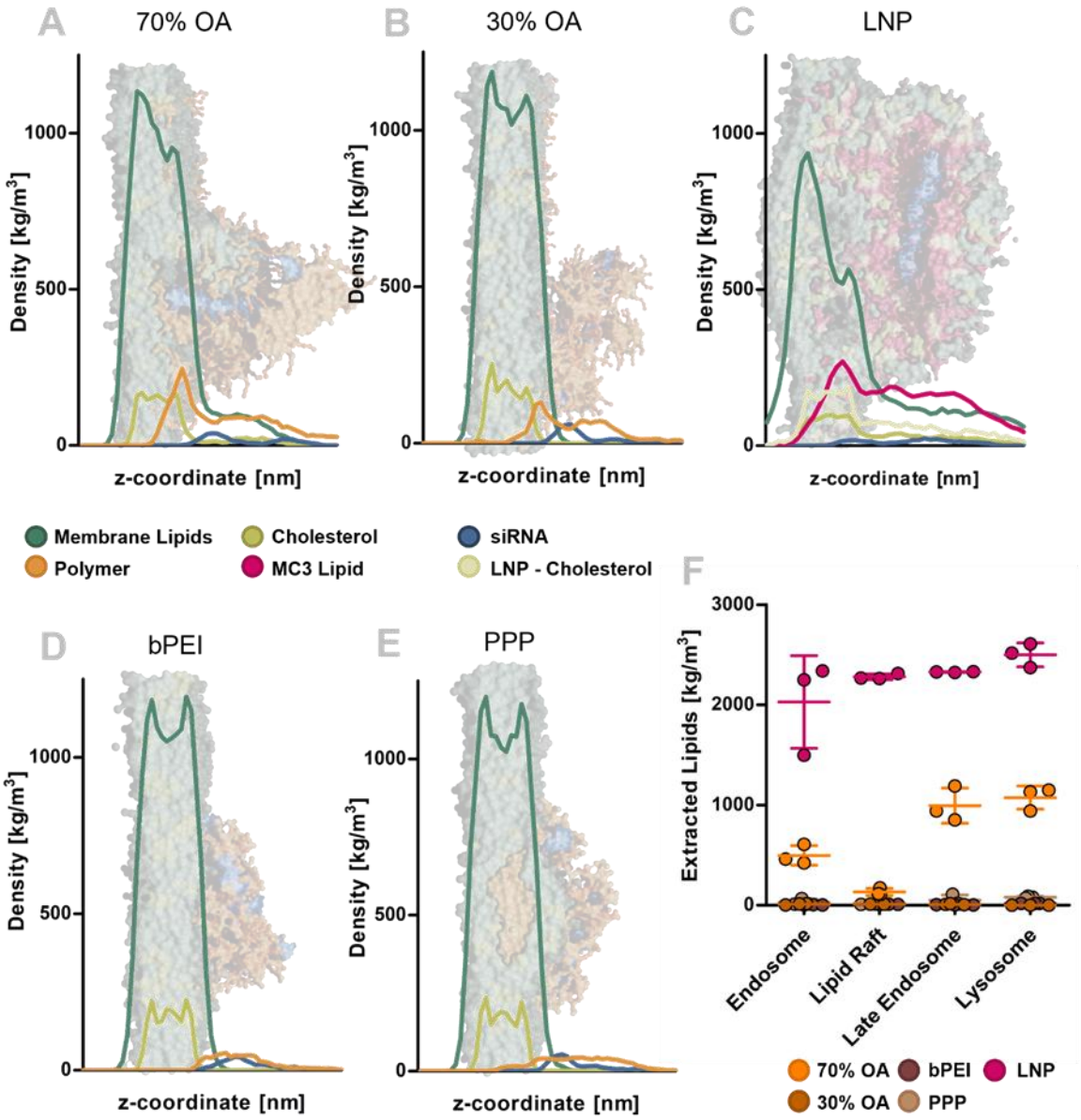

Figure IV.3. CG-MD simulations of nanoparticles interacting with planar membrane models
Density distribution along the z – coordinate of the simulation box after the interaction of a late endosomal membrane with **A.** a 70% OA PBAE particle **B.** a 30% OA PBAE particle **C.** an Onpattro – like LNP **D.** a 25 kDa bPEI polyplex **E.** a PPP polyplex. **F.** Lipids (excluding cholesterol) extracted from the plane of different membranes after interaction with the respective particles, mean ± sd, n = 3.

Based on umbrella sampling simulations, the octanol – water partition coefficients (log P) of the polymers were ranked according to their hydrophobicity: 70% OA PBAE (most hydrophobic) > PPP > 30% OA PBAE > bPEI (least hydrophobic) (Figure IV.4A+B). As discussed above, a direct correlation of polymer hydrophobicity with its EE performance can be seen as controversial. In this case, the most hydrophobic polymer caused the strongest membrane disturbance, but no clear relationship between the other polymers' log P and their effect on endosomal membranes was found.

Secondly, electrostatic interactions were observed for all particles. As the nanoparticles contained an excess of cationic charges, the interaction with negatively charged membrane lipids was favorable. For the 70% OA PBAE, this correlated with the amount of lipids being extracted from the membranes (Figure IV.3F). The least lipids were extracted from the least charged membrane type (lipid raft), and the most extraction took place from the strongly charged late endosome and lysosome membranes. The presence of glycolipids (late endosome vs. lysosome) however did not have a notable influence.

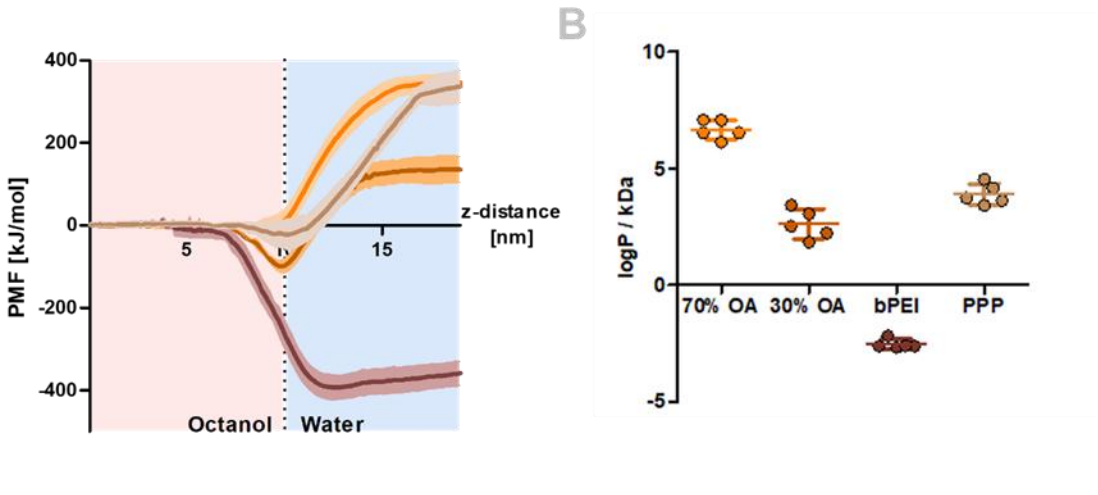

Figure IV.4. Determination of log P values in CG MD.
A. Potential of mean force (PMF) curves of the transfer of a polymer molecule from an octanol phase to a water phase, mean ± sd (n = 5). **B.** log P values of polymers, normalized to molecular weight (per kDa) as calculated from PMF curves in A., mean ± sd (n = 5).

The preferred interaction of all polymers with negatively charged lipids was conclusive both in AA MD (Figure IV.5A+B, Figure IV.S6) and CG MD (Figure IV.5C+D, Figure IV.S6+ IV.S7). In both cases, the anionic lipids (purple shades) clustered around the attached particle or free polymer molecules interacting with the membrane. Figure IV.5 shows the interactions of 70% OA PBAE or bPEI with the late endosomal membrane. In AA resolution, the graphs are noisier due to the lower overall number of molecules in the simulations. Still, it is visible that both polymers (70% OA and bPEI) were transiently attached to the glycolipids, followed by favored contacts to other anionic lipids. This was in general true for all AA setups simulated (Figure S6). The importance of anionic lipids for stable polymer–membrane interactions was particularly evident in simulations involving the lipid raft model. In this system, negative charges were confined to the glycosylated layer extending above the lipid headgroups. As a result, during the transient contacts with glycolipids no negative charges were available in the headgroup region of the membrane, and permanent polymer adsorption did not occur. The role of anionic lipids, especially the lysosome-specific lipid BMGP, has previously been discussed

to be of high relevance for EE of cationic formulations/drugs[228, 229] and was emphasized again by the here presented results. Additionally, the AA simulations confirmed the presence of interactions with neutral lipids and cholesterol for the PBAEs (Figure IV.5B), which clearly distinguished them from the bPEI polymer.

Analysis of the CG simulations (Figure IV.5C+D, Figure IV.S7+8) regarding polymer/MC3 – membrane contacts confirmed good agreement with the AA setups, although glycolipid contacts appeared less transient. In CG simulations, all particles remained associated with the membranes, including the lipid raft model, over the whole simulated timespan, likely due to the larger system size and hence an increased number of initial contact points.

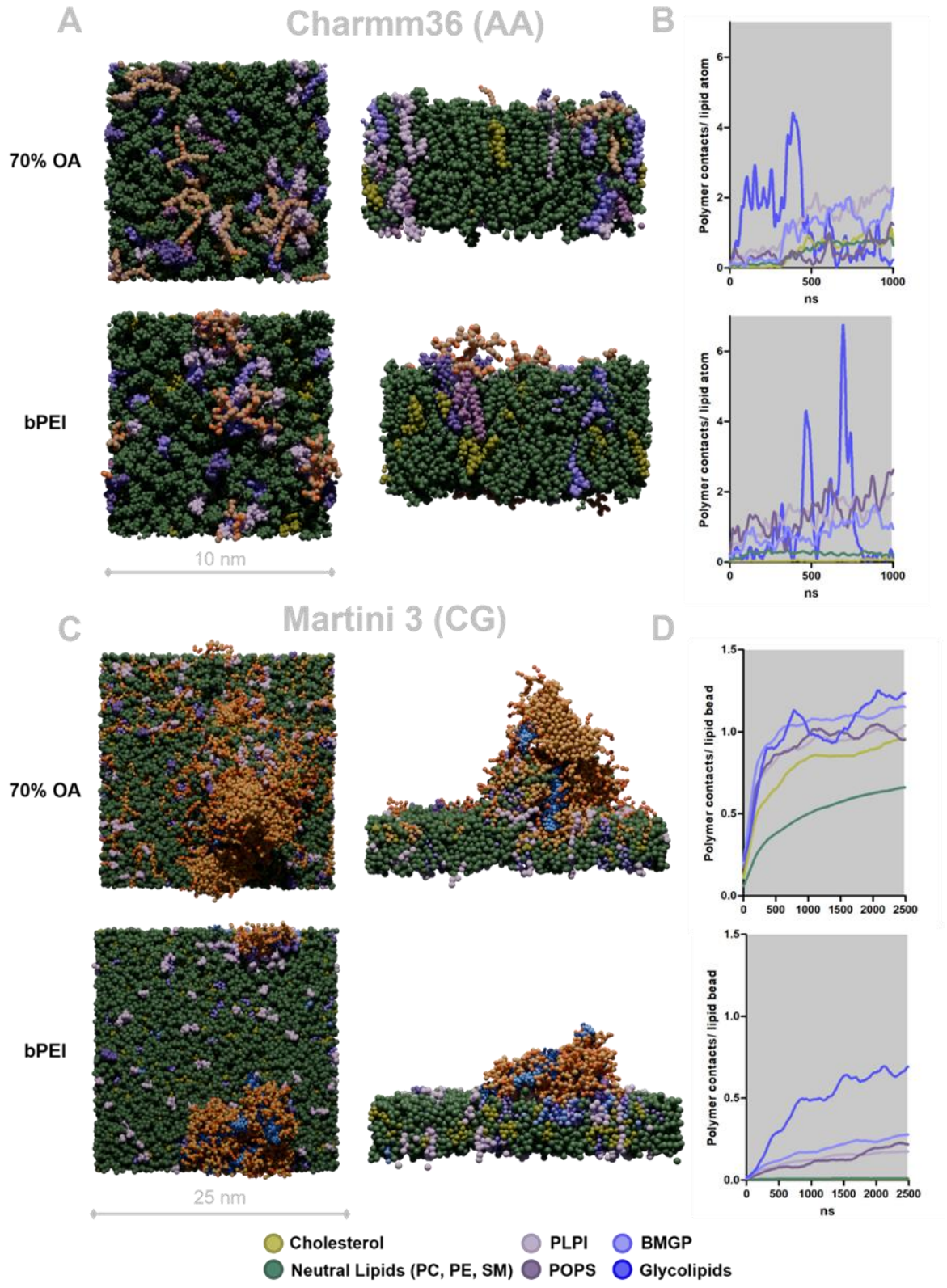

Figure IV.5. Contacts with late endosomal membrane lipids over time in AA and CG-MD simulations

A. Visualization of polymer – late endosome interactions (top- and side view) from AA simulations applying the charmm36 force field. **B.** Polymer contacts (upper: 70% OA PBAE, lower: bPEI) below 0.6 nm per membrane lipid atom (late endosome) over time, n = 2. **C.** Visualization of particle – late endosome interactions (top- and side view) from CG simulations in Martini 3. **D.** Polymer contacts (upper: 70% OA PBAE, lower: bPEI) below 0.6 nm per membrane lipid bead (late endosome) over time, n = 3.

3.4 Interaction of nanoparticles with membrane vesicles

For further investigation of potential EE mechanisms, all particles were simulated in endosome-mimicking CG membrane vesicles (Figure IV.S9). The vesicles had varied inner diameters between 19 nm (lipid raft) and 24 nm (lysosome) to acknowledge the fact that the lysosome tends to be larger than the early endosome[230]. In the early endosome and the lipid raft, simulations were begun with 1 µs at pH 7.4 protonation settings and then continued with 7 µs at pH 6.5. In the late endosome and the lysosome, pH 7.4 was only simulated for the first 0.6 µs, followed by 1.2 µs at pH 6.5 and prolonged to 8 µs at pH 5.4 protonation. Similarly to the previous results, the affinity of the polymers and the ionizable lipid MC3 to negatively charged lipids was observed (Figure IV.S8) with increasing contacts over time. In general, the number of polymer contacts per lipid bead rapidly increased in the initial ns and then stabilized towards the end of the simulations.

The EE of lipid-based systems, such as the LNP incorporated in this study, is believed to rely on membrane fusion and the disruption of the membrane bilayer[231, 232]. In the vesicle simulation setups, the LNP fused with the membrane, which caused rapid exchange of lipids between membrane and LNP. Similarly as recently portrayed by others[109], this caused disruption of the membranes and the formation of disordered phases in the vesicle (Figure IV.6A+B). However, in only one of the eight LNP-vesicle interactions, this led to successful escape of siRNA molecules from the vesicle (Figure IV.6A). Closer observation of this simulation revealed that the EE of two siRNA molecules in this simulation occurred directly during the initial fusion of LNP and vesicle. The energetic hurdle that must be overcome for the fusion of LNP and membrane to be initiated[123, 233] seemed to be increased in the interaction with the lipid raft model. Here, no membrane fusion occurred (Figure IV.6C) in one simulation, while in the repeated simulation fusion only occurred after ~ 3 µs (Figure S8). This can be explained by the absence of anionic lipids, as described above, or the presence of an increased amount of glycosylated lipids, forming a “buffer zone” above the membrane surface. The effect of pH in the endosomal compartments on the LNP-membrane interaction has been investigated in depth elsewhere[66], with the result that acidic pH (< 6.5) enhances LNP disintegration and promotes lipid exchange between LNP and endosomal membranes. This was well reproduced by our results, as each step of pH reduction in the simulations led to an abrupt increase in the number of contacts between LNP lipids and membrane (Figure IV.S8).

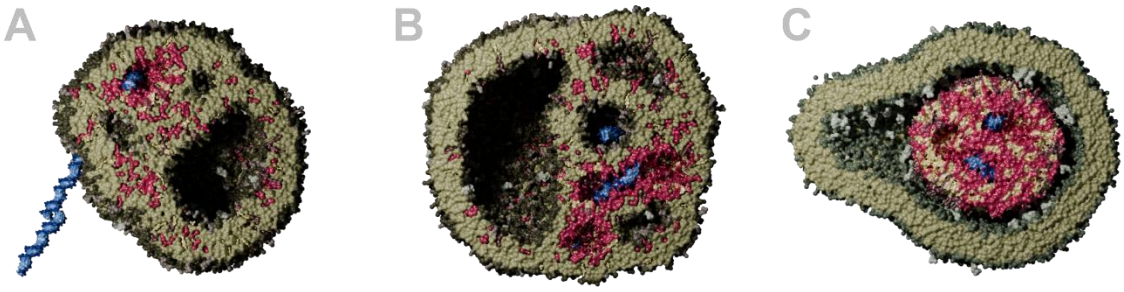

Figure IV.6. CG MD simulation outputs of an Onpattro® like LNP interacting with endosome mimicking vesicles for 8 µs. A. LNP and early endosomal vesicle. **B.** LNP and late endosomal vesicle. **C.** LNP and lipid raft vesicle. (green: membrane lipids, light gray: glycans, light green: cholesterol, blue: siRNA, pink: MC3/MC3H, purple: DSPC)

Interestingly, the 70% OA PBAE, even though to a smaller extent, caused membrane disturbances comparable to the LNP (Figure IV.7A). This formulation preferably interacted with the anionic lipids but was at the same time capable of forming hydrophobic interactions with all membrane lipids (Figure IV.S8). Over time, the polyplex disassembled and polymer molecules distributed over the whole vesicle (Figure IV.7A). In the lipid raft vesicle, the disintegration of the polyplex was less pronounced. Instead, incorporation of preferably cholesterol from the membrane into the hydrophobic PBAE core was observed (Figure IV.7B). Transmission electron microscopy (TEM) imaging has previously been used to visualize the effect of EE efficient polyplexes on endosomes[136]. Those images showed disturbed membranes that could be interpreted similar to the results from the vesicle- 70% OA PBAE polyplex simulations herein. However, no escape events were observed for the 70% OA PBAE polyplex. This may be attributed to the inherently low frequency of escape events, even in formulations considered effective for EE. Alternatively, the absence of detectable escape could suggest that PBAE-mediated EE involves a combination of membrane fusion and proton sponge-like mechanisms, which may have caused strong endosomal damage and Gal8 recruitment *in vitro*. In the vesicle simulations, chloride ions were inserted inside the vesicles to compensate for the increasing positive charge of the polymer under increasingly acidic conditions. However, this approach is unlikely to fully replicate the osmotic pressure dynamics that might develop physiologically.

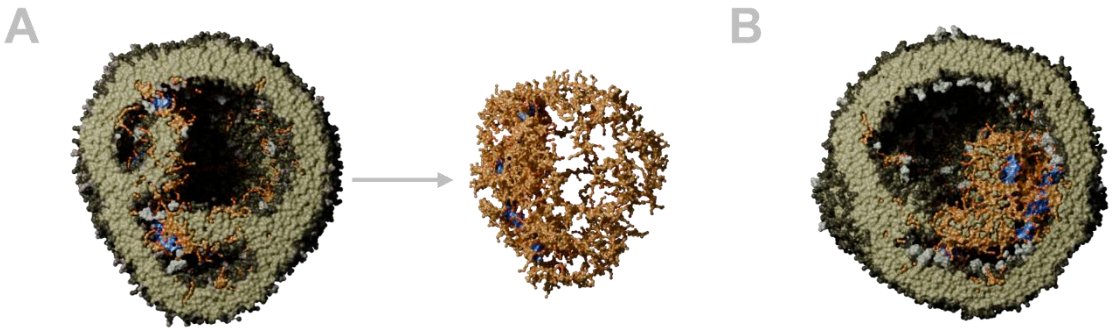

Figure IV.7. CG MD simulation outputs of 70% OA PBAE polyplex interacting with endosome mimicking vesicles for 8 µs. A. PBAE polyplex in the early endosomal vesicle (left), with visualization of disassembled polyplex only (right). **B.** 70% OA PBAE polyplex and lipid raft vesicle. (green: membrane lipids, light gray: glycans, blue: siRNA, beige/orange: polymer)

The more hydrophilic PBAE (30% OA) followed similar principles to the 70% OA PBAE, but due to the decreased hydrophobic interactions (Figure IV.S8), the effect of the particles on the vesicles was less pronounced (Figure IV.8A+B). Instead of polymer molecules fusing into the membrane, the interaction was dominated by surface contacts between the cationic spermines and the anionic lipids. Only minor disturbances of the membrane bilayer occurred. However, the vesicles deformed to a flattened shape, which allowed more surface contact with the polyplex (Figure IV.8B).

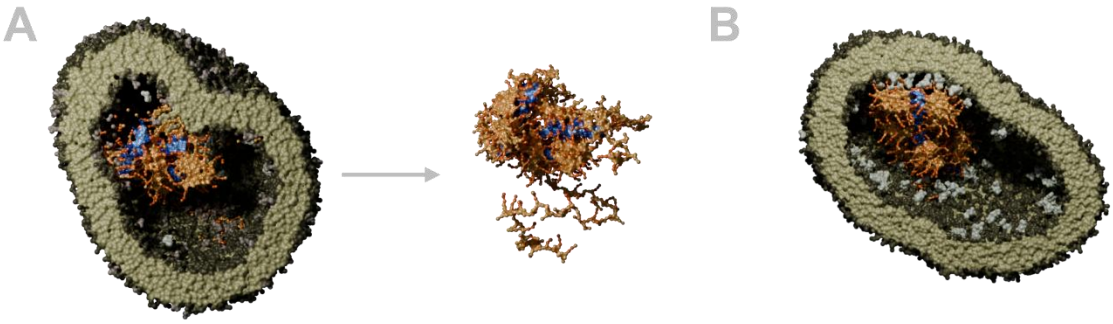

Figure IV.8. CG MD simulation outputs of 30% OA PBAE polyplex interacting with endosome mimicking vesicles for 8 µs. A. PBAE polyplex in the early endosomal vesicle (left), with visualization of disassembled polyplex only (right). **B.** 30% OA PBAE polyplex and lipid raft vesicle. (green: membrane lipids, light gray: glycans, blue: siRNA, beige/orange: polymer)

The effect of the bPEI polyplex on the membrane vesicles resembled the 30% OA PBAE, with the difference that the bPEI polyplex did not shed any polymer (Figure IV.9A-C). As mentioned above, no hydrophobic interactions of the hydrophilic bPEI polymer with the membranes were observed (Figure IV.S8). The minimal membrane interaction observed for bPEI in this setup is consistent with its limited endosomal escape efficiency in the Gal8 recruitment assay. However,

others have reported satisfying efficiency of PEI siRNA polyplexes before[35]. Some reported the formation of membrane pores due to the interaction with PEIs in simulation, however with the PEI being already placed in the membrane at the beginning of the simulation[234]. Neither our CG nor our AA models produced membrane pores in unstirred simulations. Only when the bPEI particle was not only pulled onto, but forcefully pulled through a membrane, a pore in the CG membrane formed (Figure IV.S10). In summary, this particle's results support a hypothesis formed by others on the EE of PEI polyplexes in HeLa cells[206]: The highly charged PEI polyplex firmly associates with the membrane, and local osmotic or mechanical forces are necessary for RNA release through local membrane defects into the cytoplasm. As described above, the buildup of osmotic pressure in our unstirred equilibrium simulations is limited, which makes the observation of escape events in this setup unlikely.

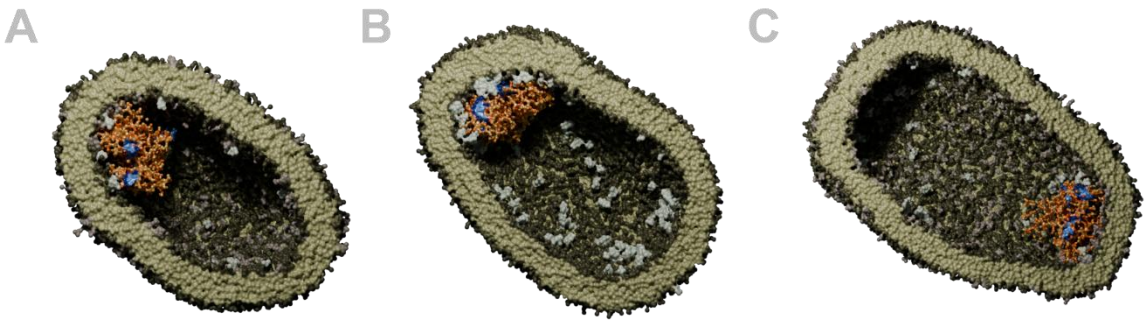

Figure IV.9. CG MD simulation outputs of the bPEI polyplex interacting with endosome mimicking vesicles for 8 µs. A. bPEI polyplex in the early endosomal vesicle **B.** bPEI polyplex in the lipid raft vesicle. **C.** bPEI polyplex in the late endosome vesicle. (green: membrane lipids, light gray: glycans, blue: siRNA, beige/orange: polymer)

Finally, the PPP polyplex performed comparably to the bPEI and the 30% OA particles (Figure IV.10A+B). As described for the planar membrane interaction, the PCL segment accumulated in the lipid tail region of the membranes, but only if the particle did not attach to the membrane surface with the bPEI residues first. In this case, the particle was hindered from hydrophobic interactions as the PEI stuck to the anionic membrane surface (Figure IV.10A). To investigate whether a larger PPP particle with therefore more hydrophobic units would cause membrane disturbance akin to the 70% OA polyplex, a PPP particle with a total polymer mass equal to the 70% OA particle was created. This polyplex caused some disturbance in the lysosomal membrane, but like the smaller particles, it did not disassemble (Figure IV.10C).

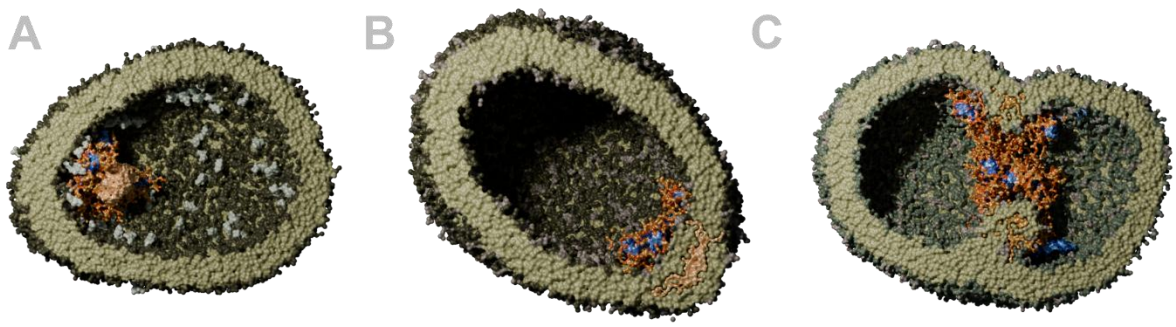

Figure IV.10. CG MD simulation outputs of the PPP polyplex interacting with endosome mimicking vesicles. A. Small PPP polyplex in the lipid raft vesicle **B.** Small PPP polyplex in the lysosomal vesicle. **C.** Larger PPP polyplex (containing 15 siRNA molecules) in the lysosomal vesicle. (green: membrane lipids, light gray: glycans, blue: siRNA, beige/orange: polymer (darker orange bPEI, PCL shown in brighter coloring)

The outcome of particle–vesicle interactions is summarized in Figure IV.11A, reporting the total number of contacts between polymer (or MC3 plus DPSC for the LNP) and membrane lipids in the final simulation frame. Consistent with the observations from planar membrane simulations, both the LNP and the 70% OA PBAE polyplex exhibited substantially higher membrane contact numbers compared to the other formulations. Specifically, the total number of contacts between 70% OA PBAE and membrane lipids was between 18.6-fold (lysosomal membrane) and 52.8-fold (early endosomal membrane) greater than that observed for bPEI. Hence, the difference can not solely be attributed to the overall higher amount of polymer in the PBAE polyplex, but also polymer specific properties. Furthermore, as noted previously, the presence of anionic lipids appeared to promote interaction, with late endosomal and lysosomal vesicles showing higher abundance of polymer or LNP contacts than early endosomal or lipid raft membranes.

Polyplex stability is known to depend on multiple interrelated factors, including polymer architecture, molecular weight, and hydrophobicity[55, 235]. In an effective polyplex formulation, these factors must be well balanced to ensure sufficient stability in serum and efficient cargo release following cellular uptake[236]. In our CG MD simulations, a comparison of polymer–siRNA contacts before and after endosomal membrane interaction revealed a reduction in siRNA encapsulation across all systems tested (Figure IV.11B), suggesting partial unpacking upon membrane contact. While no consistent trend emerged across membrane compositions, the results indicate that the 30% OA PBAE polyplex is the least stable, whereas the PPP-based polyplex shows the highest stability. Interestingly, the polyplex that exhibited the strongest membrane interaction (70% OA PBAE) did not show the most efficient siRNA unpacking. Nevertheless, comparisons between structurally related polymers (70% OA vs.

30% OA PBAE; PPP vs. bPEI) revealed that increased hydrophobicity was associated with reduced unpacking.

Noticeably, the MD-based unpacking results reproduced the outcome from an experimental stability assay (Figure IV.S11), in which competitive displacement by heparin and Triton X revealed an identical stability ranking among the four polyplexes. This correlation validates the predictive power of the simulation approach and highlights its ability to mechanistically dissect complex structure–function relationships.

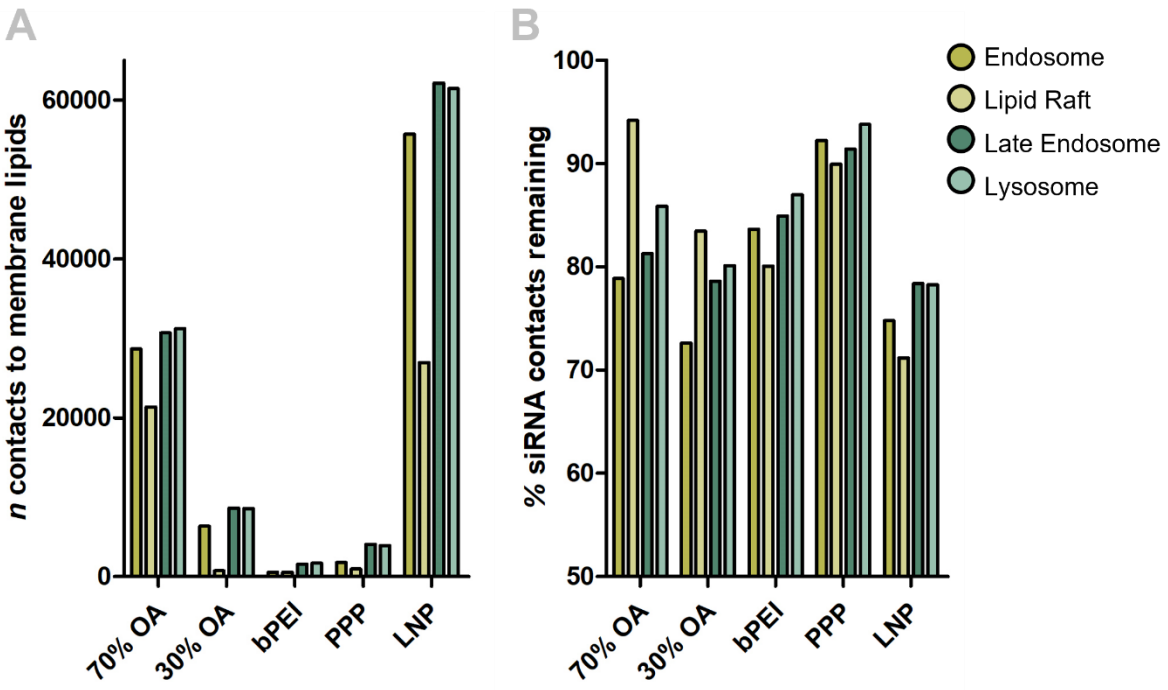

Figure IV.11. Quantification of CG MD output after 8 µs simulated interaction between endosomal membranes and model particles. A. Total number of contacts of the polymer (or DLin-MC3-DMG and DSPC for the LNP) with membrane components in the last frame of simulations (8 µs); shown as mean from n = 2 simulations per setup. **B.** Percentage of contacts of the polymer (or DLin-MC3-DMG and DSPC for the LNP) with siRNA that remained after 8 µs simulated interaction with model vesicles in comparison to t = 0 ns; shown as mean from n = 2 simulations per setup.

4 Conclusion

The herein presented MD simulations visualized and quantified the interaction of different siRNA nanoparticles with endo-lysosomal membranes. All formulations showed increased affinity to anionic membrane lipids, highlighting that these play a significant role for EE. However, only two formulations (the 70% OA PBAE polyplex and the Onpattro®-like LNP) achieved eGFP knockdown *in vitro*. These were the only particles that formed larger numbers of hydrophobic interactions in MD, extracting lipids from planar membranes and disturbing membrane vesicles. Hence, a pronounced role of hydrophobic interactions for effective EE through membrane fusion was demonstrated. Particles that do not contain hydrophobic residues (such as bPEI polyplexes) were not capable of interacting with the lipid tails of endosomal membranes.

Combining the findings of this work with the existing knowledge on EE mechanisms, we understand EE mechanisms of polyplexes as a spectrum ranging from proton sponge-like EE to membrane fusion-dominated mechanisms. For the EE of polyplexes based on hydrophilic polymers such as PEI, our simulations propose an electrostatically driven attachment of particles onto endosomal membranes, which could be followed by comparably rare escape events through the buildup of osmotic or mechanical stress. Larger hydrophobic modifications of a polymer are necessary for hydrophobic interactions to arise, which enhances membrane disruption and polymer shedding. By exploiting both proton-sponge like and membrane fusion-based mechanisms, the amphiphilic polyplex formulations (represented herein by 70% OA PBAE polyplexes) possess increased EE efficiency, but also cause large membrane defects, visible *in vitro* through the observation of Gal8 recruitment. This type of polyplex is efficient at siRNA delivery, but potentially cytotoxic through excessive endosomal disruption.

In our simulations, the Onpattro®-like LNPs caused the highest extent of membrane disruption through fusion of LNP and membrane and the mixing of lipids. *In vitro*, the formulation produced only small holes in the endosome, which were not detectable by galectins. Considering the cytotoxicity caused by large endosomal defects, the EE mechanism of the simulated LNP appears desirable. Engineering polyplexes towards more membrane fusion-based EE, for example by modifying hydrophobic residues, could therefore largely advance the development of polymers for siRNA delivery.

Even though escape events of siRNA from polyplex formulations were not observed in simulation, our results show that MD simulations of EE mechanisms can conclusively be correlated to *in vitro* results. In the future, expanding the library of simulated nanoparticle-membrane systems will help to solidify the identification of desirable EE mechanisms in MD simulations. Subsequently, MD could be used to predict EE behavior of a formulation and screen for beneficial properties.

5 Materials and Methods

5.1 Materials

Spermine and oleylamine for the synthesis of the poly(beta)aminoesters (PBAE) were obtained from Fisher Scientific (Acros, USA), whereas the 1,4-butanediol diacrylate for the PBAE backbone originated from Tokyo Chemical Industry Co. (Tokyo, Japan). The 25 kDa branched polyethylenimine (bPEI) and the 5 kDa bPEI for the synthesis of the PEI-PCL-PEI polymer (PPP) were a kind gift from BASF (Ludwigshafen, Germany). Polycaprolactone diacrylate (PCL), as well as HEPES (4-(2-hydroxylethyl)-1-piperazineethanesulfonic acid), Dulbecco's Phosphate Buffered Saline (PBS), D-Glucose, Triton-X, porcine Heparin sodium salt, Cholesterol and Copper sulfate pentahydrate, Minimum Essential Medium Eagle (MEM), High/Low glucose Dulbecco's Modified Eagle Medium (DMEM), fetal bovine serum (FBS), MEM Non-Essential Amino Acids (NEAA) solution (100X) and Cell Counting Kit-8 were obtained from Sigma-Aldrich (Taufkirchen, Germany). D-Lin-MC3-DMA was from MedChemExpress (Sollentuna, Sweden), DSPC and DMG-PEG 2000 from Avanti Research (Birmingham, United Kingdom). The siRNA used in this project was amine-modified siRNA for the knockdown of eGFP (siGFP), with the sequence 5´-pACCCUGAAGUUCAUCUGCACCACcg, 3´- ACUGGGACUUCAAGUAGACGGGUGGC, or negative control siRNA (siNC) with the sequence 5´-pCGUUAAUCGCGUAUAAUACGCGUAT, 3´-CAGCAAUUAGCGCAUAUUAUGCGCAUA, both purchased from Merck (Darmstadt, Germany). Dyes for confocal microscopy (DAPI (4',6-Diamidin-2-phenylindol, Dihydrochloride), Alexa-Fluor 647) were obtained from Life Technologies GmbH (Frankfurt, Germany). Penicillin-Streptomycin (P/S, 10.000 U/ml), Blasticidin S HCl (10 mg/ml), Lipofectamine 2000, 4% Paraformaldehyde in PBS and DAPI (4′,6-diamidino-2-phenylindole) were bought from Thermo Fisher (Waltham, MA, USA). CytoTox 96® Non-Radioactive Cytotoxicity Assay kit was purchased from Promega Corporation (Madison, WI, USA).

5.2 Experimental Methods

Polymer Synthesis

The poly(beta)aminoesters (PBAE) were synthesized via Michael Addition as previously described[55]. The synthesis was based on tri-boc-spermine as hydrophilic side chain, oleylamine (OA) as hydrophobic side chain, and 1,4-butanendiol diacrylate as backbone. After polymerization, the tri-boc-spermine was deprotected with trifluoroacetic acid. The ratio of hydrophilic spermine to hydrophobic OA was controlled by the input ratio of the reagents and validated by ^{1}H nuclear magnetic resonance (NMR). For this work, a polymer containing 33% OA (generally referenced as “30% OA” for clarity in the comparison to simulation) and 68% OA (“70% OA”) were used.

The synthesis of the 5 kDa-5 kDa-5 kDa PEI-PCL-PEI polymer (PPP) was previously described by Jin et al.[214] In brief, 5 kDa branched polyethylenimine (bPEI) was stirred with polycaprolactone-diacrylate (PCL) for 48 h at 40 °C at a molar ratio of 2 (PEI) : 1 (PCL). Then the polymer was purified from monomers by dialysis against water with a molecular weight cut-off of 10 kDa and subsequently lyophilized. The ratio of PEI:PCL in the product was evaluated to be 2:1 by a TNBS assay, which was calibrated with unmodified 5 kDa PEI[237].

Particle Formulation

PBAE and bPEI Particles: PBAE and 25 kDa bPEI polyplexes were formulated at an N/P ratio of ten (i.e., ten protonable units of the polymer per phosphate of the siRNA). The polymers and the siRNA were separately diluted in 10 mM HEPES buffer at pH 5.4 to equal volumes. For the particles used in the hemolysis assay, HEPES- buffered Glucose (5%) (HBG) at three different pH levels (7.4, 6.5 and 5.4) was used instead to ensure isotonicity. Both components were mixed by batch-mixing and shortly vortexed afterwards. Finally, the particles were incubated for 90 minutes at room temperature before further use.

PPP Particles: The PPP particles were prepared as previously described[214] by preparing empty particles first and subsequently adding the siRNA. The polymer was dissolved in acetone, and then slowly dripped into formulation buffer (as above) while stirring. The acetone was left to evaporate from the mixture over three hours, and the formation of empty particles was confirmed by dynamic light scattering (DLS). Then, siRNA loaded polyplexes were prepared by diluting the empty particles and mixing as described above for the PBAE and bPEI particles.

MC3 – LNP: For the preparation of LNPs, the lipids were diluted in ethanol, with ratios of 50% Dlin-MC3-DMA, 38.5% cholesterol, 10% DSPC and 1.5% PEG-2000-DMG. The siRNA was diluted in 25 mM sodium acetate buffer at pH 4. Lipid blend and siRNA were combined by

microfluidic mixing in a T-mixer (micro IDEX H&S P-888) at flow rate ratios of 0.75 ml/min (lipid) and 2,25 ml/min (siRNA). Afterwards, the LNPs were dialyzed overnight against 150 mM PBS or HBG when used for the hemolysis assay. Before further use, the LNPs were filtered through a 0.22 µm syringe filter.

Z-average, PDI and ζ-potential of all particles were determined on a Malvern Zetasizer Ultra (Malvern Instruments, Malvern, UK). All particles were produced in biological triplicates for characterization.

Hemolysis Assay

For the hemolysis assay[238], blood from a healthy anonymous donor was centrifuged for 10 minutes at 1500x g. The sedimented erythrocytes were resuspended in PBS and repeatedly washed with PBS until the supernatant was clear after centrifugation. The erythrocytes were resuspended in PBS again and then diluted to 5 * 10^8/ml in HBG with either pH 5.4, 6.5 or 7.4. Subsequently, 1:1 mixtures of erythrocytes and the respective particles (50 pmol siRNA/ 100 µl) or 15 mg/ml polymer dilutions were then incubated in 96-well plates for 30 minutes at 37 °C. 1% Triton-X was used as positive control (i.e., 100% hemolysis) and buffers as negative controls. After incubation, the plates were centrifuged for 5 minutes at 1500x g and the supernatants were transferred to fresh transparent well plates. The absorbance of the supernatants was measured at 541 nm on a TECAN Spark Plate Reader (Tecan Trading AG, Switzerland). The assay was performed in a biological triplicate. Erythrocyte aggregation was documented on the resuspended erythrocyte pellets on a Evos M5000 microscope (Thermo Fisher Scientific, Schwerte, Germany).

Particle Stability Assay

The stability of polyplex formulations was assessed by a competition assay at pH 5.4, as previously described elsewhere[55]. Briefly, a dilution series of stress solutions containing heparin and Triton X was prepared. In this regard, 100% stress referred to a concentration of 200 USP units heparin/ml and 1% (m/m) Triton X. First, 10 µL of nanoparticles formulated at pH 5.4 were incubated with 20 µL of the respective stress solution for 1 h at 37 °C. Then, 5 µL of diluted SYBR Gold solution was added and after 5 minutes, fluorescence was measured on a TECAN Spark Plate Reader (Tecan Trading AG, Switzerland). Excitation was set to 492 nm; emission was set to 537 nm. For data analysis, all data points (n = 3 technical replicates) were normalized towards the 100% stress sample of each formulation, which was assumed to represent maximal unpacking (i.e., 0% encapsulation). To calculate the EC50 value of each formulation, a sigmoidal curve fit with automated outlier detection was performed in GraphPad Prism5 2007 software.

Cell culture

Hela WT cells (passages 10-15) were cultured in MEM containing 10% FBS, Hela/eGFP cells (ATCC, USA, passages 5-10) were cultured in DMEM-high glucose containing 10% FBS, 0.1 mM MEM NEAA, 1% P/S and 10 µg/mL Blasticidin. Hela-Gal8-mRuby3 cells (passages 5-10) were kindly provided by Professor Ernst Wagner (Ludwig-Maximilians-Universität Munich, Germany) and cultured in DMEM-low glucose with 10% FBS and 1% P/S. All cells were cultured in a humidified atmosphere containing 5% CO_2 at 37 °C.

Galectin-8 Assay

The recruitment of Galectin-8 (Gal8) to damaged endosomes as an indicator of successful endosomal escape was tested on HeLa cells expressing mRuby-3-Gal8 fusion protein. Cells were seeded at a density of 10,000 cells per well in an 8-well ibiTreat chamber slide (Ibidi, Gräfelfing, Germany). The cells were transfected with nanoparticles containing 20 pmol siRNA per well for 4 hours or 24 hours. Of the total siRNA, 20% were labeled with Alexa Fluor 647. The culture medium was changed after 4 hours, and cells were imaged at the SP8 inverted confocal laser scanning microscope (CLSM; Leica Camera, Wetzlar, Germany) with a 63X oil objective. Cell nuclei were stained with DAPI. siRNA uptake and Gal8 puncta of ≥ 25 cells per sample were quantified from the images by automated counting using the Fuji plug-in of Image J.

eGFP Knockdown

HeLa/eGFP cells were seeded at a density of 6,000 cells per well in 96-well plates. The following day, cells were transfected with nanoparticles containing either 20 pmol siRNA targeting eGFP mRNA (siGFP) or 20 pmol scrambled siRNA of the same length (siNC) for 48 hours. Lipofectamine 2000 was used as a positive control, while free siRNA served as a negative control. After incubation, the cells were collected to perform the FACS analysis (Attune NxT Flow Cytometer, ThermoFisher Scientific). The eGFP knockdown efficiencies (biological duplicate with n = 3 technical replicates) were calculated by dividing the Median Fluorescence Intensity (MFI) of siRNA-treated group by that of the respective siNC-treated group.

Cellular uptake

HeLa/eGFP cells were seeded at a density of 6,000 cells per well in 96-well plates. The following day, cells were transfected with nanoparticles containing 20 pmol siGFP, of which 20% were labelled with Alexa Fluor 647. Lipofectamine 2000 was used as a positive control, while free siRNA served as a negative control. After 24 hours, the cells were collected to perform the FACS analysis (Attune NxT Flow Cytometer, ThermoFisher Scientific).

Additionally, uptake was analyzed by FACS after quenching the fluorescent signal on the cell surface with trypan blue (n = 3 technical replicates).

LDH- and CCK-8 Assay

To evaluate cytotoxicity, both an LDH- and a CCK-8 assay were conducted (n = 3 technical replicates). The particles for this experiment were prepared as described above and then diluted to test four concentrations (i.e., 40, 30, 20 and 10 pmol siRNA/50 µL). HeLa cells were seeded at 6,000 cells in 96 well plates. When reached 80% confluence, the cells were incubated with the four nanoparticle dilutions for 48 hours. For the LDH-assay, 50 µL cell culture supernatant was diluted 1:1 with CytoTox 96 reagent and incubated in the dark for 30 minutes at room temperature. After addition of 50 µL stop solution, the samples were quantified at 490 nm absorbance, and the results were normalized to the positive control. The cells pre-treated with 20 µL of lysis solution for 45 minutes at 37°C served as positive control for maximum LDH release. For the CCK-8 assay, 10 µL CCK-8 solution was added directly into each well containing treated cells and incubated for another 3 hours. The cell viability was quantified by absorbance relative to an untreated sample at 450 nm.

5.3 CG-MD Simulation

All simulations were run in Gromacs 2021.4-plumed[184]. For the CG simulations, the Martini 3 force field[97] was applied. The CG model particles were generated with our previously established siRNA model[134] and contain three siRNA molecules each. The number of polymer molecules was chosen to reach ~ N/P 10 for all polyplexes, whereas the MC3 – LNP had a final N/P ratio of 6.5. After minimization and NPT equilibration, all simulations were run at a timestep of 15 fs with Particle mesh Ewald (PME) electrostatic handling[239] with a cutoff of 1.1 nm. Temperature was controlled by v-rescale temperature coupling at 298 K (particle assembly) or 310 K (membrane interactions), whereas pressure was handled by the Parrinello-Rahman barostat[193] at 1 bar.

CG Particle Models

PBAE and bPEI Particles: The PBAE model particles were generated in accordance with our previously established approach for this group of polymers[134] with either a 30% Oleylamine (OA) or a 70% OA polymer model. The bPEI particles were generated the same way, based on a 25 kDa PEI model with a branching degree of 59%[133] (bPEI). PBAE or bPEI particles initially self-assembled in a 5 µs unbiased run in a cubic box with 26 nm side length. Boxes were solvated with 10 mM HEPES and neutralized with chloride ions. During the first run, the protonation corresponded to pH 5.4. This run was followed by 0.5 µs run time with reduced

polymer protonation, allowing the particles to adjust to a theoretical pH 7.4. To generate input for the interaction with planar membranes at pH 6.5 or 5.4, the protonation was subsequently adjusted for another 0.5 µs. All particles were extracted from their initial assembly box including the ions of their hydration shell to ensure the particle stability in new simulation boxes with PME electrostatics.

PPP Particles: The PPP polymer model was created from two identical 5 kDa bPEI models[133] that were connected by a 5 kDa PCL chain. The parametrization of this PCL chain was obtained according to the common Martini parametrization approach (*cgmartini.nl/index.php*)[185-188]. To ensure a particle constitution comparable to wet-lab experiments, the PPP polymer was left to self-assemble for 3 µs under the simulation conditions described above. The siRNA molecules were then added to the empty particle in a subsequent 2.5 µs simulation for encapsulation. pH adjustments were done in the same way as for the PBAE and bPEI particles.

MC3 – LNP: The MC3 – LNP with an Onpattro® – like composition was assembled following the recently published approach by Kjølbe et al.[109] The siRNA is placed in water channels within a hexagonal lipid core, covered by an outer lipid layer. This resulted in a particle consisting of 49% MC3, 39% Cholesterol and 12% DSPC and a total N/P ratio of ~ 6.5. PEG-lipids were not incorporated, as they are expected to be already shed from the LNP when it reaches the endosomal compartment of cells[215]. Protonation of MC3 was calculated based on the apparent pKa of 6.55 for MC3[31], however the lipids in direct contact with the siRNA were kept protonated at all pH levels studied to avoid excessive shedding of siRNA from the LNP at pH 7.4.

All particle models and the chemical structures of the polymers are depicted in Figure IV.1.

Membrane Models

To study the interaction of nanoparticles with different membrane compositions present in the endo-lysosomal pathway, four different membrane types were established, namely an early endosomal membrane, a lipid raft, a late endosomal membrane and a lysosomal membrane. The respective compositions were adapted from literature[226, 240-244] and are listed in table S1. The initial topologies were generated with the INSANE[137] tool. Lipid topologies were used from literature[97, 245, 246] or created based on the established building blocks if not yet available in Martini 3 (e.g., bis(monoacylglycero)phosphate (BMGP), glycolipids (DPG1 and DPG3[106, 245])). All planar models had an initial size of 25x25 nm and were simulated with semi-isotropic pressure scaling. The membranes were fixed in their position by restraints on the z-coordinate applied to the POPC molecules (in case of the lipid raft, only 50% of POPC molecules) with a force constant of 1000 kJ/mol*nm^2. Lateral diffusion of lipid components

(POPC, DPSM or cholesterol) inside the planar models was analyzed with the mean squared displacement tool[196, 247] from the MDAnalysis package[194, 248]. For the vesicular models, membrane discs with a radius of 25 nm (early endosome), 26 nm (lipid raft) or 28 nm (late endosome, lysosome) were generated. To initiate the formation of vesicles, the membranes' center of mass (COM) was pulled out of the plane in z-direction by a moving restraint applied with the PLUMED plugin. Afterwards, closed vesicles formed in an unbiased simulation within less than 1 µs.

Umbrella Sampling

The lipophilicity of the simulated CG polymer models was characterized by the calculation of a logP/ kDa according to eq. 1:

$$logP/kDa = (\frac{\Delta G_{w/o}}{2.303\ RT})/MW_{polymer} \quad (1)$$

The free energy $\Delta G_{w/o}$ of transferring one polymer molecule from an octanol phase to a water phase was determined in umbrella sampling simulations[115, 249]. A polymer molecule and neutralizing chloride ions were placed in the center of an octanol phase of 9x9x20 nm. Then the molecule was pulled into the adjacent water phase with equal dimensions by a harmonic potential applied along the z-axis. A spacing of 0.25 nm was used for the umbrella windows, resulting in 65 windows, which were simulated for 20 ns each. The potential of mean force (PMF) was generated as a function of distance from initial position by weighted histogram analysis with the gmx *wham* function[116, 250, 251].

Planar Membrane Interactions

For the investigation of particle-membrane interactions in a simple, planar setup, the 25x25 nm membranes were simulated with each model particle (70% OA PBAE, 30% OA PBAE, bPEI, PPP and LNP) in triplicate runs. The box had a z-dimension of 35 nm, and the membranes were centered at z = 10 nm. All boxes were solvated with 150 mM NaCl and simulated at 310 K. The interactions with the early endosome and the lipid raft were simulated at pH 6.5, whereas late endosome and lysosomal interaction was simulated with protonation settings of the particles corresponding to pH 5.4. To ensure interaction from the glycosylated membrane leaflet, the particles were pulled in contact with the membrane by a moving restraint with the PLUMED plugin, lasting for 5 ns. Then a 2495 ns unbiased interaction was simulated with the above-mentioned settings. For analysis, the mass density distribution along the z-axis was calculated vie the gmx *density* function, defining the center of the membrane as z = 0. The amount of membrane components extracted from the membrane plane was calculated from the density distribution, where the upper limit of the membrane area was defined as the point, where the first derivative of the density distribution was > -100.

Vesicle Interactions

Additionally, the interaction of particles with the inside of endosome-mimicking vesicles was simulated to compare a more realistic setup. Particles were placed inside the preformed vesicles and solvated with 150 mM NaCl at 310 K in cubic boxes with 40 or 42 nm side length. All setups started with protonation corresponding to pH 7.4. For the early endosome and the lipid raft, the pH was reduced to 6.5 after 1 µs, which was then followed by 7 µs simulation at the mildly acidic pH. In the late endosome and the lysosome vesicle, pH was reduced to 6.5 after 0.5 µs, and then further reduced to pH 5.4 after another 1.2 µs, at which additional 6.3 µs were simulated. The additional chloride ions needed to neutralize the polymer charge after each pH change were placed inside the vesicle to mimic the osmotic pressure increase inside the endosome. Overall, every vesicle-particle setup was simulated for 8 µs and every setup was simulated twice. The vesicle interactions were analyzed for the number of polymer–membrane contacts over time using the gmx *mindist* tool and for changes in the siRNA environment via the Radial Distribution Function (RDF).

5.4 AA Models and Simulations

The AA simulation input was generated with CHARMM-GUI[252, 253] using the CHARMM36 force field[254]: Planar membrane models with a size of 10x10 nm and lipid compositions identical to the CG membranes were built by the Membrane builder[255-257]. Polymer models with a reduced molecular weight (trimers for PBAEs, i.e. ~ 1.3 kDa; bPEI and PPP ~ 1.8 kDa) were obtained through the Ligand Reader & Modeler[258]. All AA simulation boxes were neutralized and solvated with 150 mM sodium chloride. The simulations were run as NPT ensembles with the standard settings supplied by CHARMM, i.e. PME electrostatic handling, semi-isotropic pressure scaling with the c-rescale barostat, v-rescale thermostat at 310.15 K and a timestep of 2 fs. The membranes were first simulated for 500 ns without interacting polymers. For the simulation of polymer-membrane interactions, ~ 9 kDa total mass of a polymer were used. The PBAEs were simulated separately for 500 ns to form micelles similar as the CG model and then further used in this form. The bPEI and the PPP models were used as individual molecules, as they did not aggregate within 500 ns (for PPP unlike the CG model – arguably due to the reduced MW and therefore length of the PCL segment). All polymers were placed in proximity to the glycosylated membrane leaflets in a 10x10x18 nm box. To facilitate initial contact with the membrane, a short pulling sequence mediated by a PLUMED moving restraint was applied to the polymer molecules. The polymer-membrane interactions were simulated in duplicates for 1 µs and analyzed with the gmx *mindist* tool.

5.5 Data Analysis and Visualization

Graphs were created in GraphPad Prism5 2007 software, which was also used for statistical analysis, where applicable. Simulations were visualized in Blender 4.5.2 LTS.

6 Supplementary Data

Table IV.S1. Composition of model membranes [%]
Percentage of lipid components by headgroup type in the four different simulated membrane types. Anionic lipids are marked in blue.

	Early Endosome		**Lipid Raft**		**Late Endosome**		**Lysosome**	
% Cholesterol		**29.5**		**45.0**		**20.1**		**20.1**
Phosphatidylcholines (PC)	POPC	17.0	POPC	27.5	POPC	11.0	POPC	11.0
	PIPC	15.1			PIPC	18.1	PIPC	18.1
	PAPC	5.5			PAPC	6.0	PAPC	6.0
Phosphatidylethanolamines (PE)	PIPE	4.1			POPE	11.5	POPE	11.5
	PAPE	6.8			PAPE	11.5	PAPE	11.5
Sphingomyelins (SM)	DPSM	7.1	DPSM	25.5	DPSM	2.7	DPSM	2.9
	PGSM	7.1			DXSM	2.7	DXSM	2.9
Phosphatidylserines (PS)					POPS	2.0	POPS	2.0
Phosphatidylinositols (PI)	PIPI	7.3			PIPI	8.0	PIPI	8.0
Glycolip-monosialohexosylganglioside (DPG)	DPG1	0.2	DPG1	1.0	DPG1	0.2		
	DPG3	0.2	DPG3	1.0	DPG3	0.2		
Bis(monoacylglycero)phosphate (BMGP)					BMGP	6.0	BMGP	6.0
% neg. lipids (sum)		**7.7**		**2.0**		**16.4**		**15.9**

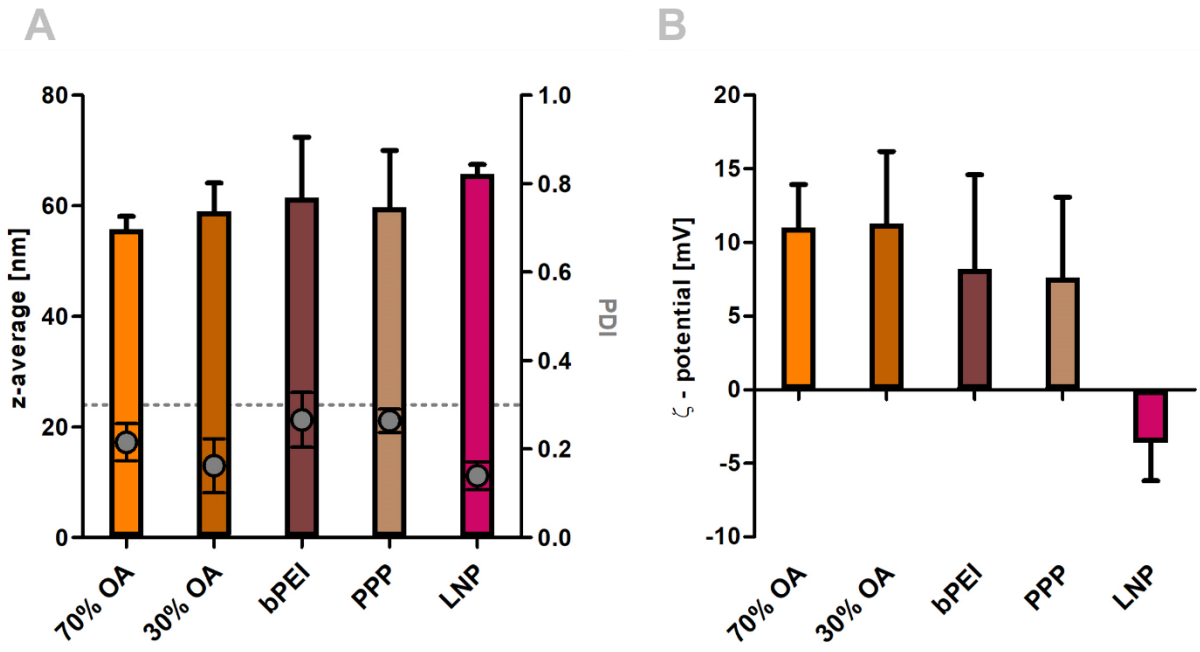

Figure IV.S1. Size and ζ-potential of nanoparticles A. Bars: Hydrodynamic diameters shown as z-average in nm, mean ± sd, n = 3; Dots: PDI, mean ± sd, n = 3. **B.** ζ-Potential in mV, mean ± sd, n = 3.

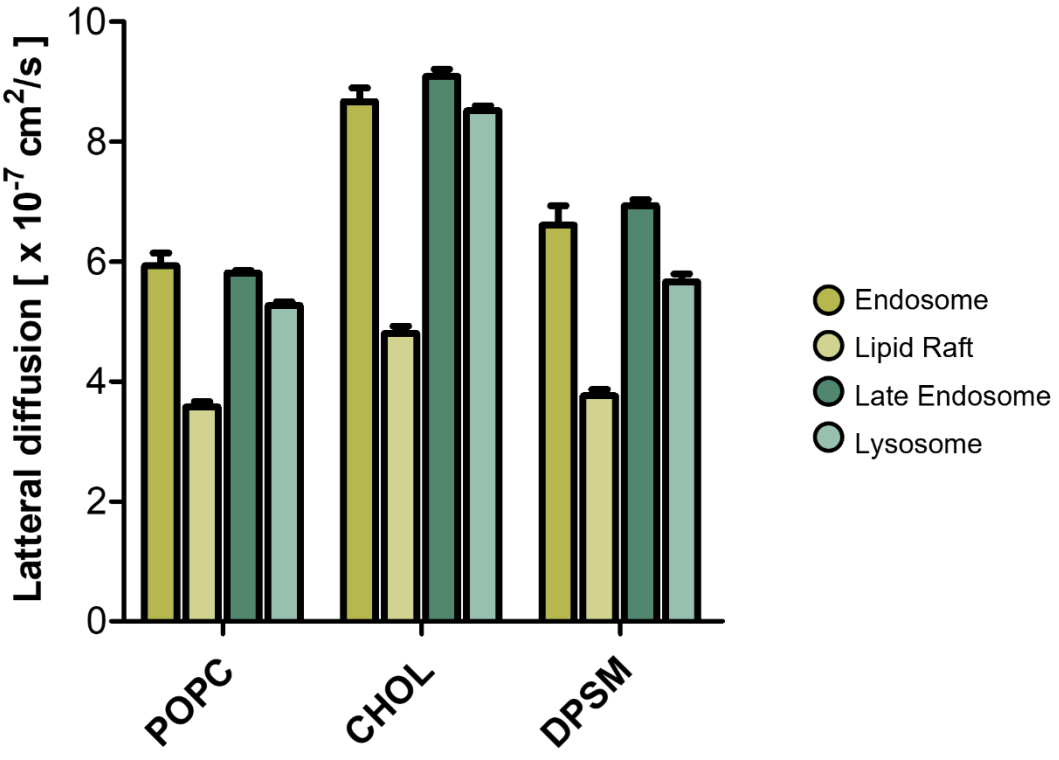

Figure IV.S2. Lateral diffusion [x 10-7 cm^2/s] of membrane lipids in the different CG membrane models.

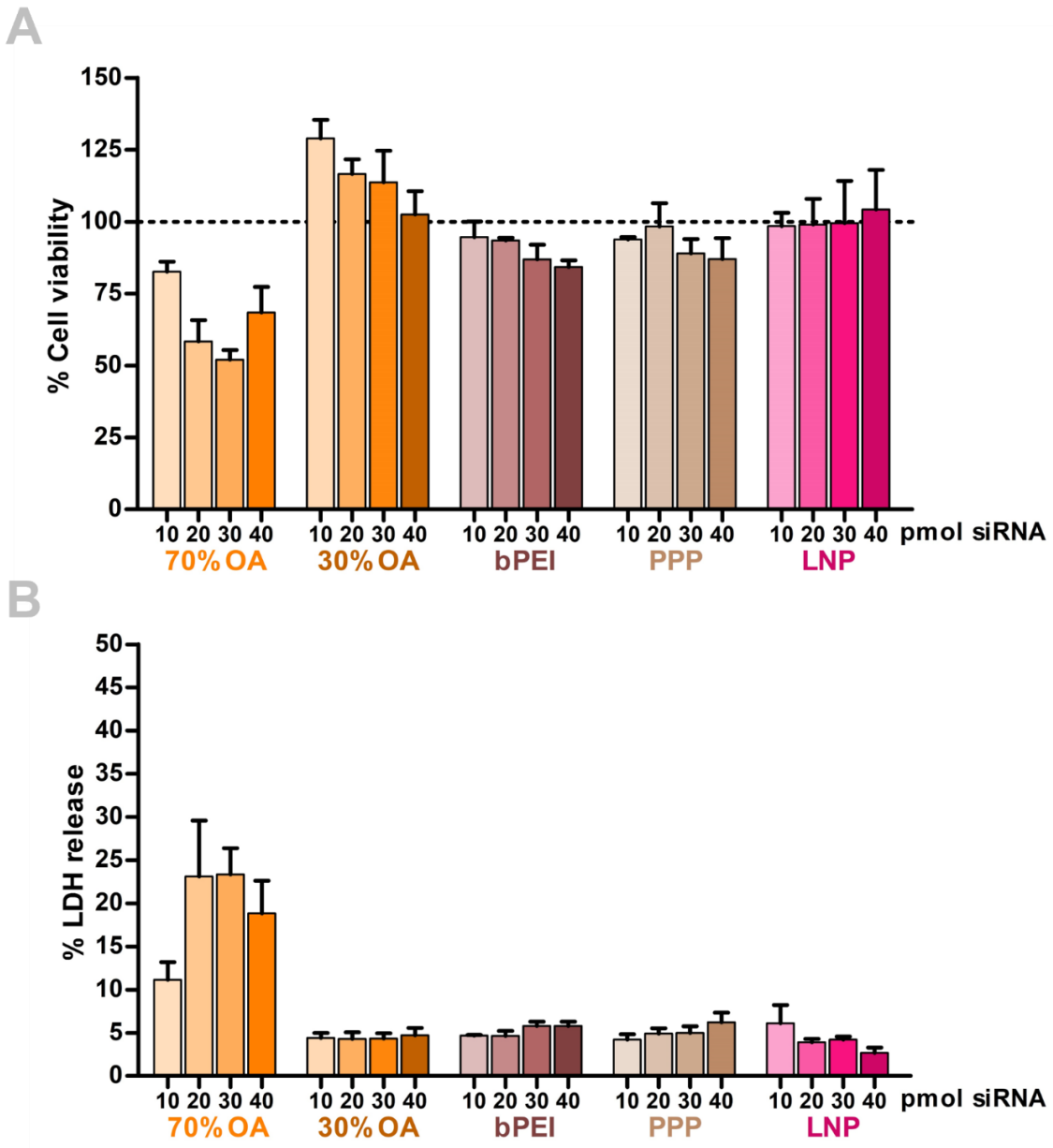

Figure IV.S3. CCK8 and LDH release assay in HeLa cells. A. Cell viability [%] calculated from CCK8 assay with 4 different nanoparticle concentrations, mean ± sd, n = 3. **B.** LDH release [%] calculated from the same 4 concentrations of nanoparticles, mean ± sd, n = 3.

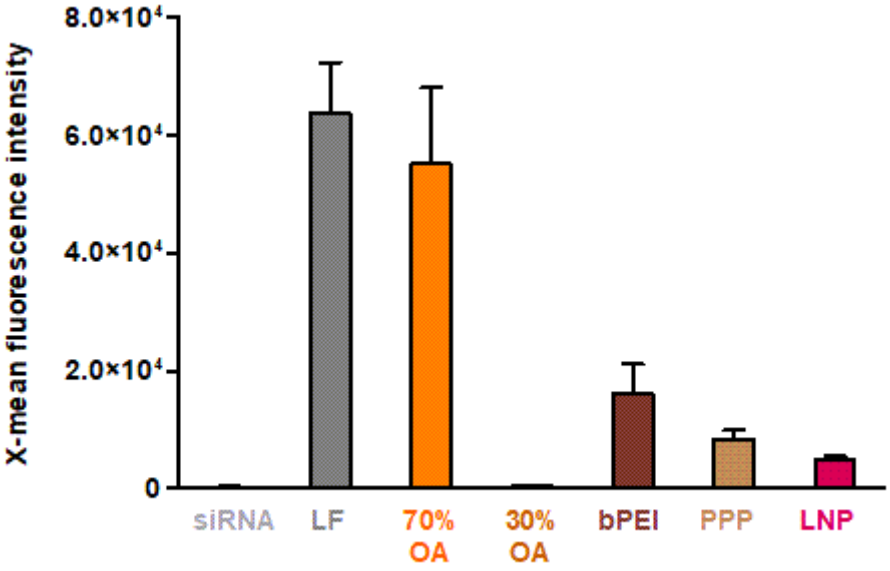

Figure IV.S4. Cellular uptake in HeLa-eGFP cells, 24 h after transfection with 20 pmol of nanoparticles containing 20% AF647-labelled siGFP, mean ± sd, n = 3.

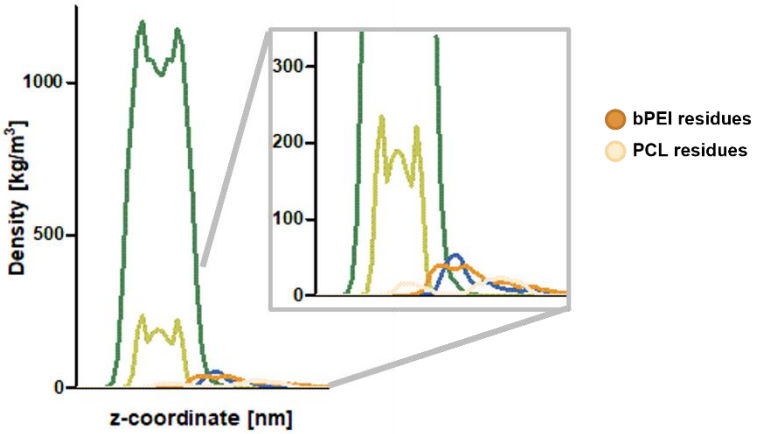

Figure IV.S5. Density distribution [kg/m^3] after interaction of PPP polyplexes and late endosomal membranes.

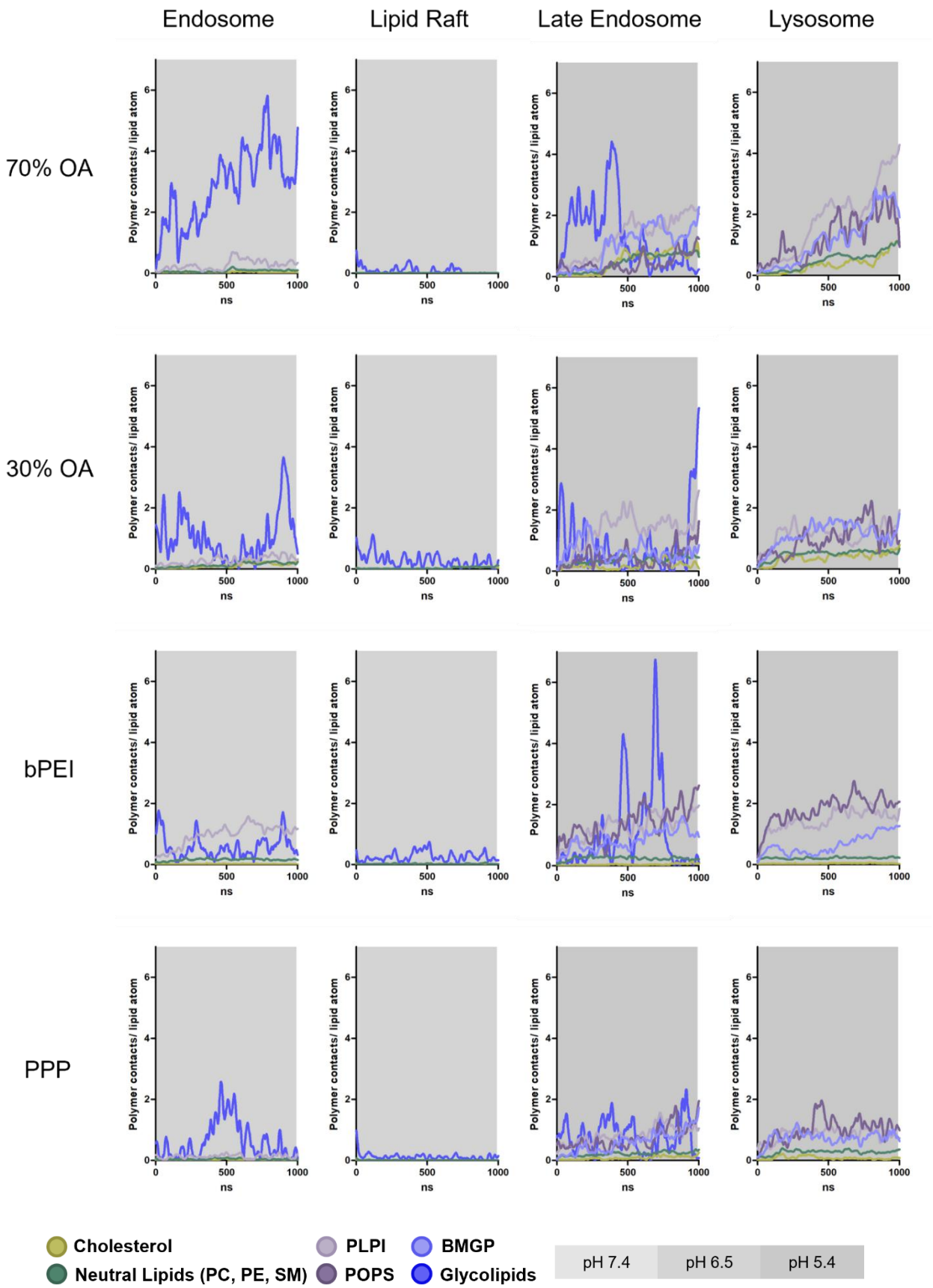

Figure IV.S6. Interaction of polymer models (in total 9 kDa polymer per simulation box) with planar membranes at AA resolution: Polymer contacts below 0.6 nm per membrane lipid atom over time, n = 2.

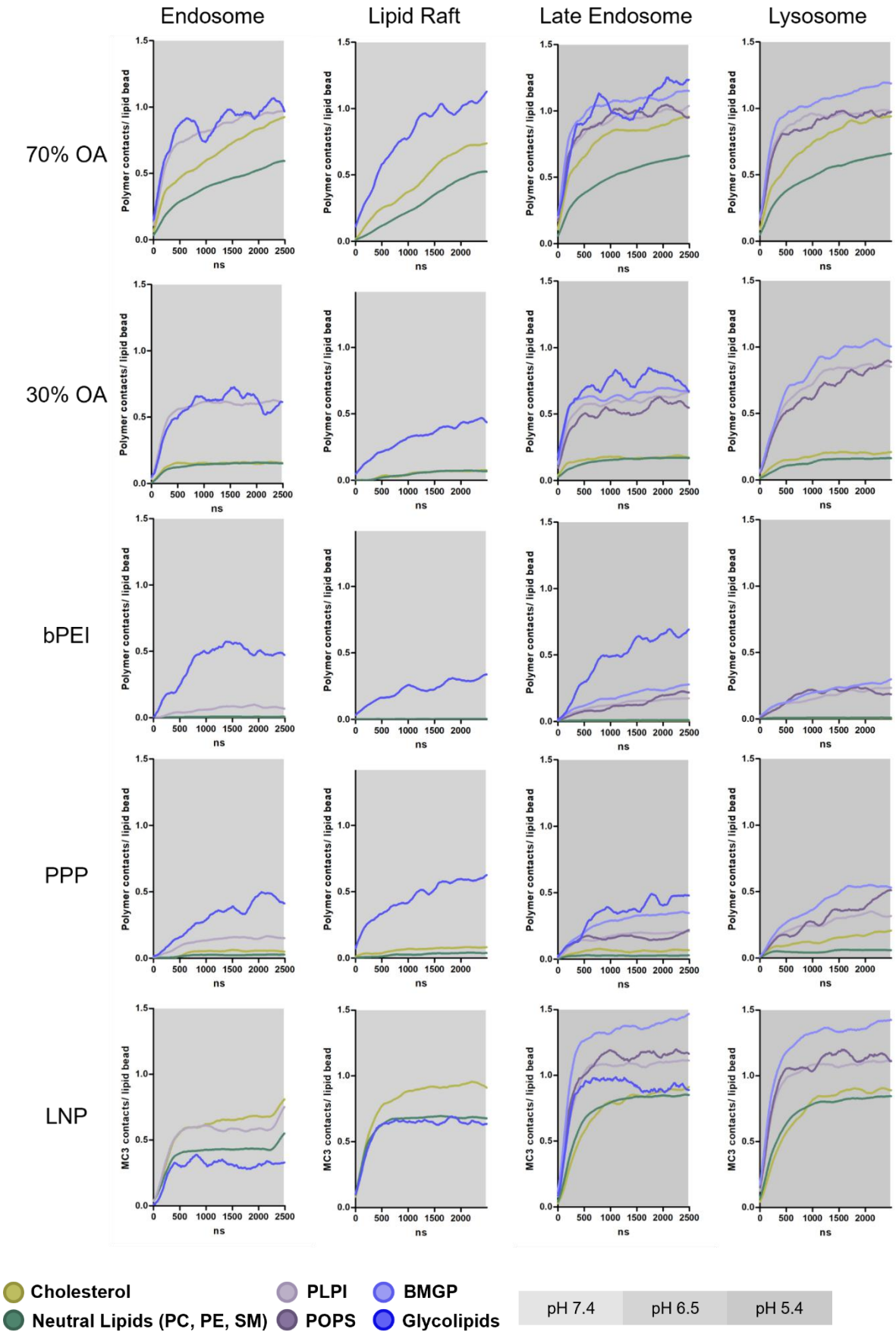

Figure IV.S7. Interaction of nanoparticles and planar membranes at CG resolution: Polymer or MC3 lipid contacts below 0.6 nm per membrane lipid bead over time, n = 3.

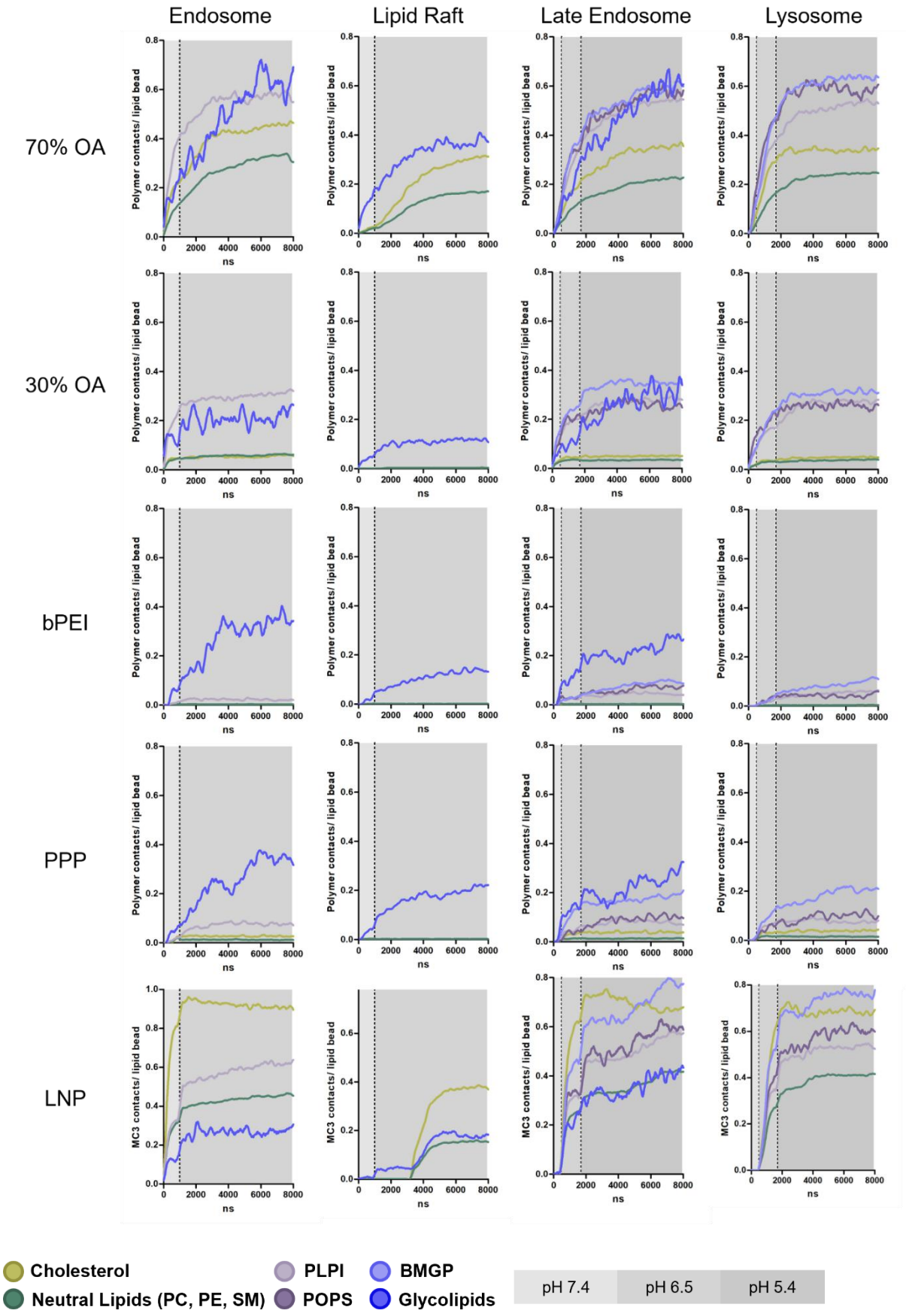

Figure IV.S8. Interaction of nanoparticles and vesicles in CG resolution: Polymer or MC3 lipid contacts below 0.6 nm per membrane lipid bead over time, n = 2.

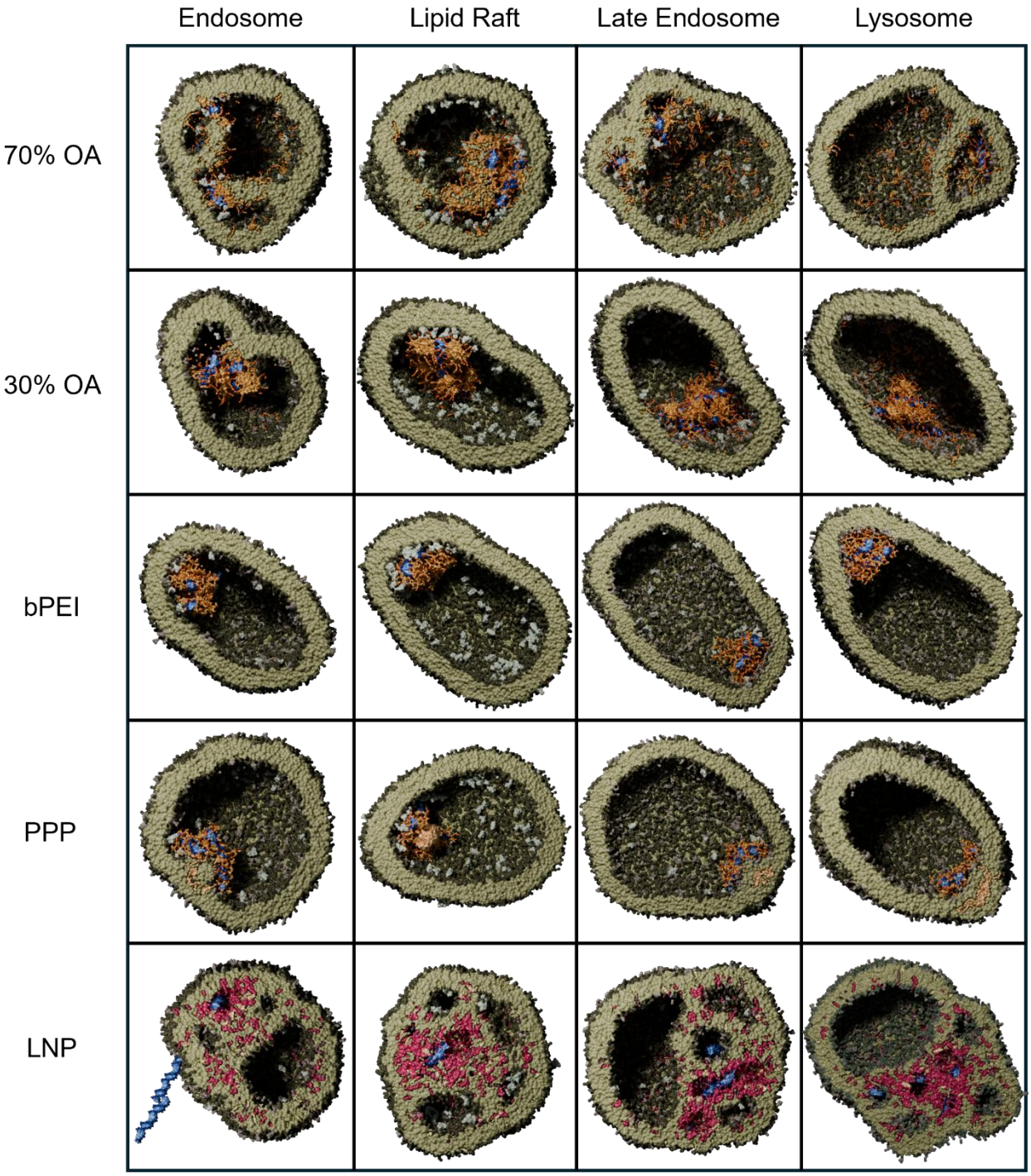

Figure IV.S9. Matrix of the five nanoparticles interacting with the four different vesicles.

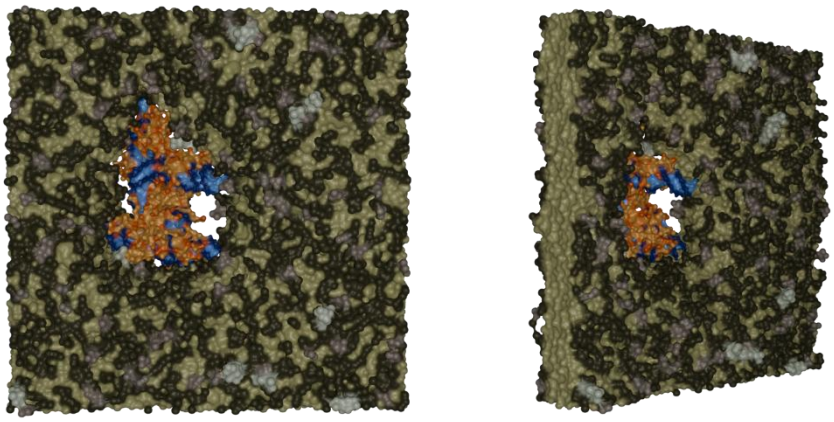

Figure IV.S10. CG simulation of a bPEI polyplex being forcefully pulled through an endosomal membrane.

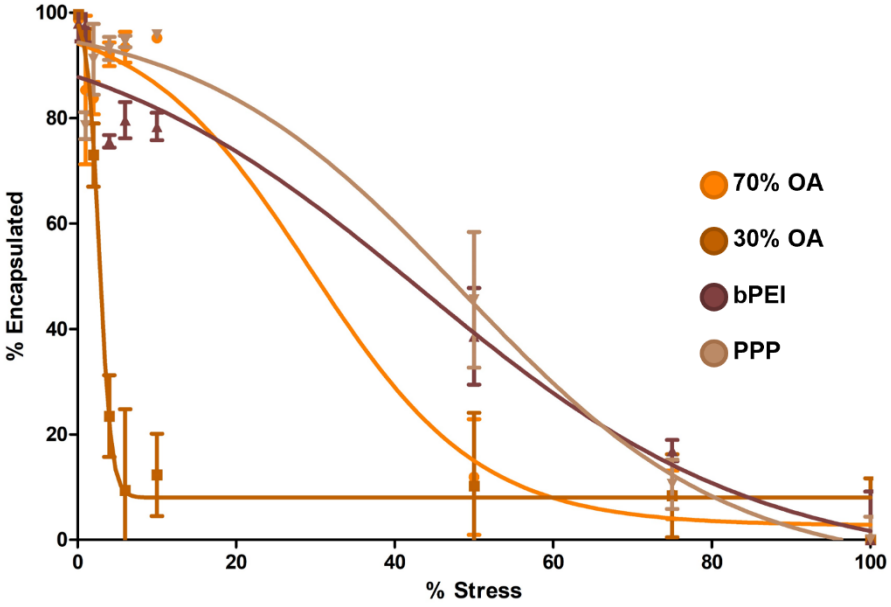

Polymer	EC50	R^2
70% OA PBAE	29.4	0.963
30% OA PBAE	2.75	0.953
bPEI	43.4	0.949
PPP	48.5	0.959

Figure IV.S11. Experimental stability data of the polyplex formulations. % Encapsulated siRNA depending on the concentration (% stress) of the applied heparin/Triton X solution (mean ± sd, n = 3), and sigmoidal fit yielding an EC50 value for each polymer (i.e., the % stress at which 50% of the siRNA is unpacked).

7 Acknowledgments

The authors gratefully acknowledge the Gauss Centre for Supercomputing e.V. (www.gauss centre.eu) for funding this project by providing computing time on the GCS Supercomputer SUPERMUC-NG at Leibniz Supercomputing Centre (www.lrz.de) in the framework of the Project “AVOCADO2”.

Summary and Outlook

Advances in computational power have enabled computational research to take on an increasingly important role in drug development. At the same time, nucleic acid delivery has emerged as one of the most active research fields in pharmaceutical science. This offers the opportunity to combine these two areas and accelerate the design of delivery systems by leveraging computational approaches. With this aim, this work highlighted previous research advances in the field and then developed large-scale MD simulation protocols to showcase how MD can provide meaningful insights into nanoparticle systems.

The applied CG MD approaches reproduced the assembly of PBAE polyplexes in close agreement with experimental observations, as both MD analysis and experiments were designed to allow direct comparison of orthogonal approaches. The main achievements of this chapter demonstrated that hydrodynamic diameters of micelles retrieved from MD were comparable to DLS results. Furthermore, particle morphologies observed in TEM images were validated by MD and vice versa, and the encapsulation of siRNA by polymer, as well as excess polymer, was quantified by MD in good agreement with experiment. Hence, this chapter demonstrates that properly parameterized simulation workflows can capture the essential molecular assembly of complex polyplex formulations.

Beyond polyplex assembly, MD simulations also provided mechanistic insights into nanoparticle–membrane interactions, with the aim of better understanding endosomal escape. The work revealed that hydrophobic moieties in polyplexes play a decisive role in membrane perturbation. Additionally, the contribution of electrostatic interactions, influenced by the composition of both nanoparticles and membranes, was highlighted. This chapter also incorporated a comparison of MD simulation results with *in vitro* data. Although this provided a less direct validation than the experiments described in the previous chapter, the analysis nonetheless offered valuable insights. The correlations observed between simulated behavior and experimental outcomes underline the capacity of MD to capture key aspects of complex biological processes, even when a higher level of abstraction is necessary, such as the exclusion of membrane proteins in the MD setup.

Together, these studies demonstrate how simulation and experiment can complement one another: while experiments provide the essential benchmark for reliability and the real-world framework of application, simulations help to rationalize observed phenomena and reveal underlying mechanisms. In this way, MD can serve both predictive and explanatory roles in the development of nucleic acid delivery systems, ultimately bridging the gap between molecular-scale processes and experimentally measurable outcomes.

The workflows presented herein reproduce experimental findings and offer mechanistic insights, but further validation is required to generalize the correlations across diverse materials and formulations. This will allow us to distinguish which of the presented results are specific to the simulated material (polymer), and which conclusions can be generalized to a broader range of particle formulations. Especially regarding the EE investigations, this will further refine the *in silico – in vitro* correlation and support the establishment of robust predictive models.

Furthermore, MD workflows require a balance between model accuracy and computational efficiency. Larger, more sophisticated models provide detailed, realistic insights. However, once robust correlations between MD simulations and wet-lab experiments have been established and validated across a broader range of systems, it will be desirable to simplify the models while maintaining these correlations. Downsizing and streamlining MD protocols would reduce computational cost and thereby allow their broader and more efficient use in early formulation screening. In the future, this would allow the incorporation of MD simulations as a standard tool in the rational design of delivery platforms, guiding material synthesis and experimental prioritization.

Ultimately, this work underscores the potential of MD simulations not only to deepen our mechanistic understanding of nucleic acid delivery but also to accelerate the development of novel nanoparticle systems.

List of Abbreviations

AA	All Atom
AF647	Alexa Fluor 647
AGO2	Argonaute 2
AIMD	Ab Initio Molecular Dynamics
aMD	accelerated Molecular Dynamics
ApoE	Apolipoprotein E
AUC	Area Under the Curve
BMGP	bis-(monoacylglycero)-phosphate
bPEI	branched Polyethylenimine
CG	Coarse Grained
CMC	Critical Micellar Concentration
CME	Clathrin-Mediated Endocytosis
COM	Center Of Mass
CV	Collective Variable
DFT	Density Functional Theory
DLS	Dynamic Light Scattering
DMEM	Dulbecco’s Modified Eagle Medium
DPG1/3	Glycolip-monosialotetrahexosylgangliosides
DPSM	N-Palmitoyl-D-sphingomyelin
DSPC	1,2-Distearoyl-sn-glycero-3-phosphocholine
EE	Endosomal Escape
eGFP	enhanced Green Fluorescent Protein
FBS	Fetal Bovine Serum
FES	Free Energy Surface
Gal8	Galectin 8
GalNAc	trivalent N- acetylgalactosamine
HBG	HEPES Buffered Glucose
HBS	HEPES Buffered Saline
LDH	Lactate Dehydrogenase
LF	Lipofectamine 2000
LNP	Lipid Nanoparticle
MC3(H)	Dlin-MC3-DMA

MD	Molecular Dynamics
MEM	Minimum Essential Medium Eagle
mRNA	messenger Ribonucleic Acid
Msd	Mean Square Displacement
MW	Molecular Weight
N/P	Amine (N) to Phosphate (P) Ratio
NEAA	Non-Essential Amino Acids
NMR	Nuclear Magnetic Resonance
NOE	Nuclear Overhauser Effect
OA	Oleylamine
PAMAM	Poly(amidoamine)
PBAE	Poly(beta-amino ester)
PBS	Phosphate Buffered Saline
PCL	Polycaprolactone
PDI	Polydispersity Index
pDMAEMA	Poly(2-(N,N-dimethylamino)ethyl methacrylate)
PEG	Poly(ethyleneglycol)
PEI	Polyethyleneimine
PLGA	Poly(lactic acid-*co*-glycolic acid)
PLL	Poly(L-lysine)
PME	Particle Mesh Ewald algorithm
PMF	Potential of Mean Force
POPC	Palmitoyloleoylphosphatidylcholine
POPS	1-Palmitoyl-2-oleoyl-sn-glycero-3-phospho-L-serine
PPP	5 kDa-5 kDa-5 kDa PEI-PCL-PEI polymer
QM	Quantum Mechanical Calculations
RDF	Radial Distribution Function
REMD	Replica Exchange Molecular Dynamics
RISC	RNA Induced Silencing Complex
RNA	Ribonucleic Acid
RNAi	RNA Inteference
SASA	Solvent Accessible Surface Area
SAXS	Small-Angle X-Ray Scattering
SD	Standard Deviation
siGFP	siRNA for the knockdown of eGFP
siNC	negative control siRNA

siRNA	Short interfering Ribonucleic Acid
SORT	Selective ORgan Targeting
TEM	Transmission Electron Microscopy
WHAM	Weighted Histogram Analysis Method

List of publications and conference contributions

1 List of publications

Jonas Binder, Joshua Winkeljann, **Katharina M Steinegger**, Lara Trnovec, Daria Orekhova, Jonas Zähringer, Andreas Hörner, Valentin Fell, Philip Tinnefeld, Benjamin Winkeljann, Wolfgang Frieß, Olivia M Merkel*:
Closing the Gap between Experiment and Simulation─ A Holistic Study on the Complexation of Small Interfering RNAs with Polyethylenimine.
Molecular Pharmaceutics 2024, doi: 10.1021/acs.molpharmaceut.3c00747

Katharina M Steinegger, Lars Allmendinger, Sebastian Sturm, Felix Sieber-Schäfer, Adrian PE Kromer, Knut Müller-Caspary, Benjamin Winkeljann, Olivia M Merkel*:
Molecular Dynamics Simulations Elucidate the Molecular Organization of Poly(beta-amino ester) Based Polyplexes for siRNA Delivery.
Nano Letters 2024, doi: 10.1021/acs.nanolett.4c04291

Joschka T Müller, JT, Adrian PE Kromer, Aysan Ezaddoustdar, Ioannis Alexopoulos, **Katharina M Steinegger**, Diana Leidy Porras-Gonzalez, Otto Berninghausen, Roland Beckmann, Peter Braubach, Gerald Burgstaller, Malgorzata Wygrecka, Olivia M Merkel*:
Nebulization of RNA-Loaded Micelle-Embedded Polyplexes as a Potential Treatment of Idiopathic Pulmonary Fibrosis.
ACS Appl. Mater. Interfaces 2025, doi: 10.1021/acsami.4c21657

Katharina M Steinegger, and Olivia M Merkel*:
How can simulations aid our understanding of nanoparticle-mediated siRNA delivery?
Therapeutic delivery 2025, doi: 10.1080/20415990.2025.2505397

Felix Sieber-Schäfer, Jonas Binder, Tim Münchrath, **Katharina M Steinegger**, Min Jiang, Benjamin Winkeljann, Wolfgang Frieß, Olivia M Merkel*:
From Bits to Bonds - High throughput virtual screening of PBAEs for siRNA delivery using a combinatorial approach of Machine Learning and Molecular Dynamics ***(Under revision)***

Katharina M. Steinegger, Min Jiang, Fabian Link, Benjamin Winkeljann, Olivia M. Merkel*:
Proton sponge or membrane fusion? – Endosomal escape of siRNA polyplexes illuminated by molecular dynamics simulations (***Submitted)***

2 List of conference contributions

Katharina M Steinegger, Jonas Binder, Yao Jin, Benjamin Winkeljann, Olivia M Merkel:
Insight in the Assembly of Nanoparticles consisting of siRNA and a copolymeric PBAE with a Coarse-Grained Molecular Dynamics Model
Poster Presentation at the *CRS Germany Local Chapter Meeting*, 2 – 3 March 2023, Würzburg, Germany

Katharina M Steinegger, Sebastian Sturm, Adrian PE Kromer, Knut Müller-Caspary, Benjamin Winkeljann, Olivia M Merkel:
Characterization of PBAE – siRNA Micelleplex Assembly by Coarse Grained Molecular Dynamics
Poster presentation at the *14th World Meeting on Pharmaceutics, Biopharmaceutics and Pharmaceutical Technology*, 18 – 21 March 2024, Vienna, Austria

Katharina M Steinegger, Min Jiang, Benjamin Winkeljann, Olivia M Merkel:
Proton sponge or membrane fusion? – Endosomal escape of siRNA polyplexes elucidated by molecular dynamics simulations
Oral presentation at the *Controlled Release Society 2025 Annual Meeting & Exposition*, 14 – 18 July 2025, Philadelphia, PA, USA

References

[1] S.M. Hammond, E. Bernstein, D. Beach, G.J. Hannon, An RNA-directed nuclease mediates post-transcriptional gene silencing in Drosophila cells, Nature 404(6775) (2000) 293-6.

[2] A.J. Hamilton, D.C. Baulcombe, A Species of Small Antisense RNA in Posttranscriptional Gene Silencing in Plants, Science 286(5441) (1999) 950-952.

[3] V. Jadhav, A. Vaishnaw, K. Fitzgerald, M.A. Maier, RNA interference in the era of nucleic acid therapeutics, Nature Biotechnology 42(3) (2024) 394-405.

[4] R.F. Ketting, The many faces of RNAi, Dev Cell 20(2) (2011) 148-61.

[5] D.J. Obbard, K.H.J. Gordon, A.H. Buck, F.M. Jiggins, The evolution of RNAi as a defence against viruses and transposable elements, Philosophical Transactions of the Royal Society B: Biological Sciences 364(1513) (2008) 99-115.

[6] S.M. Elbashir, J. Harborth, W. Lendeckel, A. Yalcin, K. Weber, T. Tuschl, Duplexes of 21-nucleotide RNAs mediate RNA interference in cultured mammalian cells, Nature 411(6836) (2001) 494-8.

[7] C. Selvam, D. Mutisya, S. Prakash, K. Ranganna, R. Thilagavathi, Therapeutic potential of chemically modified siRNA: Recent trends, Chemical Biology & Drug Design 90(5) (2017) 665-678.

[8] B.A. Kraynack, B.F. Baker, Small interfering RNAs containing full 2′-O-methylribonucleotide-modified sense strands display Argonaute2/eIF2C2-dependent activity, Rna 12(1) (2006) 163-176.

[9] H. Jahns, M. Roos, J. Imig, F. Baumann, Y. Wang, R. Gilmour, J. Hall, Stereochemical bias introduced during RNA synthesis modulates the activity of phosphorothioate siRNAs, Nat Commun 6 (2015) 6317.

[10] B. Hu, L. Zhong, Y. Weng, L. Peng, Y. Huang, Y. Zhao, X.-J. Liang, Therapeutic siRNA: state of the art, Signal Transduction and Targeted Therapy 5(1) (2020).

[11] S. Gao, F. Dagnaes-Hansen, E.J.B. Nielsen, J. Wengel, F. Besenbacher, K.A. Howard, J. Kjems, The Effect of Chemical Modification and Nanoparticle Formulation on Stability and Biodistribution of siRNA in Mice, Molecular Therapy 17(7) (2009) 1225-1233.

[12] M.E. Davis, J.E. Zuckerman, C.H. Choi, D. Seligson, A. Tolcher, C.A. Alabi, Y. Yen, J.D. Heidel, A. Ribas, Evidence of RNAi in humans from systemically administered siRNA via targeted nanoparticles, Nature 464(7291) (2010) 1067-70.

[13] M. Liu, Y. Wang, Y. Zhang, D. Hu, L. Tang, B. Zhou, L. Yang, Landscape of small nucleic acid therapeutics: moving from the bench to the clinic as next-generation medicines, Signal Transduct Target Ther 10(1) (2025) 73.

[14] A. Lee, Fitusiran: First Approval, Drugs 85(8) (2025) 1073-1077.

[15] S. Matsuda, K. Keiser, J.K. Nair, K. Charisse, R.M. Manoharan, P. Kretschmer, C.G. Peng, A. V. Kel'in, P. Kandasamy, J.L.S. Willoughby, A. Liebow, W. Querbes, K. Yucius, T. Nguyen, S. Milstein, M.A. Maier, K.G. Rajeev, M. Manoharan, siRNA Conjugates Carrying Sequentially Assembled Trivalent N-Acetylgalactosamine Linked Through Nucleosides Elicit Robust Gene Silencing In Vivo in Hepatocytes, ACS Chemical Biology 10(5) (2015) 1181-1187.

[16] J.W. Lee, J. Choi, Y. Choi, K. Kim, Y. Yang, S.H. Kim, H.Y. Yoon, I.C. Kwon, Molecularly engineered siRNA conjugates for tumor-targeted RNAi therapy, J Control Release 351 (2022) 713-726.

[17] M. Moazzam, M. Zhang, A. Hussain, X. Yu, J. Huang, Y. Huang, The landscape of nanoparticle-based siRNA delivery and therapeutic development, Mol Ther 32(2) (2024) 284-312.

[18] H. Park, A. Otte, K. Park, Evolution of drug delivery systems: From 1950 to 2020 and beyond, J Control Release 342 (2022) 53-65.

[19] A.V. Kristen, S. Ajroud-Driss, I. Conceicao, P. Gorevic, T. Kyriakides, L. Obici, Patisiran, an RNAi therapeutic for the treatment of hereditary transthyretin-mediated amyloidosis, Neurodegener Dis Manag 9(1) (2019) 5-23.

[20] U. Kalinke, D.H. Barouch, R. Rizzi, E. Lagkadinou, Ö. Türeci, S. Pather, P. Neels, Clinical development and approval of COVID-19 vaccines, Expert Review of Vaccines 21(5) (2022) 609-619.

[21] C. Hald Albertsen, J.A. Kulkarni, D. Witzigmann, M. Lind, K. Petersson, J.B. Simonsen, The role of lipid components in lipid nanoparticles for vaccines and gene therapy, Advanced Drug Delivery Reviews 188 (2022).

[22] A. Akinc, M.A. Maier, M. Manoharan, K. Fitzgerald, M. Jayaraman, S. Barros, S. Ansell, X. Du, M.J. Hope, T.D. Madden, B.L. Mui, S.C. Semple, Y.K. Tam, M. Ciufolini, D. Witzigmann, J.A. Kulkarni, R. van der Meel, P.R. Cullis, The Onpattro story and the clinical translation of nanomedicines containing nucleic acid-based drugs, Nat Nanotechnol 14(12) (2019) 1084-1087.

[23] A. Vaidya, S. Moore, S. Chatterjee, E. Guerrero, M. Kim, L. Farbiak, S.A. Dilliard, D.J. Siegwart, Expanding RNAi to Kidneys, Lungs, and Spleen via Selective ORgan Targeting (SORT) siRNA Lipid Nanoparticles, Advanced Materials 36(35) (2024).

[24] K.A. Whitehead, J.R. Dorkin, A.J. Vegas, P.H. Chang, O. Veiseh, J. Matthews, O.S. Fenton, Y. Zhang, K.T. Olejnik, V. Yesilyurt, D. Chen, S. Barros, B. Klebanov, T. Novobrantseva, R. Langer, D.G. Anderson, Degradable lipid nanoparticles with predictable in vivo siRNA delivery activity, Nature Communications 5(1) (2014).

[25] A. Abostait, M. Abdelkarim, Z. Bao, Y. Miyake, W.H. Tse, C. Di Ciano-Oliveir, T. Buerki-Thurnherr, C. Allen, R. Keijzer, H.I. Labouta, Optimizing lipid nanoparticles for fetal gene delivery in vitro, ex vivo, and aided with machine learning, Journal of Controlled Release 376 (2024) 678-700.

[26] B. Li, I.O. Raji, A.G.R. Gordon, L. Sun, T.M. Raimondo, F.A. Oladimeji, A.Y. Jiang, A. Varley, R.S. Langer, D.G. Anderson, Accelerating ionizable lipid discovery for mRNA delivery using machine learning and combinatorial chemistry, Nature Materials 23(7) (2024) 1002-1008.

[27] R. Pattipeiluhu, Y. Zeng, M.M.R.M. Hendrix, I.K. Voets, A. Kros, T.H. Sharp, Liquid crystalline inverted lipid phases encapsulating siRNA enhance lipid nanoparticle mediated transfection, Nature Communications 15(1) (2024).

[28] Y. Mo, A.F.A. Keszei, S. Kothari, H. Liu, A. Pan, P. Kim, J. Bu, A. Kamanzi, D.L. Dai, M.T. Mazhab-Jafari, J. Chen, S. Leslie, G. Zheng, Lipid-siRNA Organization Modulates the Intracellular Dynamics of Lipid Nanoparticles, Journal of the American Chemical Society 147(12) (2025) 10430-10445.

[29] M. Hammel, Y. Fan, A. Sarode, A.E. Byrnes, N. Zang, P. Kou, K. Nagapudi, D. Leung, C.C. Hoogenraad, T. Chen, C.-W. Yen, G.L. Hura, Correlating the Structure and Gene Silencing Activity of Oligonucleotide-Loaded Lipid Nanoparticles Using Small-Angle X-ray Scattering, ACS Nano 17(12) (2023) 11454-11465.

[30] S. Omo-Lamai, Y. Wang, M.N. Patel, A. Milosavljevic, D. Zuschlag, S. Poddar, J. Wu, L. Wang, F. Dong, C. Espy, A. Majumder, E.-O. Essien, M. Shen, B. Channer, T.E. Papp, M. Tobin, R. Maheshwari, S. Jeong, S. Patel, A. Shah, S. Murali, L.S. Chase, M.E. Zamora, M.L. Arral, O.A. Marcos-Contreras, J.W. Myerson, C.A. Hunter, D. Discher, P.J. Gaskill, A. Tsourkas, V.R. Muzykantov, I. Brodsky, S. Shin, K.A. Whitehead, H. Parhiz, J. Katzen, J.J. Miner, D. Trauner, J.S. Brenner, Limiting endosomal damage sensing reduces inflammation triggered by lipid nanoparticle endosomal escape, Nature Nanotechnology (2025).

[31] M. Grava, M. Ibrahim, A. Sudarsan, J. Pusterla, J. Philipp, J.O. Radler, N. Schwierz, E. Schneck, Combining molecular dynamics simulations and x-ray scattering techniques for the accurate treatment of protonation degree and packing of ionizable lipids in monolayers, J Chem Phys 159(15) (2023).

[32] M. Ramezanpour, D.P. Tieleman, Computational Insights into the Role of Cholesterol in Inverted Hexagonal Phase Stabilization and Endosomal Drug Release, Langmuir 38(24) (2022) 7462-7471.

[33] J. Philipp, A. Dabkowska, A. Reiser, K. Frank, R. Krzysztoń, C. Brummer, B. Nickel, C.E. Blanchet, A. Sudarsan, M. Ibrahim, S. Johansson, P. Skantze, U. Skantze, S. Östman, M. Johansson, N. Henderson, K. Elvevold, B. Smedsrød, N. Schwierz, L. Lindfors, J.O. Rädler, pH-dependent structural transitions in cationic ionizable lipid mesophases are critical for lipid nanoparticle function, Proceedings of the National Academy of Sciences 120(50) (2023).

[34] A.S. Piotrowski-Daspit, A.C. Kauffman, L.G. Bracaglia, W.M. Saltzman, Polymeric vehicles for nucleic acid delivery, Advanced Drug Delivery Reviews 156 (2020) 119-132.

[35] M. Zheng, G.M. Pavan, M. Neeb, A.K. Schaper, A. Danani, G. Klebe, O.M. Merkel, T. Kissel, Targeting the blind spot of polycationic nanocarrier-based siRNA delivery, ACS Nano 6(11) (2012) 9447-54.

[36] O. Boussif, F. Lezoualc'h, M.A. Zanta, M.D. Mergny, D. Scherman, B. Demeneix, J.P. Behr, A versatile vector for gene and oligonucleotide transfer into cells in culture and in vivo: polyethylenimine, Proc Natl Acad Sci U S A 92(16) (1995) 7297-301.

[37] A. Kargaard, J.P.G. Sluijter, B. Klumperman, Polymeric siRNA gene delivery – transfection efficiency versus cytotoxicity, Journal of Controlled Release 316 (2019) 263-291.

[38] S. Biswas, V. Torchilin, Dendrimers for siRNA Delivery, Pharmaceuticals 6(2) (2013) 161-183.

[39] C. Risnayanti, Y.S. Jang, J. Lee, H.J. Ahn, PLGA nanoparticles co-delivering MDR1 and BCL2 siRNA for overcoming resistance of paclitaxel and cisplatin in recurrent or advanced ovarian cancer, Sci Rep 8(1) (2018) 7498.

[40] M. Breunig, U. Lungwitz, R. Liebl, A. Goepferich, Breaking up the correlation between efficacy and toxicity for nonviral gene delivery, Proceedings of the National Academy of Sciences 104(36) (2007) 14454-14459.

[41] J.S. Suk, Q. Xu, N. Kim, J. Hanes, L.M. Ensign, PEGylation as a strategy for improving nanoparticle-based drug and gene delivery, Advanced Drug Delivery Reviews 99 (2016) 28-51.

[42] A. Beyerle, O. Merkel, T. Stoeger, T. Kissel, PEGylation affects cytotoxicity and cell-compatibility of poly(ethylene imine) for lung application: structure-function relationships, Toxicol Appl Pharmacol 242(2) (2010) 146-54.

[43] M.K. Grun, A. Suberi, K. Shin, T. Lee, V. Gomerdinger, Z.M. Moscato, A.S. Piotrowski-Daspit, W.M. Saltzman, PEGylation of poly(amine-co-ester) polyplexes for tunable gene delivery, Biomaterials 272 (2021).

[44] C.E. Nelson, J.R. Kintzing, A. Hanna, J.M. Shannon, M.K. Gupta, C.L. Duvall, Balancing cationic and hydrophobic content of PEGylated siRNA polyplexes enhances endosome escape, stability, blood circulation time, and bioactivity in vivo, ACS Nano 7(10) (2013) 8870-80.

[45] T.A. Werfel, M.A. Jackson, T.E. Kavanaugh, K.C. Kirkbride, M. Miteva, T.D. Giorgio, C. Duvall, Combinatorial optimization of PEG architecture and hydrophobic content improves ternary siRNA polyplex stability, pharmacokinetics, and potency in vivo, Journal of Controlled Release 255 (2017) 12-26.

[46] P.Y. Teo, C. Yang, J.L. Hedrick, A.C. Engler, D.J. Coady, S. Ghaem-Maghami, A.J.T. George, Y.Y. Yang, Hydrophobic modification of low molecular weight polyethylenimine for improved gene transfection, Biomaterials 34(32) (2013) 7971-7979.

[47] A.S. Ansari, R. K.C, L.C. Morales, M. Nasrullah, D.N. Meenakshi Sundaram, C. Kucharski, X. Jiang, J. Brandwein, H. Uludağ, Lipopolymer mediated siRNA delivery targeting aberrant oncogenes for effective therapy of myeloid leukemia in preclinical animal models, Journal of Controlled Release 367 (2024) 821-836.

[48] B. Winkeljann, D.C. Keul, O.M. Merkel, Engineering poly- and micelleplexes for nucleic acid delivery - A reflection on their endosomal escape, J Control Release 353 (2022) 518-534.

[49] W. Wang, M. Balk, Z. Deng, C. Wischke, M. Gossen, M. Behl, N. Ma, A. Lendlein, Engineering biodegradable micelles of polyethylenimine-based amphiphilic block copolymers for efficient DNA and siRNA delivery, Journal of Controlled Release 242 (2016) 71-79.

[50] G. Sinani, M.E. Durgun, E. Cevher, Y. Özsoy, Polymeric-Micelle-Based Delivery Systems for Nucleic Acids, Pharmaceutics 15(8) (2023).

[51] C.J. Grimme, M.G. Hanson, L.G. Corcoran, T.M. Reineke, Polycation Architecture Affects Complexation and Delivery of Short Antisense Oligonucleotides: Micelleplexes Outperform Polyplexes, Biomacromolecules 23(8) (2022) 3257-3271.

[52] J.J. Green, G.T. Zugates, R. Langer, D.G. Anderson, Poly(beta-amino esters): procedures for synthesis and gene delivery, Methods Mol Biol 480 (2009) 53-63.

[53] Y. Rui, D.R. Wilson, S.Y. Tzeng, H.M. Yamagata, D. Sudhakar, M. Conge, C.A. Berlinicke, D.J. Zack, A. Tuesca, J.J. Green, High-throughput and high-content bioassay enables tuning of polyester nanoparticles for cellular uptake, endosomal escape, and systemic in vivo delivery of mRNA, Sci Adv 8(1) (2022) eabk2855.

[54] J.T. Müller, A.P.E. Kromer, A. Ezaddoustdar, I. Alexopoulos, K.M. Steinegger, D.L. Porras-Gonzalez, O. Berninghausen, R. Beckmann, P. Braubach, G. Burgstaller, M. Wygrecka, O.M. Merkel, Nebulization of RNA-Loaded Micelle-Embedded Polyplexes as a Potential Treatment of Idiopathic Pulmonary Fibrosis, ACS Applied Materials & Interfaces 17(8) (2025) 11861-11872.

[55] A.P.E. Kromer, F. Sieber-Schafer, J. Farfan Benito, O.M. Merkel, Design of Experiments Grants Mechanistic Insights into the Synthesis of Spermine-Containing PBAE Copolymers, ACS Appl Mater Interfaces (2024).

[56] S. Panico, S. Capolla, S. Bozzer, G. Toffoli, M. Dal Bo, P. Macor, Biological Features of Nanoparticles: Protein Corona Formation and Interaction with the Immune System, Pharmaceutics 14(12) (2022).

[57] W. Dong, J. Ye, J. Zhou, W. Wang, H. Wang, X. Zheng, Y. Yang, X. Xia, Y. Liu, Comparative study of mucoadhesive and mucus-penetrative nanoparticles based on phospholipid complex to overcome the mucus barrier for inhaled delivery of baicalein, Acta Pharmaceutica Sinica B 10(8) (2020) 1576-1585.

[58] Z. Zhao, A. Ukidve, J. Kim, S. Mitragotri, Targeting Strategies for Tissue-Specific Drug Delivery, Cell 181(1) (2020) 151-167.

[59] I. Rivolta, Panariti, Miserocchi, The effect of nanoparticle uptake on cellular behavior: disrupting or enabling functions?, Nanotechnology, Science and Applications (2012).

[60] S. Tortorella, T.C. Karagiannis, Transferrin Receptor-Mediated Endocytosis: A Useful Target for Cancer Therapy, The Journal of Membrane Biology 247(4) (2014) 291-307.

[61] M.M. Islam, I. Hlushchenko, S.G. Pfisterer, Low-Density Lipoprotein Internalization, Degradation and Receptor Recycling Along Membrane Contact Sites, Frontiers in Cell and Developmental Biology 10 (2022).

[62] M. Sousa de Almeida, E. Susnik, B. Drasler, P. Taladriz-Blanco, A. Petri-Fink, B. Rothen-Rutishauser, Understanding nanoparticle endocytosis to improve targeting strategies in nanomedicine, Chemical Society Reviews 50(9) (2021) 5397-5434.

[63] S. Behzadi, V. Serpooshan, W. Tao, M.A. Hamaly, M.Y. Alkawareek, E.C. Dreaden, D. Brown, A.M. Alkilany, O.C. Farokhzad, M. Mahmoudi, Cellular uptake of nanoparticles: journey inside the cell, Chemical Society Reviews 46(14) (2017) 4218-4244.

[64] X. Xie, J. Liao, X. Shao, Q. Li, Y. Lin, The Effect of shape on Cellular Uptake of Gold Nanoparticles in the forms of Stars, Rods, and Triangles, Scientific Reports 7(1) (2017).

[65] X. Cheng, X. Tian, A. Wu, J. Li, J. Tian, Y. Chong, Z. Chai, Y. Zhao, C. Chen, C. Ge, Protein Corona Influences Cellular Uptake of Gold Nanoparticles by Phagocytic and Nonphagocytic Cells in a Size-Dependent Manner, ACS Applied Materials & Interfaces 7(37) (2015) 20568-20575.

[66] A. Spadea, M. Jackman, L. Cui, S. Pereira, M.J. Lawrence, R.A. Campbell, M. Ashford, Nucleic Acid-Loaded Lipid Nanoparticle Interactions with Model Endosomal Membranes, ACS Applied Materials & Interfaces 14(26) (2022) 30371-30384.

[67] L.M.P. Vermeulen, S.C. De Smedt, K. Remaut, K. Braeckmans, The proton sponge hypothesis: Fable or fact?, Eur J Pharm Biopharm 129 (2018) 184-190.

[68] D. Yan, Y. Ma, X. Chen, S. Deng, Q. Wang, Molecular dynamics-driven drug discovery, Physical Chemistry Chemical Physics 27(24) (2025) 12633-12651.

[69] Q. Zhao, N. Miriyala, Y. Su, W. Chen, X. Gao, L. Shao, R. Yan, H. Li, X. Yao, D. Cao, Y. Wang, D. Ouyang, Computer-Aided Formulation Design for a Highly Soluble Lutein–Cyclodextrin Multiple-Component Delivery System, Molecular Pharmaceutics 15(4) (2018) 1664-1673.

[70] A. Pandya, C. Zhang, T.S. Barata, S. Brocchini, M.J. Howard, M. Zloh, P.A. Dalby, Molecular Dynamics Simulations Reveal How Competing Protein–Surface Interactions for Glycine, Citrate, and Water Modulate Stability in Antibody Fragment Formulations, Molecular Pharmaceutics 21(11) (2024) 5497-5509.

[71] B.M. Bruininks, P.C. Souza, H. Ingolfsson, S.J. Marrink, A molecular view on the escape of lipoplexed DNA from the endosome, Elife 9 (2020).

[72] Z. Zhang, D. Cheng, W. Luo, D. Hu, T. Yang, K. Hu, L. Liang, W. Liu, J. Hu, Molecular Dynamics Simulation of Lipid Nanoparticles Encapsulating mRNA, Molecules 29(18) (2024).

[73] A. Bunker, T. Róg, Mechanistic Understanding From Molecular Dynamics Simulation in Pharmaceutical Research 1: Drug Delivery, Frontiers in Molecular Biosciences 7 (2020).

[74] M.A. González, Force fields and molecular dynamics simulations, École thématique de la Société Française de la Neutronique 12 (2011) 169-200.

[75] C. Ringrose, J.T. Horton, L.-P. Wang, D.J. Cole, Exploration and validation of force field design protocols through QM-to-MM mapping, Physical Chemistry Chemical Physics 24(28) (2022) 17014-17027.

[76] P.E.M. Lopes, O. Guvench, A.D. MacKerell, Current Status of Protein Force Fields for Molecular Dynamics Simulations, Molecular Modeling of Proteins2015, pp. 47-71.

[77] K. Vanommeslaeghe, A.D. MacKerell, CHARMM additive and polarizable force fields for biophysics and computer-aided drug design, Biochimica et Biophysica Acta (BBA) - General Subjects 1850(5) (2015) 861-871.

[78] A.N. Leonard, A.C. Simmonett, F.C. Pickard, J. Huang, R.M. Venable, J.B. Klauda, B.R. Brooks, R.W. Pastor, Comparison of Additive and Polarizable Models with Explicit Treatment of Long-Range Lennard-Jones Interactions Using Alkane Simulations, Journal of Chemical Theory and Computation 14(2) (2018) 948-958.

[79] L. Wang, M. Schauperl, D.L. Mobley, C. Bayly, M.K. Gilson, A Fast, Convenient, Polarizable Electrostatic Model for Molecular Dynamics, Journal of Chemical Theory and Computation 20(3) (2024) 1293-1305.

[80] A. Wacha, Z. Varga, T. Beke-Somfai, Comparative Study of Molecular Mechanics Force Fields for β-Peptidic Foldamers: Folding and Self-Association, Journal of Chemical Information and Modeling 63(12) (2023) 3799-3813.

[81] M. Javanainen, P. Heftberger, J.J. Madsen, M.S. Miettinen, G. Pabst, O.H.S. Ollila, Quantitative Comparison against Experiments Reveals Imperfections in Force Fields' Descriptions of POPC–Cholesterol Interactions, Journal of Chemical Theory and Computation 19(18) (2023) 6342-6352.

[82] M. Domanska, P. Setny, Exploring the Properties of Curved Lipid Membranes: Comparative Analysis of Atomistic and Coarse-Grained Force Fields, The Journal of Physical Chemistry B 128(29) (2024) 7160-7171.

[83] S.J. Marrink, V. Corradi, P.C.T. Souza, H.I. Ingólfsson, D.P. Tieleman, M.S.P. Sansom, Computational Modeling of Realistic Cell Membranes, Chemical Reviews 119(9) (2019) 6184-6226.

[84] S.A. Hollingsworth, R.O. Dror, Molecular Dynamics Simulation for All, Neuron 99(6) (2018) 1129-1143.

[85] L. Casalino, A.C. Dommer, Z. Gaieb, E.P. Barros, T. Sztain, S.-H. Ahn, A. Trifan, A. Brace, A.T. Bogetti, A. Clyde, H. Ma, H. Lee, M. Turilli, S. Khalid, L.T. Chong, C. Simmerling, D.J. Hardy, J.D.C. Maia, J.C. Phillips, T. Kurth, A.C. Stern, L. Huang, J.D. McCalpin, M. Tatineni, T. Gibbs, J.E. Stone, S. Jha, A. Ramanathan, R.E. Amaro, AI-driven multiscale simulations illuminate mechanisms of SARS-CoV-2 spike dynamics, The International Journal of High Performance Computing Applications 35(5) (2021) 432-451.

[86] K. Sarthak, D. Winogradoff, Y. Ge, S. Myong, A. Aksimentiev, Benchmarking Molecular Dynamics Force Fields for All-Atom Simulations of Biological Condensates, Journal of Chemical Theory and Computation 19(12) (2023) 3721-3740.

[87] D. Chmielewski, E.A. Wilson, G. Pintilie, P. Zhao, M. Chen, M.F. Schmid, G. Simmons, L. Wells, J. Jin, A. Singharoy, W. Chiu, Structural insights into the modulation of coronavirus spike tilting and infectivity by hinge glycans, Nature Communications 14(1) (2023).

[88] X.-L. Li, Z.-S. Yan, Y.-Q. Ma, H.-M. Ding, Impact of Glycosylation of Apolipoprotein D on Its Interaction with Gold Nanoparticles: Insights from Molecular Dynamics Simulations, ACS Applied Materials & Interfaces 17(3) (2025) 4490-4501.

[89] J.A. Maier, C. Martinez, K. Kasavajhala, L. Wickstrom, K.E. Hauser, C. Simmerling, ff14SB: Improving the Accuracy of Protein Side Chain and Backbone Parameters from ff99SB, Journal of Chemical Theory and Computation 11(8) (2015) 3696-3713.

[90] I. Ivani, P.D. Dans, A. Noy, A. Pérez, I. Faustino, A. Hospital, J. Walther, P. Andrio, R. Goñi, A. Balaceanu, G. Portella, F. Battistini, J.L. Gelpí, C. González, M. Vendruscolo, C.A. Laughton, S.A. Harris, D.A. Case, M. Orozco, Parmbsc1: a refined force field for DNA simulations, Nature Methods 13(1) (2015) 55-58.

[91] C.J. Dickson, B.D. Madej, Å.A. Skjevik, R.M. Betz, K. Teigen, I.R. Gould, R.C. Walker, Lipid14: The Amber Lipid Force Field, Journal of Chemical Theory and Computation 10(2) (2014) 865-879.

[92] R.B. Best, X. Zhu, J. Shim, P.E.M. Lopes, J. Mittal, M. Feig, A.D. MacKerell, Optimization of the Additive CHARMM All-Atom Protein Force Field Targeting Improved Sampling of the Backbone ϕ, ψ and Side-Chain χ1 and χ2 Dihedral Angles, Journal of Chemical Theory and Computation 8(9) (2012) 3257-3273.

[93] E. Balduzzi, W. Yin, J.C. Lambry, H. Myllykallio, A. Aleksandrov, Additive CHARMM Force Field for Pterins and Folates, Journal of Computational Chemistry 46(1) (2024).

[94] A. Croitoru, S.-J. Park, A. Kumar, J. Lee, W. Im, A.D. MacKerell, A. Aleksandrov, Additive CHARMM36 Force Field for Nonstandard Amino Acids, Journal of Chemical Theory and Computation 17(6) (2021) 3554-3570.

[95] A. Croitoru, A. Kumar, J.-C. Lambry, J. Lee, S. Sharif, W. Yu, A.D. MacKerell, A. Aleksandrov, Increasing the Accuracy and Robustness of the CHARMM General Force Field with an Expanded Training Set, Journal of Chemical Theory and Computation 21(6) (2025) 3044-3065.

[96] W.L. Jorgensen, D.S. Maxwell, J. Tirado-Rives, Development and Testing of the OPLS All-Atom Force Field on Conformational Energetics and Properties of Organic Liquids, Journal of the American Chemical Society 118(45) (1996) 11225-11236.

[97] P.C.T. Souza, R. Alessandri, J. Barnoud, S. Thallmair, I. Faustino, F. Grunewald, I. Patmanidis, H. Abdizadeh, B.M.H. Bruininks, T.A. Wassenaar, P.C. Kroon, J. Melcr, V. Nieto, V. Corradi, H.M. Khan, J. Domanski, M. Javanainen, H. Martinez-Seara, N. Reuter, R.B. Best, I. Vattulainen, L. Monticelli, X. Periole, D.P. Tieleman, A.H. de Vries, S.J. Marrink, Martini 3: a general purpose force field for coarse-grained molecular dynamics, Nat Methods 18(4) (2021) 382-388.

[98] A. Emperador, E. Guàrdia, Accurate coarse grained models for protein association and recognition, Protein Aggregation - Part A2025, pp. 1-21.

[99] A. Bunker, A. Magarkar, T. Viitala, Rational design of liposomal drug delivery systems, a review: Combined experimental and computational studies of lipid membranes, liposomes and their PEGylation, Biochimica et Biophysica Acta (BBA) - Biomembranes 1858(10) (2016) 2334-2352.

[100] J.A. Stevens, F. Grunewald, P.A.M. van Tilburg, M. Konig, B.R. Gilbert, T.A. Brier, Z.R. Thornburg, Z. Luthey-Schulten, S.J. Marrink, Molecular dynamics simulation of an entire cell, Front Chem 11 (2023) 1106495.

[101] A. Bartocci, A. Grazzi, N. Awad, P.-J. Corringer, P.C.T. Souza, M. Cecchini, A millisecond coarse-grained simulation approach to decipher allosteric cannabinoid binding at the glycine receptor α1, Nature Communications 15(1) (2024).

[102] S.J. Marrink, H.J. Risselada, S. Yefimov, D.P. Tieleman, A.H. de Vries, The MARTINI Force Field: Coarse Grained Model for Biomolecular Simulations, The Journal of Physical Chemistry B 111(27) (2007) 7812-7824.

[103] E. Papaleo, M. Javanainen, H. Martinez-Seara, I. Vattulainen, Excessive aggregation of membrane proteins in the Martini model, Plos One 12(11) (2017).

[104] S.J. Marrink, L. Monticelli, M.N. Melo, R. Alessandri, D.P. Tieleman, P.C.T. Souza, Two decades of Martini: Better beads, broader scope, WIREs Computational Molecular Science 13(1) (2022).

[105] K.B. Pedersen, H.I. Ingólfsson, D.P. Ramirez-Echemendia, L. Borges-Araújo, M.D. Andreasen, C. Empereur-mot, J. Melcr, T.N. Ozturk, W.F.D. Bennett, L.R. Kjølbye, C. Brasnett, V. Corradi, H.M. Khan, E.A. Cino, J. Crowley, H. Kim, B. Fábián, A.C. Borges-Araújo, G.M. Pavan, G. Launay, F. Lolicato, T.A. Wassenaar, M.N. Melo, S. Thallmair, T.S. Carpenter, L. Monticelli, D.P. Tieleman, B. Schiøtt, P.C.T. Souza, S.J. Marrink, The Martini 3 Lipidome: Expanded and Refined Parameters Improve Lipid Phase Behavior, ACS Central Science (2025).

[106] F. Grunewald, M.H. Punt, E.E. Jefferys, P.A. Vainikka, M. Konig, V. Virtanen, T.A. Meyer, W. Pezeshkian, A.J. Gormley, M. Karonen, M.S.P. Sansom, P.C.T. Souza, S.J. Marrink, Martini 3 Coarse-Grained Force Field for Carbohydrates, J Chem Theory Comput 18(12) (2022) 7555-7569.

[107] L. Borges-Araújo, A.C. Borges-Araújo, T.N. Ozturk, D.P. Ramirez-Echemendia, B. Fábián, T.S. Carpenter, S. Thallmair, J. Barnoud, H.I. Ingólfsson, G. Hummer, D.P. Tieleman, S.J. Marrink, P.C.T. Souza, M.N. Melo, Martini 3 Coarse-Grained Force Field for Cholesterol, Journal of Chemical Theory and Computation 19(20) (2023) 7387-7404.

[108] P.C.e.a. Kroon, Martinize2 and Vermouth: Unified Framework for Topology Generation, (2022).

[109] L.R. Kjølbye, M. Valério, M. Paloncýová, L. Borges-Araújo, R. Pestana-Nobles, F. Grünewald, B. M. H. Bruininks, R. Araya-Osorio, M. Šrejber, R. Mera-Adasme, L. Monticelli, S. J. Marrink, M. Otyepka, S. Wu, P. C.T. Souza, Martini 3 building blocks for Lipid Nanoparticle design, ChemRxiv (2025).

[110] Y. Cao, J. Zhu, J. Kou, D.P. Tieleman, Q. Liang, Unveiling Interactions of Tumor-Targeting Nanoparticles with Lipid Bilayers Using a Titratable Martini Model, J Chem Theory Comput 20(9) (2024) 4045-4053.

[111] D.N. Zimmer, F. Schmid, G. Settanni, Ionizable Cationic Lipids and Helper Lipids Synergistically Contribute to RNA Packing and Protection in Lipid-Based Nanomaterials, J Phys Chem B 128(41) (2024) 10165-10177.

[112] L. Borges-Araújo, G.P. Pereira, M. Valério, P.C.T. Souza, Assessing the Martini 3 protein model: A review of its path and potential, Biochimica et Biophysica Acta (BBA) - Proteins and Proteomics 1872(4) (2024).

[113] J. Binder, M. Zalar, M. Huelsmeyer, M. Siedler, R. Curtis, W. Friess, Enhancing Martini 3 for protein self-interaction simulations, European Journal of Pharmaceutical Sciences 209 (2025).

[114] L. Wang, C. Brasnett, L. Borges-Araújo, P.C.T. Souza, S.J. Marrink, Martini3-IDP: improved Martini 3 force field for disordered proteins, Nature Communications 16(1) (2025).

[115] G.M. Torrie, J.P. Valleau, Nonphysical sampling distributions in Monte Carlo free-energy estimation: Umbrella sampling, Journal of Computational Physics 23(2) (1977) 187-199.

[116] J.S. Hub, B.L. de Groot, D. van der Spoel, g_wham—A Free Weighted Histogram Analysis Implementation Including Robust Error and Autocorrelation Estimates, Journal of Chemical Theory and Computation 6(12) (2010) 3713-3720.

[117] A. Laio, M. Parrinello, Escaping free-energy minima, Proceedings of the National Academy of Sciences 99(20) (2002) 12562-12566.

[118] L.C.T. Pierce, R. Salomon-Ferrer, C. Augusto F. de Oliveira, J.A. McCammon, R.C. Walker, Routine Access to Millisecond Time Scale Events with Accelerated Molecular Dynamics, Journal of Chemical Theory and Computation 8(9) (2012) 2997-3002.

[119] L.S. Stelzl, G. Hummer, Kinetics from Replica Exchange Molecular Dynamics Simulations, Journal of Chemical Theory and Computation 13(8) (2017) 3927-3935.

[120] R. Iftimie, P. Minary, M.E. Tuckerman, Ab initio

molecular dynamics: Concepts, recent developments, and future trends, Proceedings of the National Academy of Sciences 102(19) (2005) 6654-6659.

[121] Y.-B. Zhuang, C. Liu, J.-X. Zhu, J.-Y. Hu, J.-B. Le, J.-Q. Li, X.-J. Wen, X.-T. Fan, M. Jia, X.-Y. Li, A. Chen, L. Li, Z.-L. Lin, W.-H. Xu, J. Cheng, An artificial intelligence accelerated ab initio molecular dynamics dataset for electrochemical interfaces, Scientific Data 12(1) (2025).

[122] G. Groenhof, Introduction to QM/MM Simulations, Biomolecular Simulations2013, pp. 43-66.

[123] P. Cechova, M. Paloncyova, M. Srejber, M. Otyepka, Mechanistic insights into interactions between ionizable lipid nanodroplets and biomembranes, J Biomol Struct Dyn (2024) 1-11.

[124] J.V. Vermaas, C.G. Mayne, E. Shinn, E. Tajkhorshid, Assembly and Analysis of Cell-Scale Membrane Envelopes, J Chem Inf Model 62(3) (2022) 602-617.

[125] L.T. Chong, A.S. Saglam, D.M. Zuckerman, Path-sampling strategies for simulating rare events in biomolecular systems, Current Opinion in Structural Biology 43 (2017) 88-94.

[126] S. Sinha, B. Tam, S.M. Wang, Applications of Molecular Dynamics Simulation in Protein Study, Membranes (Basel) 12(9) (2022).

[127] G.M. Pavan, L. Albertazzi, A. Danani, Ability to adapt: different generations of PAMAM dendrimers show different behaviors in binding siRNA, J Phys Chem B 114(8) (2010) 2667-75.

[128] G. Grasso, M.A. Deriu, V. Patrulea, G. Borchard, M. Moller, A. Danani, Free energy landscape of siRNA-polycation complexation: Elucidating the effect of molecular geometry, polymer flexibility, and charge neutralization, PLoS One 12(10) (2017) e0186816.

[129] X. Zhao, Q. Xu, Q. Wang, X. Liang, J. Wang, H. Jin, Y. Man, D. Guo, F. Gao, X. Tang, Induced Self-Assembly of Vitamin E-Spermine/siRNA Nanocomplexes via Spermine/Helix Groove-Specific Interaction for Efficient siRNA Delivery and Antitumor Therapy, Adv Healthc Mater (2024) e2303186.

[130] D. Meneksedag-Erol, R.B. Kc, T. Tang, H. Uludağ, A Delicate Balance When Substituting a Small Hydrophobe onto Low Molecular Weight Polyethylenimine to Improve Its Nucleic Acid Delivery Efficiency, ACS Applied Materials & Interfaces 7(44) (2015) 24822-24832.

[131] S. Dehghani-Ghahnaviyeh, M. Smith, Y. Xia, A. Dousis, A. Grossfield, S. Sur, Ionizable Amino Lipids Distribution and Effects on DSPC/Cholesterol Membranes: Implications for Lipid Nanoparticle Structure, J Phys Chem B 127(31) (2023) 6928-6939.

[132] M. Ibrahim, J. Gilbert, M. Heinz, T. Nylander, N. Schwierz, Structural insights on ionizable Dlin-MC3-DMA lipids in DOPC layers by combining accurate atomistic force fields, molecular dynamics simulations and neutron reflectivity, Nanoscale 15(27) (2023) 11647-11656.

[133] J. Binder, J. Winkeljann, K. Steinegger, L. Trnovec, D. Orekhova, J. Zahringer, A. Horner, V. Fell, P. Tinnefeld, B. Winkeljann, W. Friess, O.M. Merkel, Closing the Gap between Experiment and Simulation: A Holistic Study on the Complexation of Small Interfering RNAs with Polyethylenimine, Mol Pharm 21(5) (2024) 2163-2175.

[134] K.M. Steinegger, L. Allmendinger, S. Sturm, F. Sieber-Schafer, A.P.E. Kromer, K. Muller-Caspary, B. Winkeljann, O.M. Merkel, Molecular Dynamics Simulations Elucidate the Molecular Organization of Poly(beta-amino ester) Based Polyplexes for siRNA Delivery, Nano Lett (2024).

[135] M. Paloncyova, M. Srejber, P. Cechova, P. Kuhrova, F. Zaoral, M. Otyepka, Atomistic Insights into Organization of RNA-Loaded Lipid Nanoparticles, J Phys Chem B 127(5) (2023) 1158-1166.

[136] K.V. Kilchrist, S.C. Dimobi, M.A. Jackson, B.C. Evans, T.A. Werfel, E.A. Dailing, S.K. Bedingfield, I.B. Kelly, C.L. Duvall, Gal8 Visualization of Endosome Disruption Predicts Carrier-Mediated Biologic Drug Intracellular Bioavailability, ACS Nano 13(2) (2019) 1136-1152.

[137] T.A. Wassenaar, H.I. Ingolfsson, R.A. Bockmann, D.P. Tieleman, S.J. Marrink, Computational Lipidomics with insane: A Versatile Tool for Generating Custom Membranes for Molecular Simulations, J Chem Theory Comput 11(5) (2015) 2144-55.

[138] S. Feng, S. Park, Y.K. Choi, W. Im, CHARMM-GUI Membrane Builder: Past, Current, and Future Developments and Applications, J Chem Theory Comput 19(8) (2023) 2161-2185.

[139] G.M. Traber, A.M. Yu, RNAi-Based Therapeutics and Novel RNA Bioengineering Technologies, J Pharmacol Exp Ther 384(1) (2023) 133-154.

[140] M. Balwani, E. Sardh, P. Ventura, P.A. Peiro, D.C. Rees, U. Stolzel, D.M. Bissell, H.L. Bonkovsky, J. Windyga, K.E. Anderson, C. Parker, S.M. Silver, S.B. Keel, J.D. Wang, P.E. Stein, P. Harper, D. Vassiliou, B. Wang, J. Phillips, A. Ivanova, J.G. Langendonk, R. Kauppinen, E. Minder, Y. Horie, C. Penz, J. Chen, S. Liu, J.J. Ko, M.T. Sweetser, P. Garg, A. Vaishnaw, J.B. Kim, A.R. Simon, L. Gouya, E. Investigators, Phase 3 Trial of RNAi Therapeutic Givosiran for Acute Intermittent Porphyria, N Engl J Med 382(24) (2020) 2289-2301.

[141] S.F. Garrelfs, Y. Frishberg, S.A. Hulton, M.J. Koren, W.D. O'Riordan, P. Cochat, G. Deschenes, H. Shasha-Lavsky, J.M. Saland, W.G. Van't Hoff, D.G. Fuster, D. Magen, S.H. Moochhala, G. Schalk, E. Simkova, J.W. Groothoff, D.J. Sas, K.A. Meliambro, J. Lu, M.T. Sweetser, P.P. Garg, A.K. Vaishnaw, J.M. Gansner, T.L. McGregor, J.C. Lieske, I.-A. Collaborators, Lumasiran, an RNAi Therapeutic for Primary Hyperoxaluria Type 1, N Engl J Med 384(13) (2021) 1216-1226.

[142] K.K. Ray, R.S. Wright, D. Kallend, W. Koenig, L.A. Leiter, F.J. Raal, J.A. Bisch, T. Richardson, M. Jaros, P.L.J. Wijngaard, J.J.P. Kastelein, Orion, O.-. Investigators, Two Phase 3 Trials of Inclisiran in Patients with Elevated LDL Cholesterol, N Engl J Med 382(16) (2020) 1507-1519.

[143] J. Belgrad, H.H. Fakih, A. Khvorova, Nucleic Acid Therapeutics: Successes, Milestones, and Upcoming Innovation, Nucleic Acid Ther 34(2) (2024) 52-72.

[144] E.W. Kavanagh, J.J. Green, Toward Gene Transfer Nanoparticles as Therapeutics, Adv Healthc Mater 11(7) (2022) e2102145.

[145] O.M. Merkel, T. Kissel, Quo vadis polyplex?, J Control Release 190 (2014) 415-23.

[146] Z. Chu, Z. Li, H. Yong, D. Che, B. Li, C. Yan, T. Zhou, X. Wang, Y. Feng, K. Guo, S. Geng, Enhanced gene transfection and induction of apoptosis in melanoma cells by branched poly(beta-amino ester)s with uniformly distributed branching units, J Control Release 367 (2024) 197-208.

[147] X. Gao, D. Dong, C. Zhang, Y. Deng, J. Ding, S. Niu, S. Tan, L. Sun, Chitosan-Functionalized Poly(beta-Amino Ester) Hybrid System for Gene Delivery in Vaginal Mucosal Epithelial Cells, Pharmaceutics 16(1) (2024).

[148] P. Dosta, I. Tamargo, V. Ramos, S. Kumar, D.W. Kang, S. Borros, H. Jo, Delivery of Anti-microRNA-712 to Inflamed Endothelial Cells Using Poly(beta-amino ester) Nanoparticles Conjugated with VCAM-1 Targeting Peptide, Adv Healthc Mater 10(15) (2021) e2001894.

[149] M. Rodriguez, Y. Soler, M.K. Muthu Karuppan, Y. Zhao, E.V. Batrakova, N. El-Hage, Targeting Beclin1 as an Adjunctive Therapy against HIV Using Mannosylated Polyethylenimine Nanoparticles, Pharmaceutics 13(2) (2021).

[150] S. Patnaik, K.C. Gupta, Novel polyethylenimine-derived nanoparticles for in vivo gene delivery, Expert Opin Drug Deliv 10(2) (2013) 215-28.

[151] B. Urban-Klein, S. Werth, S. Abuharbeid, F. Czubayko, A. Aigner, RNAi-mediated gene-targeting through systemic application of polyethylenimine (PEI)-complexed siRNA in vivo, Gene Ther 12(5) (2005) 461-6.

[152] H. Ragelle, G. Vandermeulen, V. Préat, Chitosan-based siRNA delivery systems, Journal of Controlled Release 172(1) (2013) 207-218.

[153] J. Karlsson, K.R. Rhodes, J.J. Green, S.Y. Tzeng, Poly(beta-amino ester)s as gene delivery vehicles: challenges and opportunities, Expert Opin Drug Deliv 17(10) (2020) 1395-1410.

[154] L.R. Lynn DM, Degradable Poly(β-amino Esters): Synthesis, Characterization, and Self-Assembly with Plasmid DNA, J Am Chem Soc. 122(44) (2000) 10761-10768.

[155] A. Akinc, D.M. Lynn, D.G. Anderson, R. Langer, Parallel synthesis and biophysical characterization of a degradable polymer library for gene delivery, J Am Chem Soc 125(18) (2003) 5316-23.

[156] A.A. Eltoukhy, D. Chen, C.A. Alabi, R. Langer, D.G. Anderson, Degradable terpolymers with alkyl side chains demonstrate enhanced gene delivery potency and nanoparticle stability, Adv Mater 25(10) (2013) 1487-93.

[157] Y. Jin, X. Wang, A.P.E. Kromer, J.T. Müller, C. Zimmermann, Z. Xu, A. Hartschuh, F. Adams, O.M. Merkel, Role of Hydrophobic Modification in Spermine-Based Poly(β-amino ester)s for siRNA Delivery and Their Spray-Dried Powders for Inhalation and Improved Storage, Biomacromolecules 25(7) (2024) 4177-4191.

[158] P. Holzerny, B. Ajdini, W. Heusermann, K. Bruno, M. Schuleit, L. Meinel, M. Keller, Biophysical properties of chitosan/siRNA polyplexes: profiling the polymer/siRNA interactions and bioactivity, J Control Release 157(2) (2012) 297-304.

[159] Y. Li, Z. He, S. A, X. Wang, Z. Li, M. Johnson, R. Foley, I.L. Saez, J. Lyu, W. Wang, Artificial Intelligence (AI)-Aided Structure Optimization for Enhanced Gene Delivery: The Effect of the Polymer Component Distribution (PCD), ACS Appl Mater Interfaces 15(30) (2023) 36667-36675.

[160] D. Ouyang, H. Zhang, D.P. Herten, H.S. Parekh, S.C. Smith, Structure, dynamics, and energetics of siRNA-cationic vector complexation: a molecular dynamics study, J Phys Chem B 114(28) (2010) 9220-30.

[161] F. Marquet, F. Stojceski, G. Grasso, V. Patrulea, A. Danani, G. Borchard, Characterization of the Interaction of Polymeric Micelles with siRNA: A Combined Experimental and Molecular Dynamics Study, Polymers (Basel) 14(20) (2022).

[162] N. Bono, B. Coloma Smith, F. Moreschi, A. Redaelli, A. Gautieri, G. Candiani, In silico prediction of the in vitro behavior of polymeric gene delivery vectors, Nanoscale 13(17) (2021) 8333-8342.

[163] Z. Li, R. Guo, Z. Zhang, H. Yong, L. Guo, Z. Chen, D. Huang, D. Zhou, Enhancing gene transfection of poly(beta-amino ester)s through modulation of amphiphilicity and chain sequence, J Control Release 368 (2024) 131-139.

[164] A. Claveras Cabezudo, C. Athanasiou, A. Tsengenes, R.C. Wade, Scaling Protein-Water Interactions in the Martini 3 Coarse-Grained Force Field to Simulate Transmembrane Helix Dimers in Different Lipid Environments, J Chem Theory Comput 19(7) (2023) 2109-2119.

[165] S. Boeckle, K. von Gersdorff, S. van der Piepen, C. Culmsee, E. Wagner, M. Ogris, Purification of polyethylenimine polyplexes highlights the role of free polycations in gene transfer, J Gene Med 6(10) (2004) 1102-11.

[166] Y. Jin, F. Adams, A. Nguyen, S. Sturm, S. Carnerio, K. Muller-Caspary, O.M. Merkel, Synthesis and application of spermine-based amphiphilic poly(beta-amino ester)s for siRNA delivery, Nanoscale Adv 5(19) (2023) 5256-5262.

[167] D.J. Gary, J. Min, Y. Kim, K. Park, Y.Y. Won, The Effect of N/P Ratio on the In Vitro and In Vivo Interaction Properties of PEGylated Poly[2-(dimethylamino)ethyl methacrylate]-Based siRNA Complexes, Macromolecular Bioscience 13(8) (2013) 1059-1071.

[168] X. Wang, S.S. Kelkar, A.G. Hudson, R.B. Moore, T.M. Reineke, L.A. Madsen, Quantitation of Complexed versus Free Polymers in Interpolyelectrolyte Polyplex Formulations, ACS Macro Lett 2(11) (2013) 1038-1041.

[169] M. Kluenker, M. Mondeshki, M. Nawaz Tahir, W. Tremel, Monitoring Thiol-Ligand Exchange on Au Nanoparticle Surfaces, Langmuir 34(4) (2018) 1700-1710.

[170] M.A. Keniry, E.A. Owen, Insight into the molecular recognition of spermine by DNA quadruplexes from an NMR study of the association of spermine with the thrombin-binding aptamer, Journal of Molecular Recognition 26(7) (2013) 308-317.

[171] C.L. Perrin, T.J. Dwyer, Application of two-dimensional NMR to kinetics of chemical exchange, Chemical Reviews 90(6) (2002) 935-967.

[172] A. Kumar, R.R. Ernst, K. Wuthrich, A two-dimensional nuclear Overhauser enhancement (2D NOE) experiment for the elucidation of complete proton-proton cross-relaxation networks in biological macromolecules, Biochem Biophys Res Commun 95(1) (1980) 1-6.

[173] M.H. Levitt, Spin Dynamics: Basics of Nuclear Magnetic Resonance, 2nd Edition, Wiley2008.

[174] D.H. de Jong, S. Baoukina, H.I. Ingólfsson, S.J. Marrink, Martini straight: Boosting performance using a shorter cutoff and GPUs, Computer Physics Communications 199 (2016) 1-7.

[175] C. Sagui, T.A. Darden, MOLECULAR DYNAMICS SIMULATIONS OF BIOMOLECULES: Long-Range Electrostatic Effects, Annual Review of Biophysics and Biomolecular Structure 28(1) (1999) 155-179.

[176] F. Coelho, C. Botelho, J.L. Paris, E.F. Marques, B.F.B. Silva, Influence of the media ionic strength on the formation and in vitro biological performance of polycation-DNA complexes, Journal of Molecular Liquids 344 (2021) 117930.

[177] B. Lou, K. Connor, K. Sweeney, I.S. Miller, A. O'Farrell, E. Ruiz-Hernandez, D.M. Murray, G.P. Duffy, A. Wolfe, E. Mastrobattista, A.T. Byrne, W.E. Hennink, RGD-decorated cholesterol stabilized polyplexes for targeted siRNA delivery to glioblastoma cells, Drug Deliv Transl Res 9(3) (2019) 679-693.

[178] A. Gessner, A. Lieske, B. Paulke, R. Muller, Influence of surface charge density on protein adsorption on polymeric nanoparticles: analysis by two-dimensional electrophoresis, Eur J Pharm Biopharm 54(2) (2002) 165-70.

[179] R.V. Benjaminsen, M.A. Mattebjerg, J.R. Henriksen, S.M. Moghimi, T.L. Andresen, The possible "proton sponge " effect of polyethylenimine (PEI) does not include change in lysosomal pH, Mol Ther 21(1) (2013) 149-57.

[180] N. Hartl, D.C. Jurgens, S. Carneiro, A.C. Konig, X. Xiao, R. Liu, S.M. Hauck, O.M. Merkel, Protein corona investigations of polyplexes with varying hydrophobicity - From method development to in vitro studies, Int J Pharm 643 (2023) 123257.

[181] P. Dosta, N. Segovia, A. Cascante, V. Ramos, S. Borrós, Surface charge tunability as a powerful strategy to control electrostatic interaction for high efficiency silencing, using tailored oligopeptide-modified poly(beta-amino ester)s (PBAEs), Acta Biomaterialia 20 (2015) 82-93.

[182] J. Shi, J.L. Choi, B. Chou, R.N. Johnson, J.G. Schellinger, S.H. Pun, Effect of Polyplex Morphology on Cellular Uptake, Intracellular Trafficking, and Transgene Expression, ACS Nano 7(12) (2013) 10612-10620.

[183] K.M. Vijisha K. Rajan, Calculation of pKa Values of Alkanolamines – A DFT-B3LYP Computational Analysis, International Journal of Cheminformatics Research 2(1) (2016).

[184] D. Van Der Spoel, E. Lindahl, B. Hess, G. Groenhof, A.E. Mark, H.J. Berendsen, GROMACS: fast, flexible, and free, J Comput Chem 26(16) (2005) 1701-18.

[185] W.L. Jorgensen, J. Tirado-Rives, Potential energy functions for atomic-level simulations of water and organic and biomolecular systems, Proc Natl Acad Sci U S A 102(19) (2005) 6665-70.

[186] L.S. Dodda, J.Z. Vilseck, J. Tirado-Rives, W.L. Jorgensen, 1.14*CM1A-LBCC: Localized Bond-Charge Corrected CM1A Charges for Condensed-Phase Simulations, J Phys Chem B 121(15) (2017) 3864-3870.

[187] L.S. Dodda, I. Cabeza de Vaca, J. Tirado-Rives, W.L. Jorgensen, LigParGen web server: an automatic OPLS-AA parameter generator for organic ligands, Nucleic Acids Res 45(W1) (2017) W331-W336.

[188] J. Barnoud, https://github.com/jbarnoud/cgbuilder.

[189] A.K. Malde, L. Zuo, M. Breeze, M. Stroet, D. Poger, P.C. Nair, C. Oostenbrink, A.E. Mark, An Automated Force Field Topology Builder (ATB) and Repository: Version 1.0, J Chem Theory Comput 7(12) (2011) 4026-37.

[190] H. Lee, A.H. de Vries, S.J. Marrink, R.W. Pastor, A coarse-grained model for polyethylene oxide and polyethylene glycol: conformation and hydrodynamics, J Phys Chem B 113(40) (2009) 13186-94.

[191] B. Hess, Determining the shear viscosity of model liquids from molecular dynamics simulations, The Journal of Chemical Physics 116(1) (2002) 209-217.

[192] G. Bussi, D. Donadio, M. Parrinello, Canonical sampling through velocity rescaling, The Journal of Chemical Physics 126(1) (2007).

[193] M. Parrinello, A. Rahman, Polymorphic transitions in single crystals: A new molecular dynamics method, Journal of Applied Physics 52(12) (1981) 7182-7190.

[194] R. Gowers, M. Linke, J. Barnoud, T. Reddy, M. Melo, S. Seyler, J. Domański, D. Dotson, S. Buchoux, I. Kenney, O. Beckstein, MDAnalysis: A Python Package for the Rapid Analysis of Molecular Dynamics Simulations, Proceedings of the 15th Python in Science Conference, 2016, pp. 98-105.

[195] N. Michaud-Agrawal, E.J. Denning, T.B. Woolf, O. Beckstein, MDAnalysis: a toolkit for the analysis of molecular dynamics simulations, J Comput Chem 32(10) (2011) 2319-27.

[196] P. de Buyl, tidynamics: A tiny package to compute the dynamics of stochastic and molecular simulations, Journal of Open Source Software 3(28) (2018).

[197] V. Calandrini, Pellegrini, E., Calligari, P., Hinsen, K., Kneller, G. R., nMoldyn - Interfacing spectroscopic experiments, molecular dynamics simulations and models for time correlation functions, Collect. SFN 12 (2011) 201-232.

[198] B.M.H. Bruininks, T.A. Wassenaar, I. Vattulainen, Unbreaking Assemblies in Molecular Simulations with Periodic Boundaries, J Chem Inf Model 63(11) (2023) 3448-3452.

[199] W. Li, J. Sun, X. Zhang, L. Jia, M. Qiao, X. Zhao, H. Hu, D. Chen, Y. Wang, Synthesis and Characterization of pH-Responsive PEG-Poly(β-Amino Ester) Block Copolymer Micelles as Drug Carriers to Eliminate Cancer Stem Cells, Pharmaceutics 12(2) (2020).

[200] K.A. Whitehead, R. Langer, D.G. Anderson, Knocking down barriers: advances in siRNA delivery, Nat Rev Drug Discov 8(2) (2009) 129-38.

[201] T. Jeon, D.C. Luther, R. Goswami, C. Bell, H. Nagaraj, Y.A. Cicek, R. Huang, J.A. Mas-Rosario, J.L. Elia, J. Im, Y.-W. Lee, Y. Liu, F. Scaletti, M.E. Farkas, J. Mager, V.M. Rotello, Engineered Polymer–siRNA Polyplexes Provide Effective Treatment of Lung Inflammation, ACS Nano 17(5) (2023) 4315-4326.

[202] S.H. El Moukhtari, E. Garbayo, A. Amundarain, S. Pascual-Gil, A. Carrasco-León, F. Prosper, X. Agirre, M.J. Blanco-Prieto, Lipid nanoparticles for siRNA delivery in cancer treatment, Journal of Controlled Release 361 (2023) 130-146.

[203] R.M. Schiffelers, Cancer siRNA therapy by tumor selective delivery with ligand-targeted sterically stabilized nanoparticle, Nucleic Acids Research 32(19) (2004) e149-e149.

[204] L.M.P. Vermeulen, T. Brans, S.K. Samal, P. Dubruel, J. Demeester, S.C. De Smedt, K. Remaut, K. Braeckmans, Endosomal Size and Membrane Leakiness Influence Proton Sponge-Based Rupture of Endosomal Vesicles, ACS Nano 12(3) (2018) 2332-2345.

[205] B.D. Monnery, Polycation-Mediated Transfection: Mechanisms of Internalization and Intracellular Trafficking, Biomacromolecules 22(10) (2021) 4060-4083.

[206] Z.u. Rehman, D. Hoekstra, I.S. Zuhorn, Mechanism of Polyplex- and Lipoplex-Mediated Delivery of Nucleic Acids: Real-Time Visualization of Transient Membrane Destabilization without Endosomal Lysis, ACS Nano 7(5) (2013) 3767-3777.

[207] S.M. Bates, M.J. Munson, V. Trovisco, S. Pereira, S.R. Miller, A. Sabirsh, C.J. Betts, E.O. Blenke, N.J. Gay, The kinetics of endosomal disruption reveal differences in lipid nanoparticle induced cellular toxicity, Journal of Controlled Release 386 (2025).

[208] S. Vaidyanathan, B.G. Orr, M.M. Banaszak Holl, Role of Cell Membrane–Vector Interactions in Successful Gene Delivery, Accounts of Chemical Research 49(8) (2016) 1486-1493.

[209] I.M.S. Degors, C. Wang, Z.U. Rehman, I.S. Zuhorn, Carriers Break Barriers in Drug Delivery: Endocytosis and Endosomal Escape of Gene Delivery Vectors, Accounts of Chemical Research 52(7) (2019) 1750-1760.

[210] J.M. Johansson, H. Du Rietz, H. Hedlund, H.C. Eriksson, E. Oude Blenke, A. Pote, S. Harun, P. Nordenfelt, L. Lindfors, A. Wittrup, Cellular and biophysical barriers to lipid nanoparticle mediated delivery of RNA to the cytosol, (2024).

[211] J. Gilleron, W. Querbes, A. Zeigerer, A. Borodovsky, G. Marsico, U. Schubert, K. Manygoats, S. Seifert, C. Andree, M. Stöter, H. Epstein-Barash, L. Zhang, V. Koteliansky, K. Fitzgerald, E. Fava, M. Bickle, Y. Kalaidzidis, A. Akinc, M. Maier, M. Zerial, Image-based analysis of lipid nanoparticle–mediated siRNA delivery, intracellular trafficking and endosomal escape, Nature Biotechnology 31(7) (2013) 638-646.

[212] S. Sabnis, E.S. Kumarasinghe, T. Salerno, C. Mihai, T. Ketova, J.J. Senn, A. Lynn, A. Bulychev, I. McFadyen, J. Chan, Ö. Almarsson, M.G. Stanton, K.E. Benenato, A Novel Amino Lipid Series for mRNA Delivery: Improved Endosomal Escape and Sustained Pharmacology and Safety in Non-human Primates, Molecular Therapy 26(6) (2018) 1509-1519.

[213] D.G. Angelescu, Molecular modeling of the carbohydrate corona formation on a polyvinyl chloride nanoparticle and its impact on the adhesion to lipid bilayers, J Chem Phys 160(14) (2024).

[214] Y. Jin, F. Adams, J. Möller, L. Isert, C.M. Zimmermann, D. Keul, O.M. Merkel, Synthesis and Application of Low Molecular Weight PEI-Based Copolymers for siRNA Delivery with Smart Polymer Blends, Macromolecular Bioscience 23(2) (2022).

[215] S.C. Wilson, J.L. Baryza, A.J. Reynolds, K. Bowman, M.E. Keegan, S.M. Standley, N.P. Gardner, P. Parmar, V.O. Agir, S. Yadav, A. Zunic, C. Vargeese, C.C. Lee, S. Rajan, Real Time Measurement of PEG Shedding from Lipid Nanoparticles in Serum via NMR Spectroscopy, Molecular Pharmaceutics 12(2) (2015) 386-392.

[216] C.A. Alabi, G. Sahay, R. Langer, D.G. Anderson, Development of siRNA-probes for studying intracellular trafficking of siRNA nanoparticles, Integrative Biology 5(1) (2013) 224-230.

[217] A. Wittrup, A. Ai, X. Liu, P. Hamar, R. Trifonova, K. Charisse, M. Manoharan, T. Kirchhausen, J. Lieberman, Visualizing lipid-formulated siRNA release from endosomes and target gene knockdown, Nat Biotechnol 33(8) (2015) 870-6.

[218] H. Du Rietz, H. Hedlund, S. Wilhelmson, P. Nordenfelt, A. Wittrup, Imaging small molecule-induced endosomal escape of siRNA, Nature Communications 11(1) (2020).

[219] P. Boya, G. Kroemer, Lysosomal membrane permeabilization in cell death, Oncogene 27(50) (2008) 6434-6451.

[220] F. Sieber-Schäfer, M. Jiang, A. Kromer, A. Nguyen, M. Molbay, S. Pinto Carneiro, D. Jürgens, G. Burgstaller, B. Popper, B. Winkeljann, O.M. Merkel, Machine Learning-Enabled Polymer Discovery for Enhanced Pulmonary siRNA Delivery, Advanced Functional Materials (2025).

[221] I. Sæbø, M. Bjørås, H. Franzyk, E. Helgesen, J. Booth, Optimization of the Hemolysis Assay for the Assessment of Cytotoxicity, International Journal of Molecular Sciences 24(3) (2023).

[222] D. Khang, Y.K. Lee, E.-J. Choi, T.J. Webster, S.-H. Kim, Effect of the protein corona on nanoparticles for modulating cytotoxicity and immunotoxicity, International Journal of Nanomedicine (2014).

[223] Z. Darwich, A.S. Klymchenko, D. Dujardin, Y. Mély, Imaging lipid order changes in endosome membranes of live cells by using a Nile Red-based membrane probe, RSC Adv. 4(17) (2014) 8481-8488.

[224] I. Levental, K.R. Levental, F.A. Heberle, Lipid Rafts: Controversies Resolved, Mysteries Remain, Trends Cell Biol 30(5) (2020) 341-353.

[225] A. Hall, T. Róg, M. Karttunen, I. Vattulainen, Role of Glycolipids in Lipid Rafts: A View through Atomistic Molecular Dynamics Simulations with Galactosylceramide, The Journal of Physical Chemistry B 114(23) (2010) 7797-7807.

[226] I.D. Pogozheva, G.A. Armstrong, L. Kong, T.J. Hartnagel, C.A. Carpino, S.E. Gee, D.M. Picarello, A.S. Rubin, J. Lee, S. Park, A.L. Lomize, W. Im, Comparative Molecular Dynamics Simulation Studies of Realistic Eukaryotic, Prokaryotic, and Archaeal Membranes, J Chem Inf Model 62(4) (2022) 1036-1051.

[227] H.D. Gallala, K. Sandhoff, Biological Function of the Cellular Lipid BMP—BMP as a Key Activator for Cholesterol Sorting and Membrane Digestion, Neurochemical Research 36(9) (2010) 1594-1600.

[228] A. Erazo-Oliveras, K. Najjar, D. Truong, T.Y. Wang, D.J. Brock, A.R. Prater, J.P. Pellois, The Late Endosome and Its Lipid BMP Act as Gateways for Efficient Cytosolic Access of the Delivery Agent dfTAT and Its Macromolecular Cargos, Cell Chem Biol 23(5) (2016) 598-607.

[229] U. Kwolek, D. Jamróz, M. Janiczek, M. Nowakowska, P. Wydro, M. Kepczynski, Interactions of Polyethylenimines with Zwitterionic and Anionic Lipid Membranes, Langmuir 32(19) (2016) 5004-5018.

[230] C. Wang, T. Zhao, Y. Li, G. Huang, M.A. White, J. Gao, Investigation of endosome and lysosome biology by ultra pH-sensitive nanoprobes, Advanced Drug Delivery Reviews 113 (2017) 87-96.

[231] S. Omo-Lamai, Y. Wang, M.N. Patel, E.-O. Essien, M. Shen, A. Majumdar, C. Espy, J. Wu, B. Channer, M. Tobin, S. Murali, T.E. Papp, R. Maheshwari, L. Wang, L.S. Chase, M.E. Zamora, M.L. Arral, O.A. Marcos-Contreras, J.W. Myerson, C.A. Hunter, A. Tsourkas, V. Muzykantov, I. Brodsky, S. Shin, K.A. Whitehead, P. Gaskill, D. Discher, H. Parhiz, J.S. Brenner, Lipid Nanoparticle-Associated Inflammation is Triggered by Sensing of Endosomal Damage: Engineering Endosomal Escape Without Side Effects, (2024).

[232] P.R. Cullis, M.J. Hope, Effects of fusogenic agent on membrane structure of erythrocyte ghosts and the mechanism of membrane fusion, Nature 271(5646) (1978) 672-674.

[233] G. Brosio, G. Rossi, D. Bochicchio, Nanoparticle-induced biomembrane fusion: unraveling the effect of core size on stalk formation, Nanoscale Advances 5(18) (2023) 4675-4680.

[234] J. Sabin, M. Alatorre-Meda, J. Minones, Jr., V. Dominguez-Arca, G. Prieto, New insights on the mechanism of polyethylenimine transfection and their implications on gene therapy and DNA vaccines, Colloids Surf B Biointerfaces 210 (2022) 112219.

[235] S.M. Sarett, T.A. Werfel, I. Chandra, M.A. Jackson, T.E. Kavanaugh, M.E. Hattaway, T.D. Giorgio, C.L. Duvall, Hydrophobic interactions between polymeric carrier and palmitic acid-conjugated siRNA improve PEGylated polyplex stability and enhance in vivo pharmacokinetics and tumor gene silencing, Biomaterials 97 (2016) 122-132.

[236] C.L. Grigsby, K.W. Leong, Balancing protection and release of DNA: tools to address a bottleneck of non-viral gene delivery, Journal of The Royal Society Interface 7(suppl_1) (2009).

[237] A.F.S.A. Habeeb, Determination of free amino groups in proteins by trinitrobenzenesulfonic acid, Analytical Biochemistry 14(3) (1966) 328-336.

[238] H. Petersen, P.M. Fechner, A.L. Martin, K. Kunath, S. Stolnik, C.J. Roberts, D. Fischer, M.C. Davies, T. Kissel, Polyethylenimine-graft-Poly(ethylene glycol) Copolymers: Influence of Copolymer Block Structure on DNA Complexation and Biological Activities as Gene Delivery System, Bioconjugate Chemistry 13(4) (2002) 845-854.

[239] U. Essmann, L. Perera, M.L. Berkowitz, T. Darden, H. Lee, L.G. Pedersen, A smooth particle mesh Ewald method, The Journal of Chemical Physics 103(19) (1995) 8577-8593.

[240] E. Sezgin, I. Levental, S. Mayor, C. Eggeling, The mystery of membrane organization: composition, regulation and roles of lipid rafts, Nat Rev Mol Cell Biol 18(6) (2017) 361-374.

[241] P.V. Escriba, X. Busquets, J. Inokuchi, G. Balogh, Z. Torok, I. Horvath, J.L. Harwood, L. Vigh, Membrane lipid therapy: Modulation of the cell membrane composition and structure as a molecular base for drug discovery and new disease treatment, Prog Lipid Res 59 (2015) 38-53.

[242] Y. Yang, M. Lee, G.D. Fairn, Phospholipid subcellular localization and dynamics, J Biol Chem 293(17) (2018) 6230-6240.

[243] M. Zaborowska, D. Dziubak, D. Matyszewska, S. Sek, R. Bilewicz, Designing a Useful Lipid Raft Model Membrane for Electrochemical and Surface Analytical Studies, Molecules 26(18) (2021).

[244] M.R. Krause, S.L. Regen, The structural role of cholesterol in cell membranes: from condensed bilayers to lipid rafts, Acc Chem Res 47(12) (2014) 3512-21.

[245] C.A. Lopez, Z. Sovova, F.J. van Eerden, A.H. de Vries, S.J. Marrink, Martini Force Field Parameters for Glycolipids, J Chem Theory Comput 9(3) (2013) 1694-708.

[246] L. Borges-Araujo, P.C.T. Souza, F. Fernandes, M.N. Melo, Improved Parameterization of Phosphatidylinositide Lipid Headgroups for the Martini 3 Coarse-Grain Force Field, J Chem Theory Comput 18(1) (2022) 357-373.

[247] V. Calandrini, E. Pellegrini, P. Calligari, K. Hinsen, G.R. Kneller, nMoldyn - Interfacing spectroscopic experiments, molecular dynamics simulations and models for time correlation functions, École thématique de la Société Française de la Neutronique 12 (2011) 201-232.

[248] N. Michaud-Agrawal, E.J. Denning, T.B. Woolf, O. Beckstein, MDAnalysis: A toolkit for the analysis of molecular dynamics simulations, Journal of Computational Chemistry 32(10) (2011) 2319-2327.

[249] F. Fornasier, L.M.P. Souza, F.R. Souza, F. Reynaud, A.S. Pimentel, Lipophilicity of Coarse-Grained Cholesterol Models, J Chem Inf Model 60(2) (2020) 569-577.

[250] S. Kumar, J.M. Rosenberg, D. Bouzida, R.H. Swendsen, P.A. Kollman, THE weighted histogram analysis method for free-energy calculations on biomolecules. I. The method, Journal of Computational Chemistry 13(8) (2004) 1011-1021.

[251] L.S. Stelzl, A. Kells, E. Rosta, G. Hummer, Dynamic Histogram Analysis To Determine Free Energies and Rates from Biased Simulations, Journal of Chemical Theory and Computation 13(12) (2017) 6328-6342.

[252] S. Jo, T. Kim, V.G. Iyer, W. Im, CHARMM-GUI: A web-based graphical user interface for CHARMM, Journal of Computational Chemistry 29(11) (2008) 1859-1865.

[253] B.R. Brooks, C.L. Brooks, A.D. Mackerell, L. Nilsson, R.J. Petrella, B. Roux, Y. Won, G. Archontis, C. Bartels, S. Boresch, A. Caflisch, L. Caves, Q. Cui, A.R. Dinner, M. Feig, S. Fischer, J. Gao, M. Hodoscek, W. Im, K. Kuczera, T. Lazaridis, J. Ma, V. Ovchinnikov, E. Paci, R.W. Pastor, C.B. Post, J.Z. Pu, M. Schaefer, B. Tidor, R.M. Venable, H.L. Woodcock, X. Wu, W. Yang, D.M. York, M. Karplus, CHARMM: The biomolecular simulation program, Journal of Computational Chemistry 30(10) (2009) 1545-1614.

[254] J. Lee, X. Cheng, J.M. Swails, M.S. Yeom, P.K. Eastman, J.A. Lemkul, S. Wei, J. Buckner, J.C. Jeong, Y. Qi, S. Jo, V.S. Pande, D.A. Case, C.L. Brooks, A.D. MacKerell, J.B. Klauda, W. Im, CHARMM-GUI Input Generator for NAMD, GROMACS, AMBER, OpenMM, and CHARMM/OpenMM Simulations Using the CHARMM36 Additive Force Field, Journal of Chemical Theory and Computation 12(1) (2015) 405-413.

[255] E.L. Wu, X. Cheng, S. Jo, H. Rui, K.C. Song, E.M. Dávila-Contreras, Y. Qi, J. Lee, V. Monje-Galvan, R.M. Venable, J.B. Klauda, W. Im, CHARMM-GUIMembrane Buildertoward realistic biological membrane simulations, Journal of Computational Chemistry 35(27) (2014) 1997-2004.

[256] S. Jo, J.B. Lim, J.B. Klauda, W. Im, CHARMM-GUI Membrane Builder for Mixed Bilayers and Its Application to Yeast Membranes, Biophysical Journal 97(1) (2009) 50-58.

[257] A. Yuan, S. Jo, T. Kim, W. Im, Automated Builder and Database of Protein/Membrane Complexes for Molecular Dynamics Simulations, PLoS ONE 2(9) (2007).

[258] S. Kim, J. Lee, S. Jo, C.L. Brooks, H.S. Lee, W. Im, CHARMM-GUI ligand reader and modeler for CHARMM force field generation of small molecules, Journal of Computational Chemistry 38(21) (2017) 1879-1886.

Acknowledgements

After more than three years of work on this project, it is a great satisfaction to see how all the individual steps have come together. This achievement would not have been possible without the support of many people.

First, I would like to thank my supervisor, Prof. Dr. Olivia Merkel, for her scientific guidance, support, and enthusiasm. It has been an honor to be trusted and challenged with this exciting topic, which enabled me to get to know the world of MD simulation. Thank you for creating such an encouraging and kind work environment.
Secondly, I would like to thank Dr. Benjamin Winkeljann — your input and expertise brought great improvement to my scientific work.

I would also like to acknowledge all my co-authors. In particular, I would like to thank Min Jiang, for all the efforts you put into the in vitro work for this project. You are a true sunshine in this group. I would also like to thank the PBAE team for all the joint efforts to put our puzzle pieces together. Additionally, I would like to thank Dr. Lars Allmendinger for his work on the NMR experiments for this project and Sebastian Sturm for the TEM imaging.

Furthermore, I want to thank all members of Pharmaceutical Technology at LMU for the great working atmosphere, inspiring discussions, and all the organization that takes place behind the scenes. Thank you to everyone in AK Merkel and AK Frieß for great ski trips, lunch breaks full of laughter, and unforgettable celebrations.

I especially want to express my gratitude to the members of the Blondie Lab, because I don’t know how I would have managed this time without you.
I also want to thank my office mate Felix for sharing many of my struggles — in the end, ML is pretty much the same as MD.
At the same time, I am grateful to all my friends outside of this PhD bubble, who always reminded me that there is much more to life than work.

Of course, I would never be where I am today without my family- especially my Mama and Papa, my brother, and my grandparents.
Thank you for giving me the feeling that I could achieve anything. Thank you for the never-ending support, and for clearing so many obstacles from my path.

Lastly, I would like to thank my partner, Patrick. Your mission to make me laugh every day brings so much lightness to my days. Together, we can climb any mountain.